APPENDIX A

Seismic Acquisition Parameters and Processing Workflow

A-1. Seismic Acquisition Parameters

1) Survey definition

Acquisition Mode:	3D
Shot interval:	18.75m / flip flop
Inline offset:	315m
Cell Length:	6.25m
Cell Width:	28.125m
Line Orientation:	37.0 / 217.0°

2) Energy Source

Source type:	Sodera G guns
Number of sources:	2
Air pressure:	2000 psi
Volume:	2 x 3900 cu. In.
Number of sub-arrays:	2 x 3
Array Separation:	56.25m
Gun String Separation:	12.5m
Source Layout:	14m x 25m
Source Length:	14m
Source Depth:	5m

Gun synchronisation:	90% @ +/-1ms, 10% @ +/-1.5ms

3) Streamer

Number of Streamers:	8
Streamer Length:	4500m
Streamer Depth:	7m +/-1m
Streamer Separation:	112.5m
Number of groups:	8 x 360
Group interval:	12.5m

4) Data Recording

Projection:	Transverse Mercator
Projection System:	WGS84, UTM, Zone 51S
Central Meridian:	123° E
Scale Factor on Central Meridian:	0.9996

5) Map Projection

Record length:	5.5s
Sampling rate:	2ms
Lo-cut filter - Hydrophone:	3Hz / 12dB per octave
Hi-cut filter – Hydrophone:	206Hz / 276dB per octave
Format:	SEG-D – 8036 3590 Tapes

A-2. Seismic Processing Workflow

1) Transcription from SEG-D to PGS internal format
2) Navigation-seismic merge
3) Shot and channel edits from observers reports
4) 3 Hz low cut filter
5) System delay static apply (Phase2 Ext -36ms, Phase2 and Onnia North -120ms)
6) Gain recovery – multiply amplitudes by T2

7) Swell noise attenuation (Spine) and despike
8) Receiver-based Bandwidth Optimization (RBO)
9) Designature using far field signature to zero-phase
10) Receiver motion correction
11) Resample to 4ms with anti-alias filter
12) Linear noise attenuation (Tau-P)
13) Correct data to MSL – apply gun & cable correction and tidal statics correction
14) Deterministic shallow water demultiple (Swdemul)
15) Deep water multiple attenuation (3D SRME)
16) Reef replacement static
17) V1 velocity analysis (1012.5m x 1000m grid) – inline direction.
18) Residual linear noise attenuation
19) K-filter / trace drop
20) Extra V1 velocity analysis around reefs (506.25m x 500m grid) – inline direction
21) High resolution Radon demultiple
22) 4D regularization & interpolation of missing data (Interp4D)
    a. Input grid size = 28.125m x 12.5m
    b. Output grid size = 14.0625m x 12.5m
23) 3D CDP denoise in NE of prospect, outside of fully-migrated area
24) SEG-Y 3592 output – 3D Binned and Regularized Pre-Migration CDP Gathers (at MSL, without NMO correction, gain recovery removed, reef replacement statics applied)
25) Q phase (for VMB and final imaging deliverables) – Handover of Time to Depth processing
26) 6 Iterative VTI velocity updates using beam migration and reflection tomography
27) Beam Pre-Stack Depth Migration (unlimited aperture) output CMPs
28) Gather Preconditioning, Residual Moveout Correction (2nd order)
29) Q-amplitude Compensation
30) Time domain Radon De-multiple
31) 3D CDP Denoise

32) Trim Statics

33) Output 3D CMP BEAM Pre-SDM CIGs in SEGY format (NMO applied in time domain)

34) Stack

    a. FULL = 6 degree - TX mute,

    b. ANGLES = NEAR (6-19 degrees), MID (19-32 degrees) and FAR (32-45 degrees)

APPENDIX B

Well Tie Results

Chapter 4 was shown some examples of the final well tie of mid angle stack only. This appendix were contained all final well tie which used final averaged wavelets to generate the synthetic traces. The final well tie for near, mid and far angle stacks in the study were shown separately of Well-A, Well-C and Well-D in the following figures.

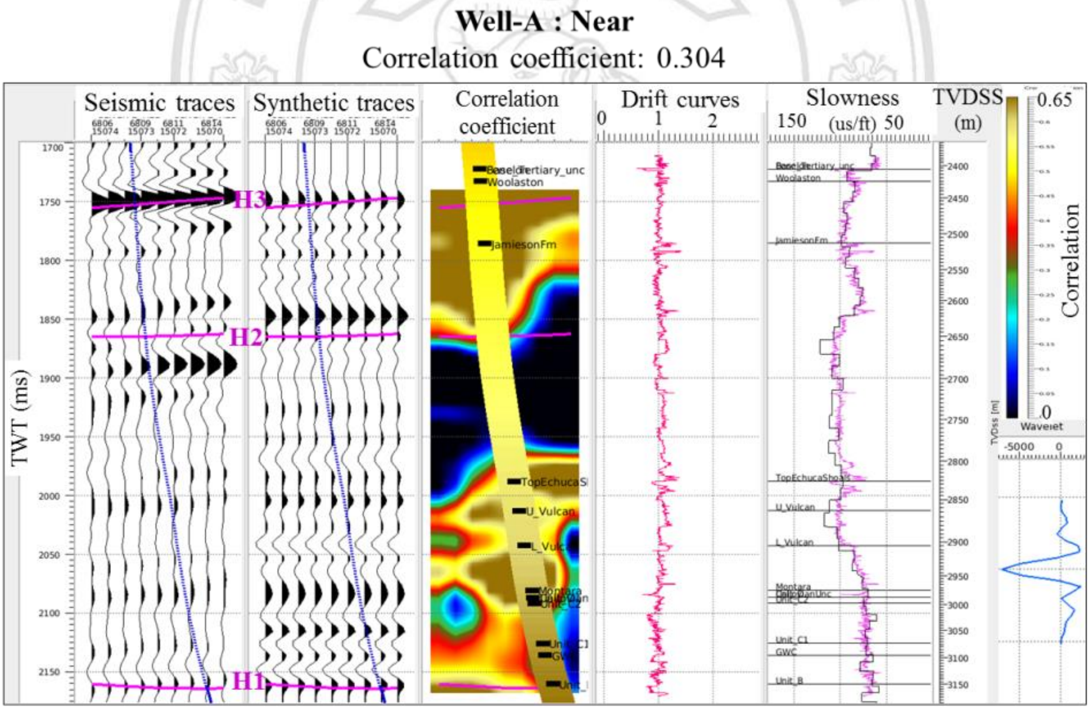

Figure B-1 Synthetic tie at Well-A showing the tie at near angle stacks.

Well-A : Mid

Correlation coefficient: 0.338

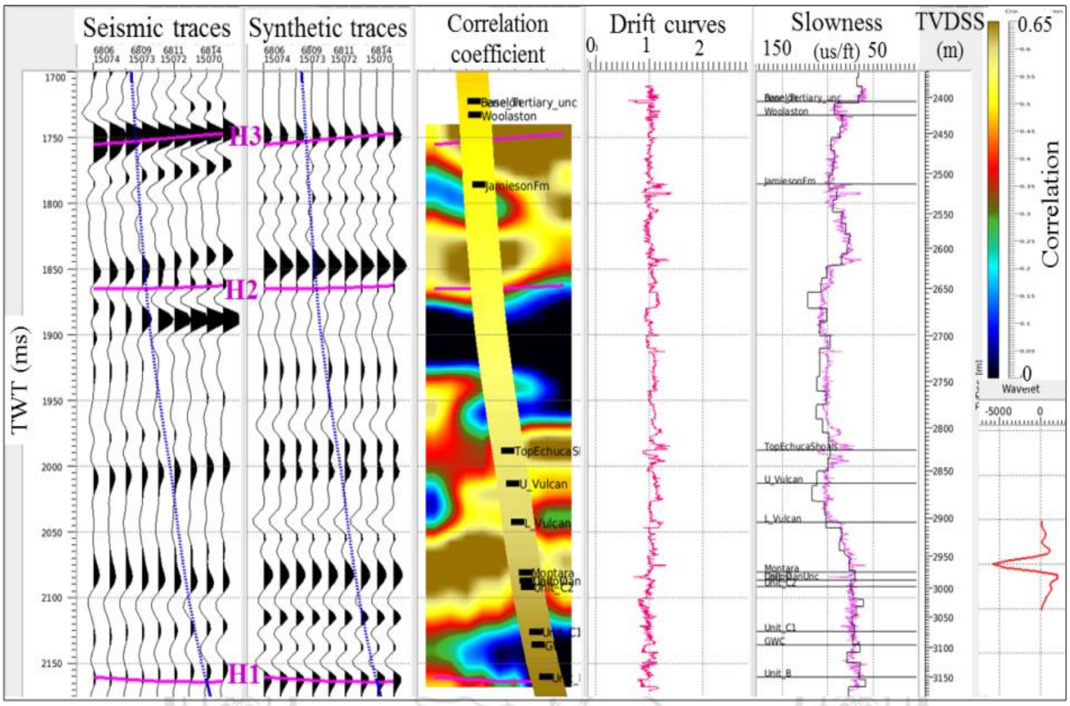

Figure B-2 Synthetic tie at Well-A showing the tie at mid angle stacks.

Well-A : Far

Correlation coefficient: 0.242

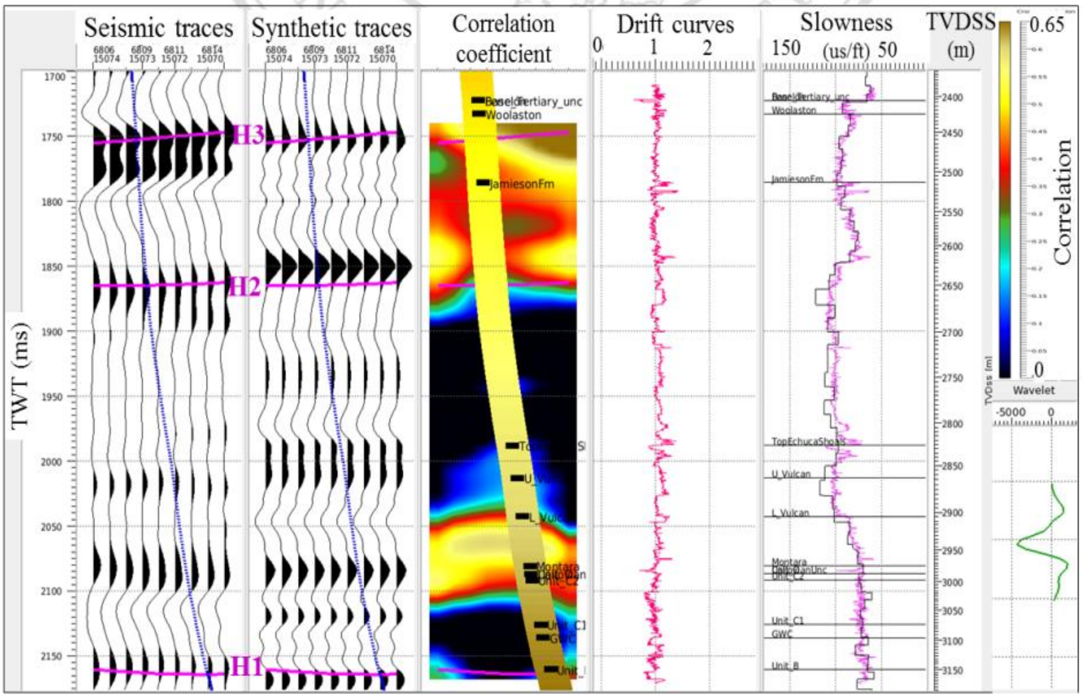

Figure B-3 Synthetic tie at Well-A showing the tie at far angle stacks.

Well-C : Near

Correlation coefficient: 0.450

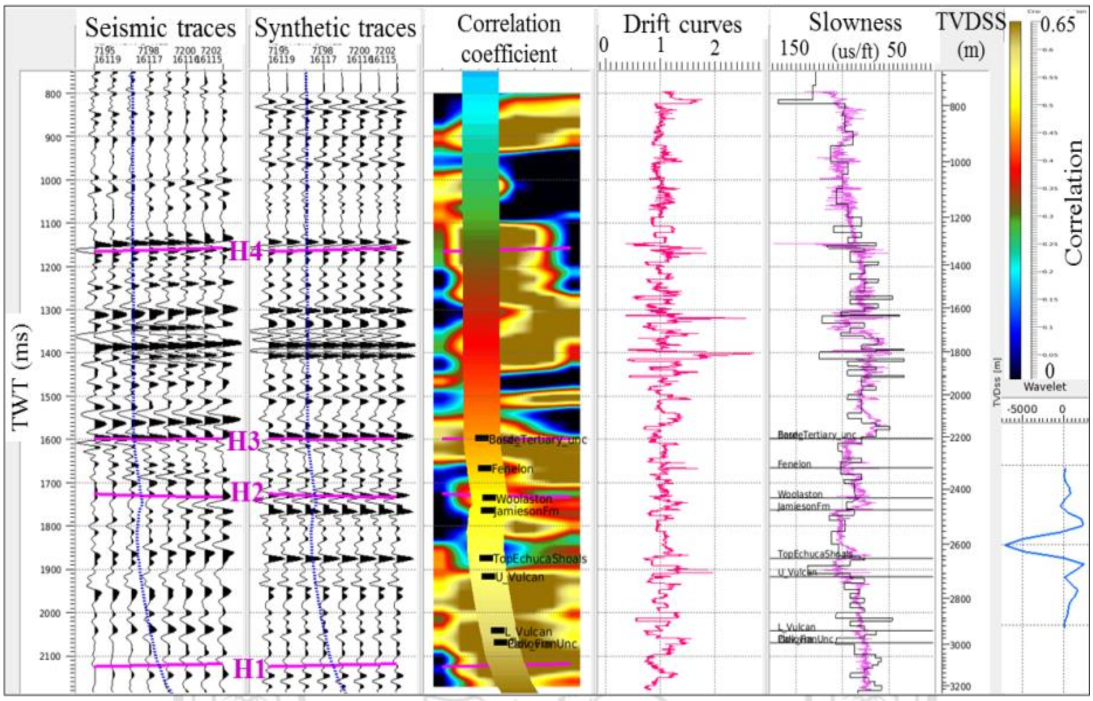

Figure B-4 Synthetic tie at Well-C showing the tie at near angle stacks.

Well-C : Mid

Correlation coefficient: 0.441

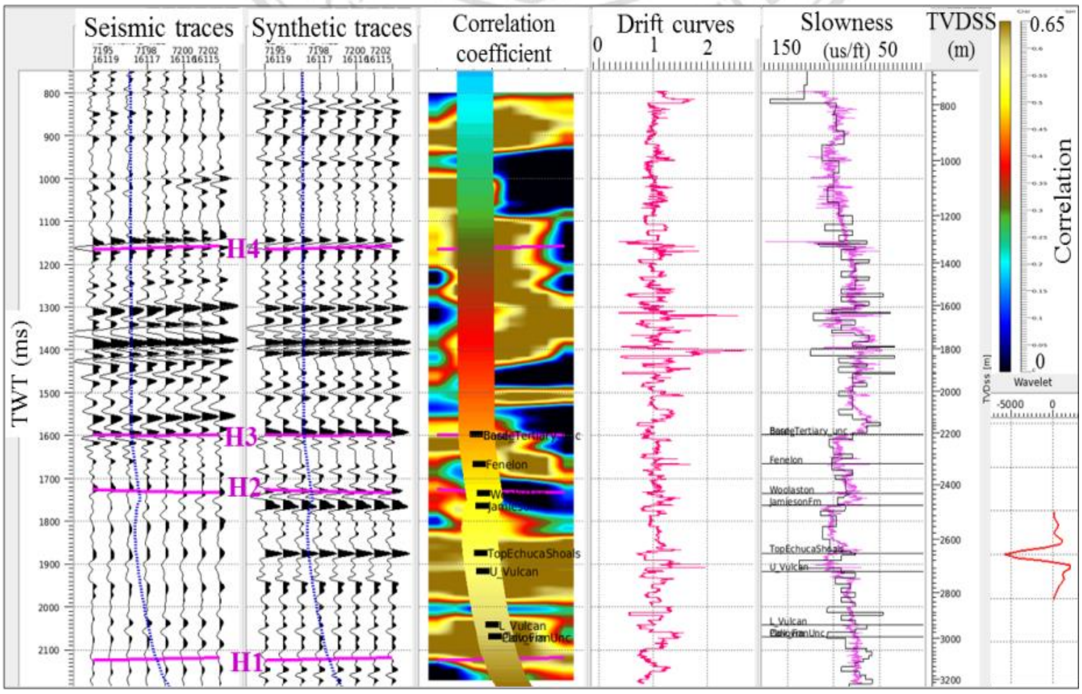

Figure B-5 Synthetic tie at Well-C showing the tie at mid angle stacks.

Well-C : Far

Correlation coefficient: 0.356

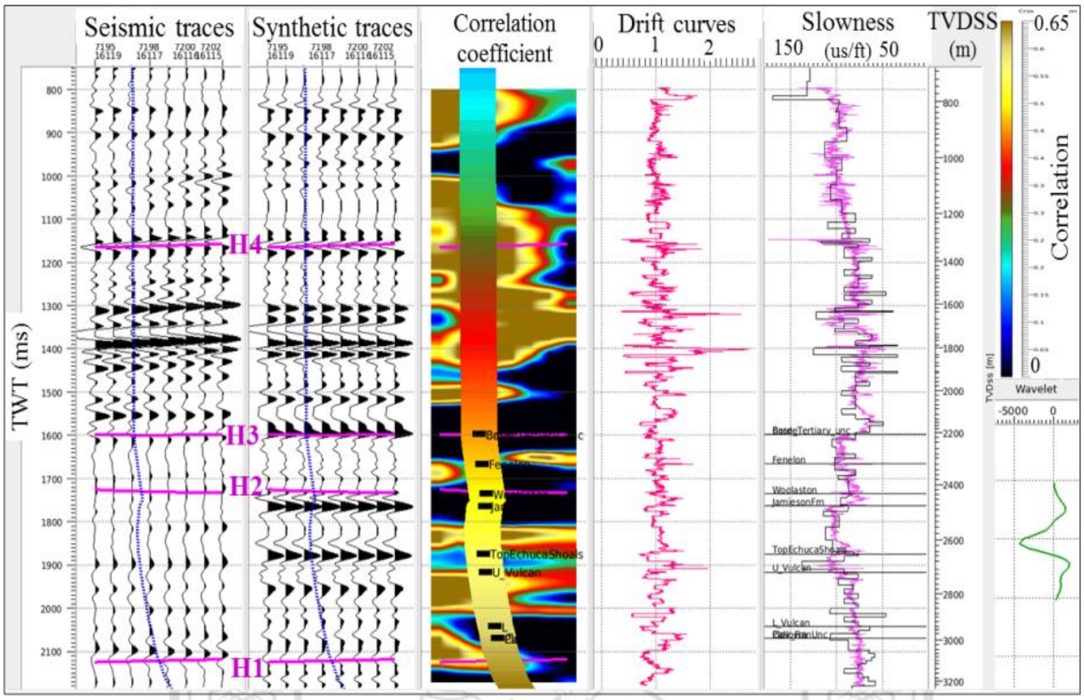

Figure B-6 Synthetic tie at Well-C showing the tie at far angle stacks.

Well-D : Near

Correlation coefficient: 0.424

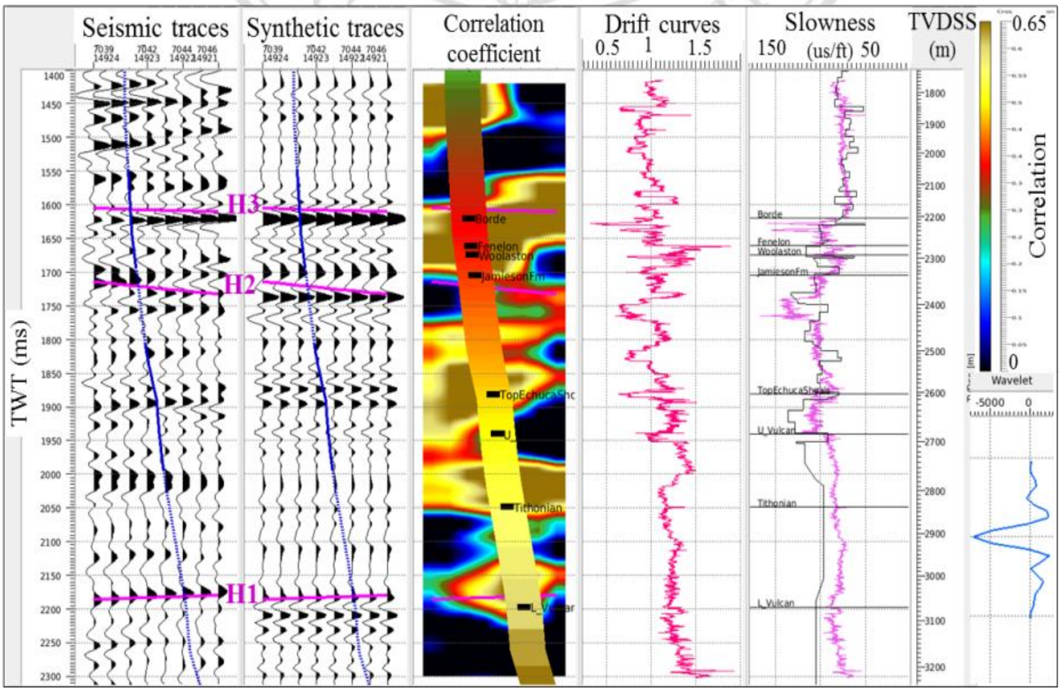

Figure B-7 Synthetic tie at Well-D showing the tie at near angle stacks.

Well-D : Mid

Correlation coefficient: 0.412

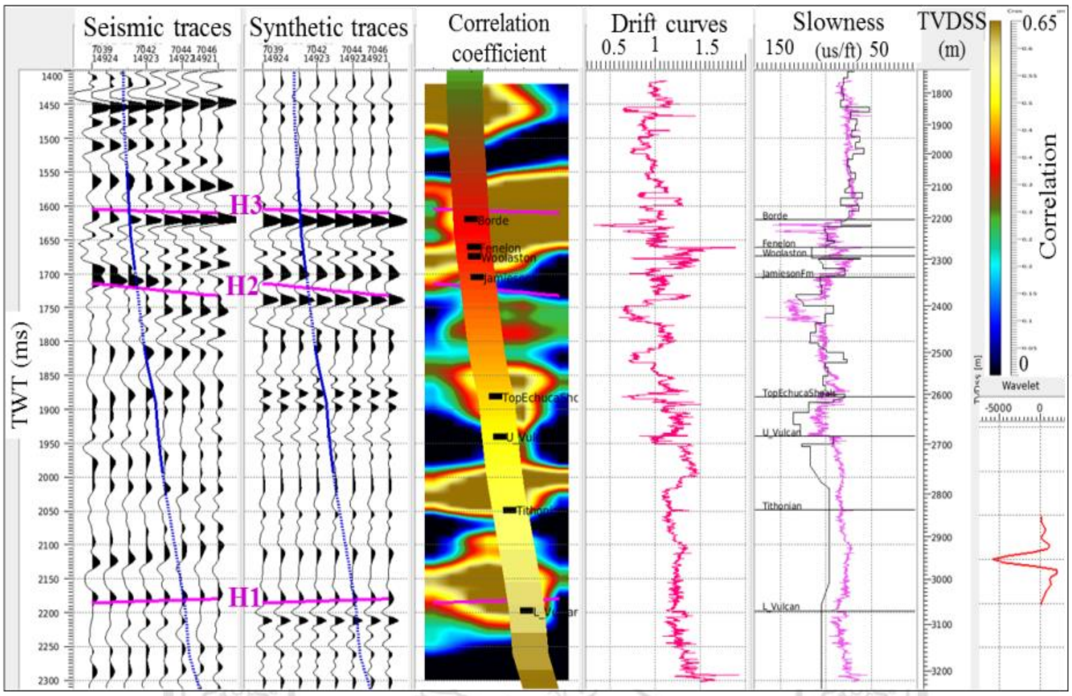

Figure B-8 Synthetic tie at Well-D showing the tie at mid angle stacks.

Well-D : Far

Correlation coefficient: 0.297

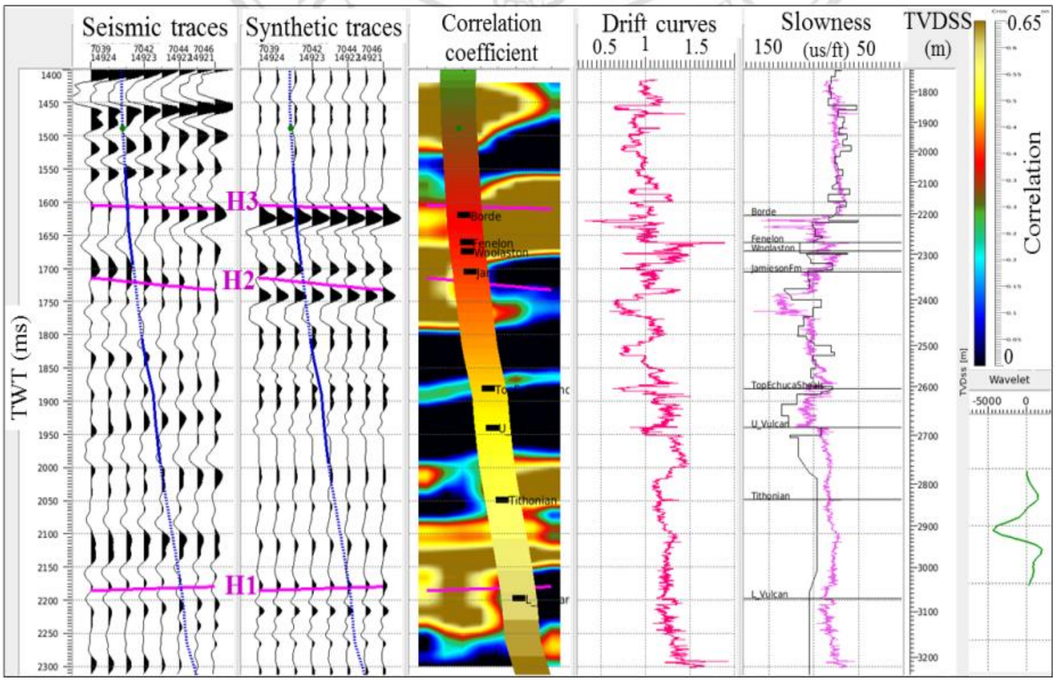

Figure B-9 Synthetic tie at Well-D showing the tie at far angle stacks.

APPENCIX C

Seismic Pre-Stack Simultaneous Inversion

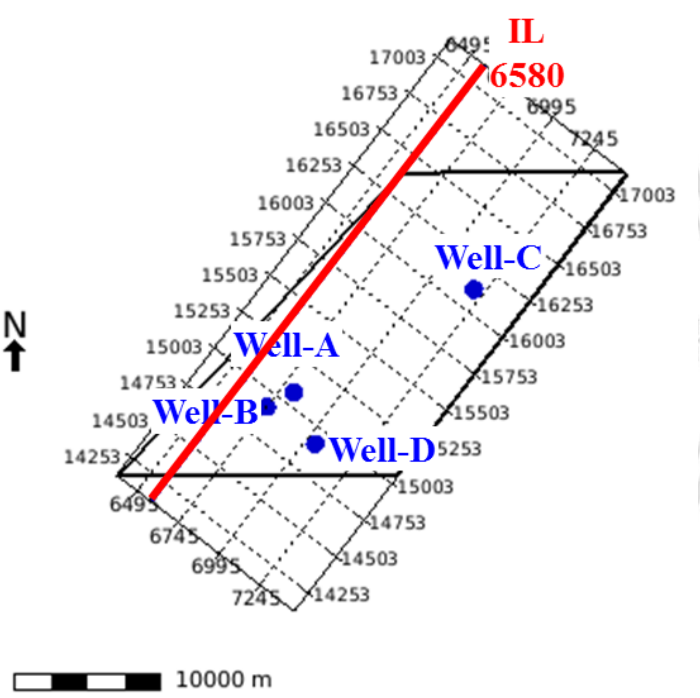

Figure C-1 Map location of inline 6580.

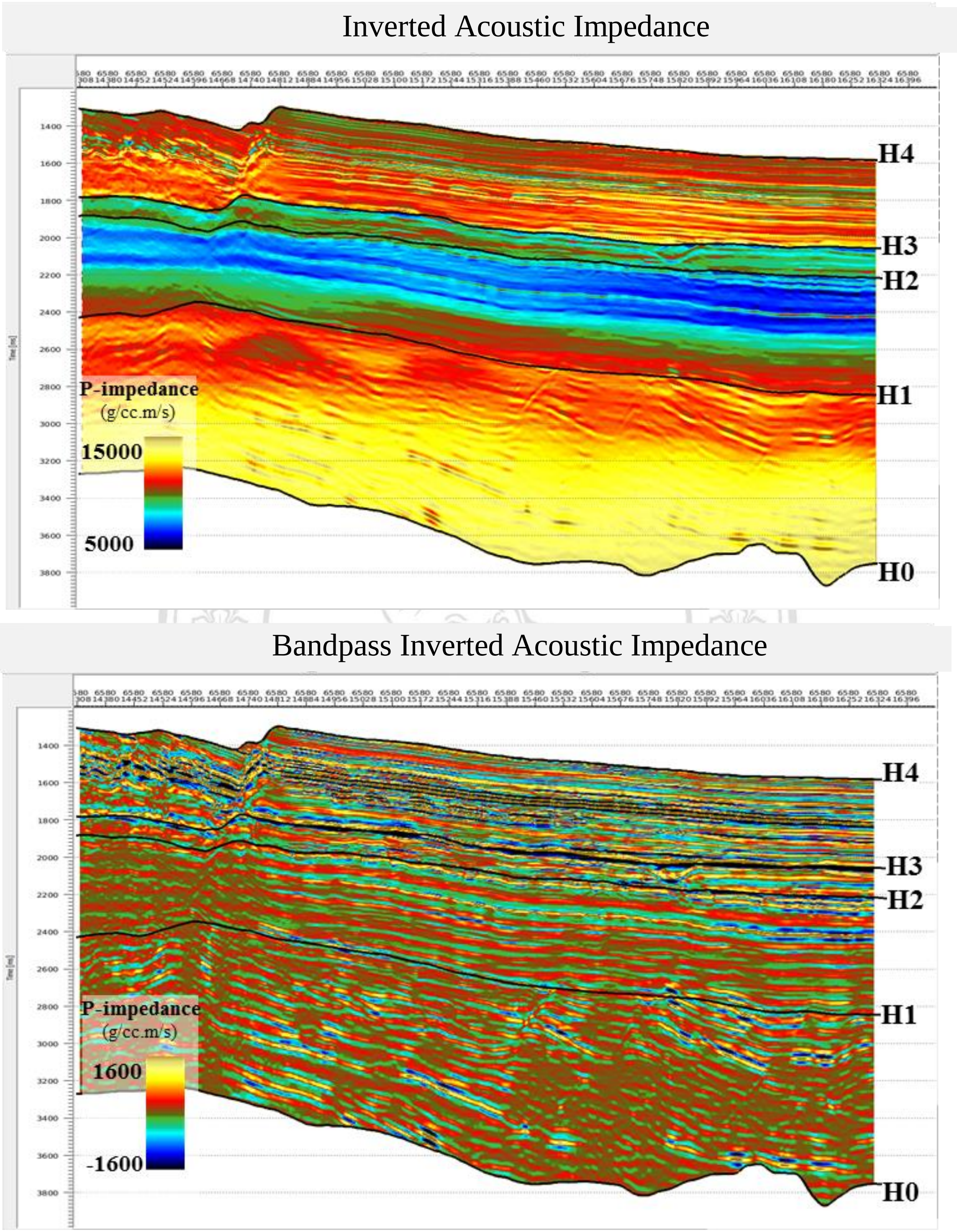

Figure C-2 Inline 6580 section of final absolute acoustic impedance (top) and bandpass filtering were applied to inverted acoustic impedance to create comparable relative inversion results (bottom).

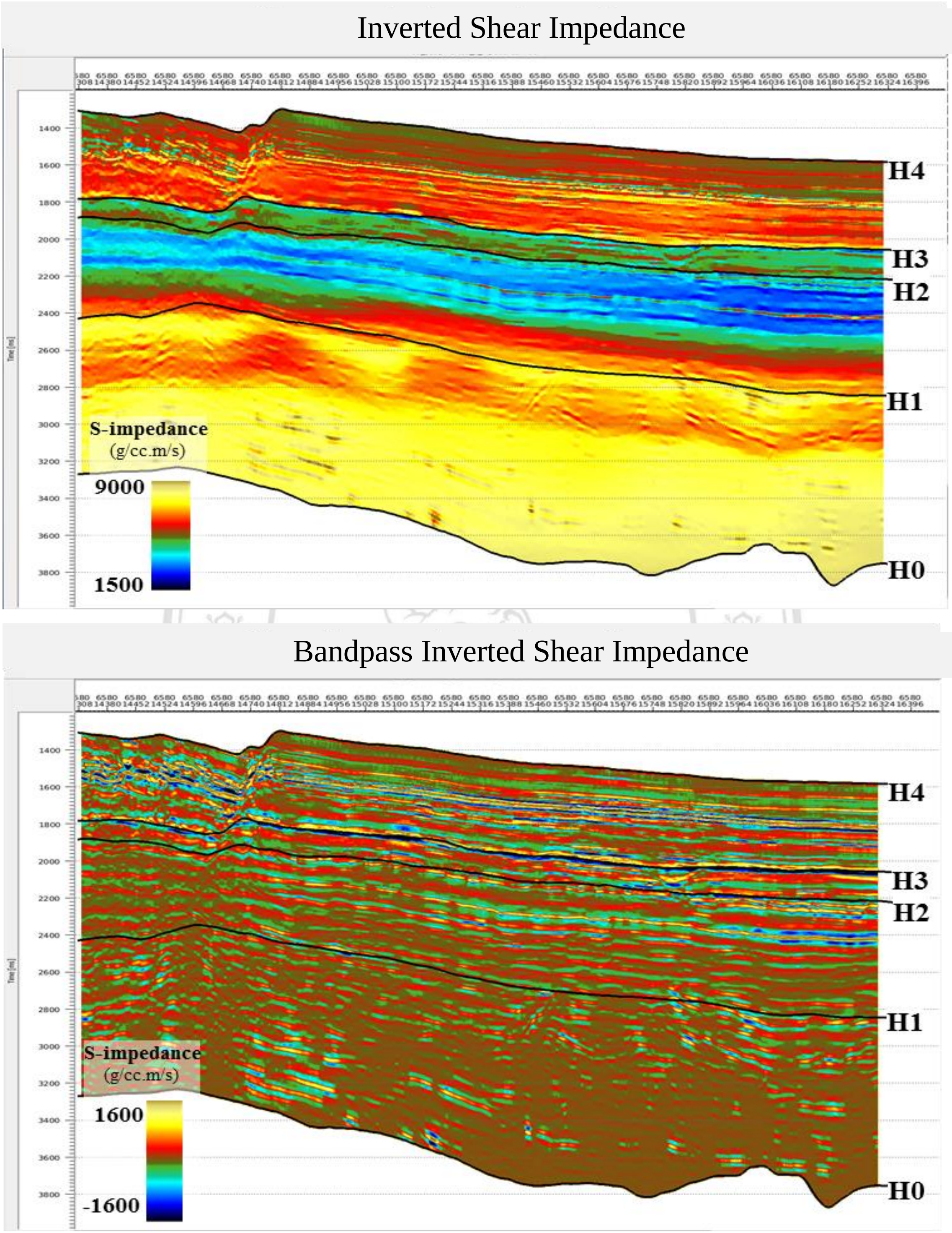

Figure C-3 Inline 6580 section of final absolute shear impedance (top) and bandpass filtering were applied to inverted shear impedance to create comparable relative inversion results (bottom).

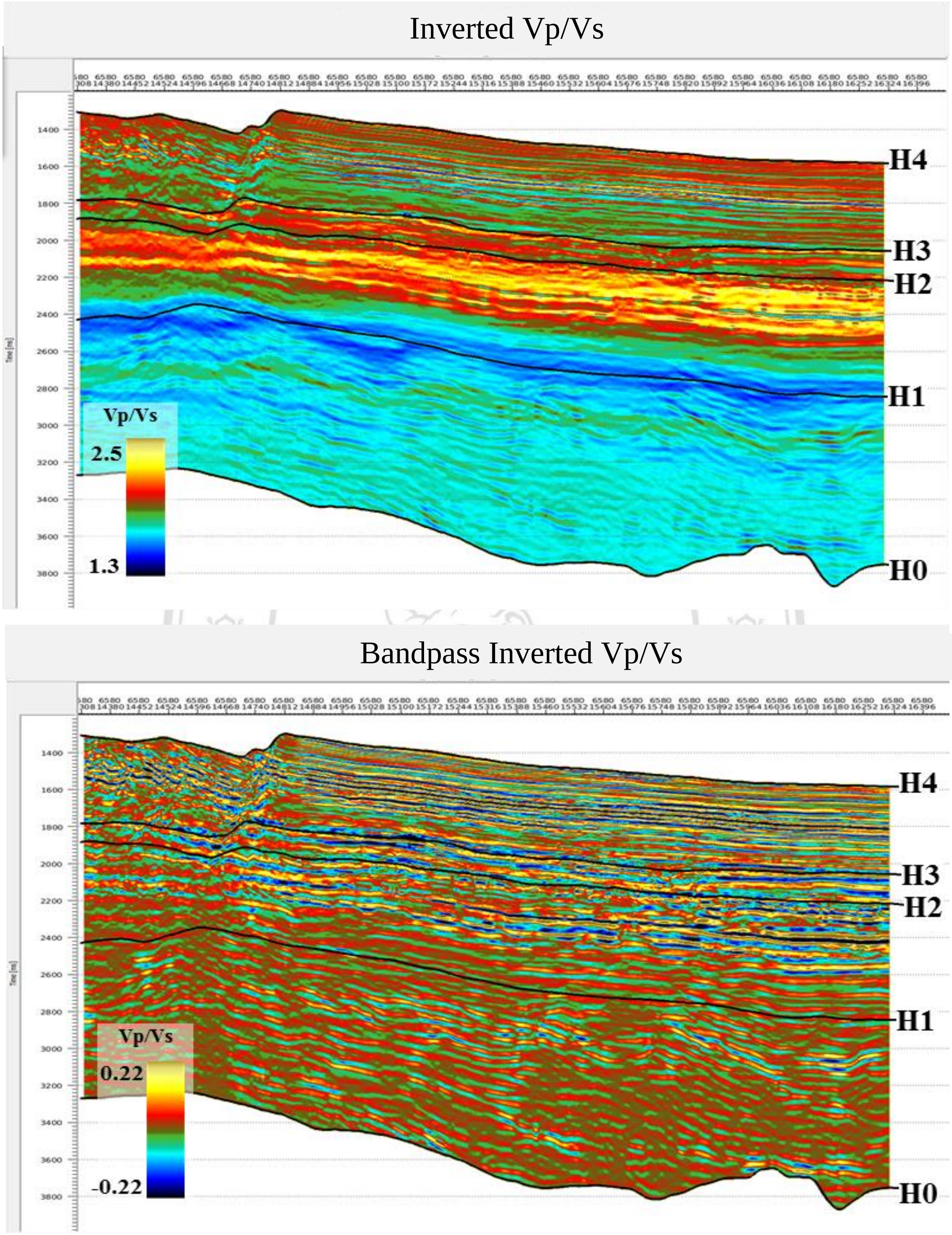

Figure C-4 Inline 6580 section of final Vp/Vs (top) and bandpass filtering were applied to inverted Vp/Vs to create comparable relative inversion results (bottom).

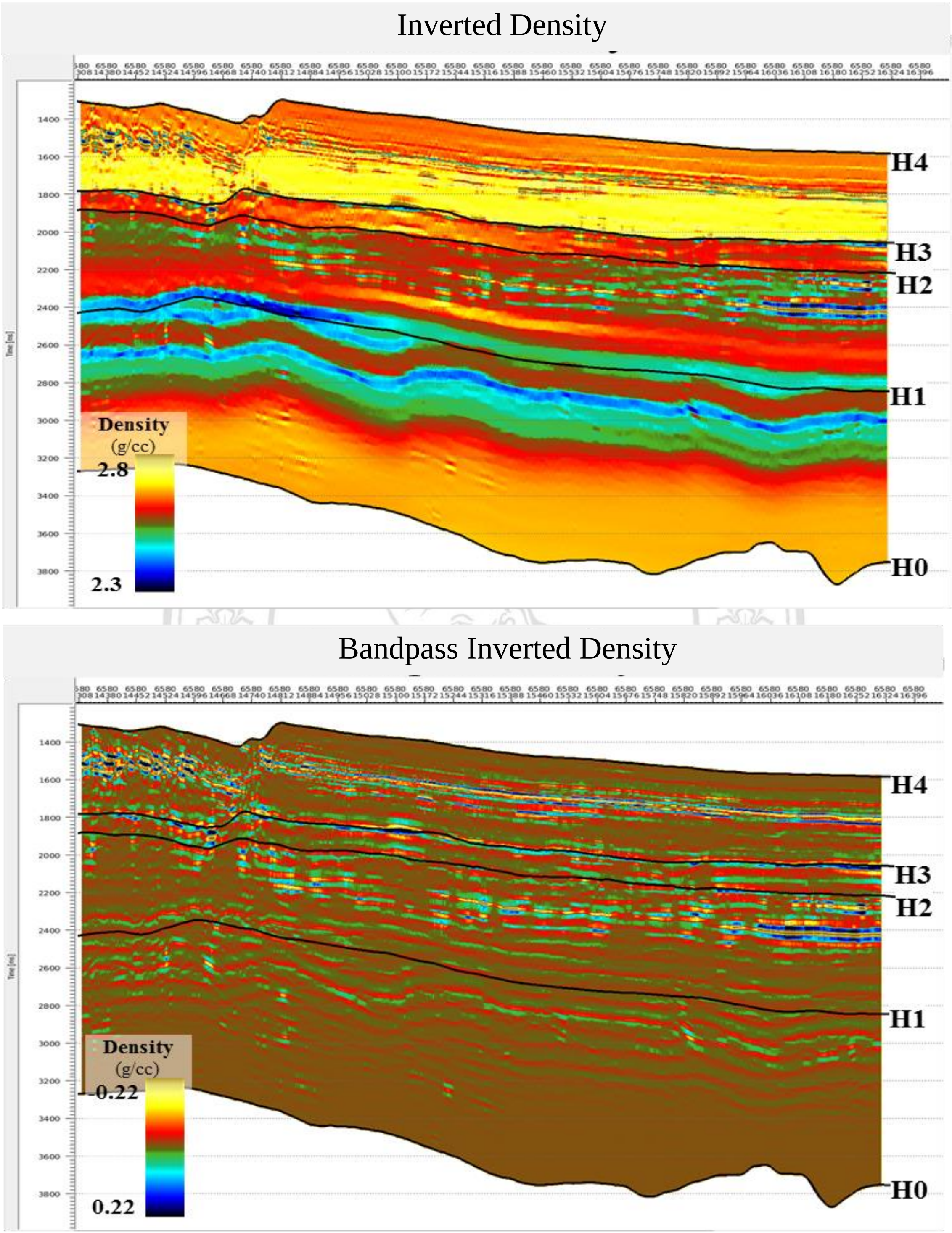

Figure C-5 Inline 6580 section of final density (top) and bandpass filtering were applied to inverted density to create comparable relative inversion results (bottom).

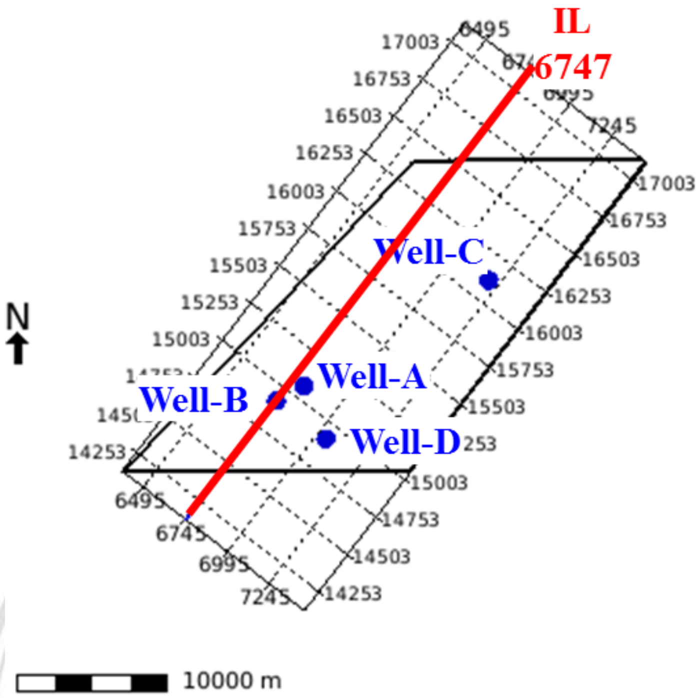

Figure C-6 Map location of inline 6747 that passed through Well-B location.

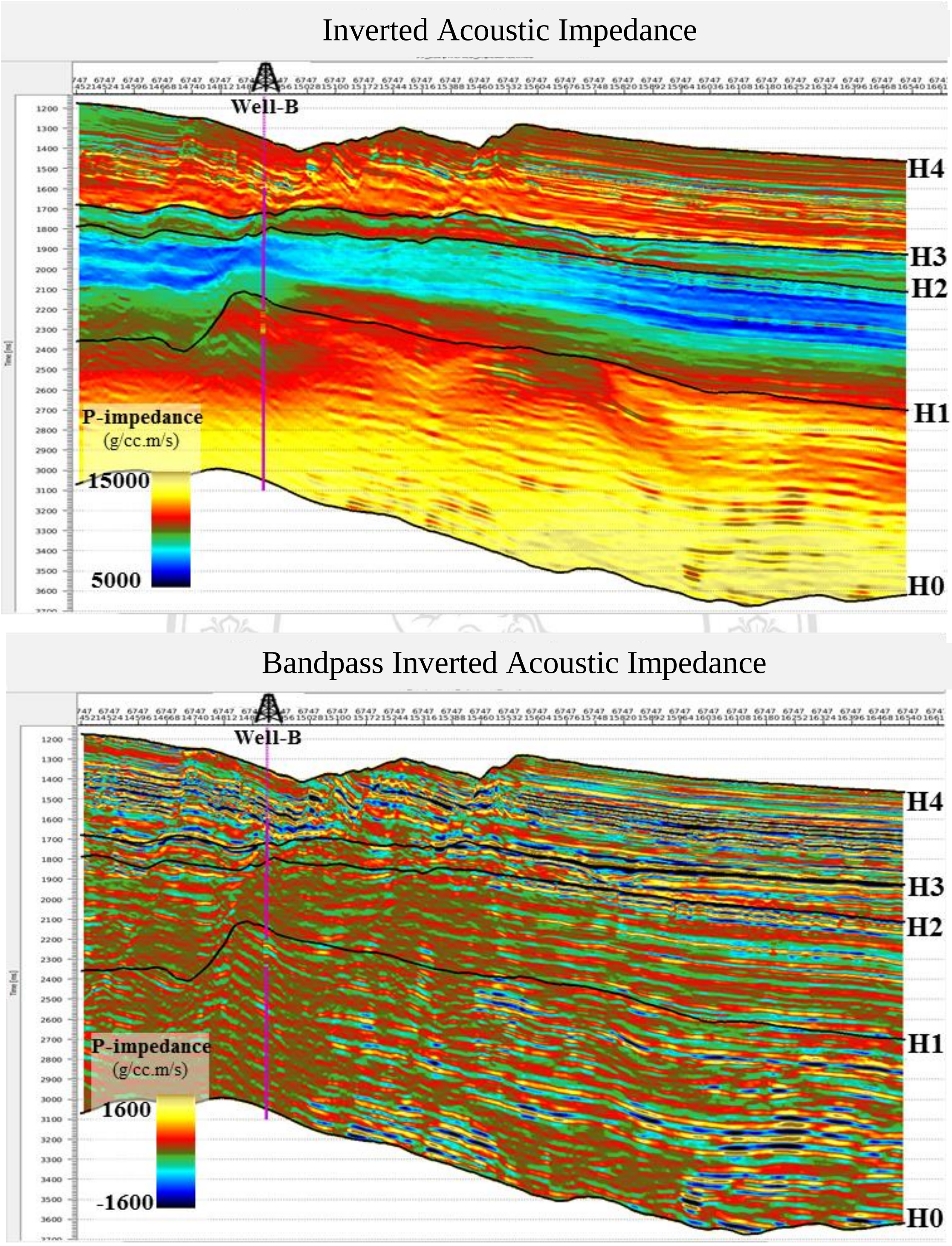

Figure C-7 Inline 6747 section of final absolute acoustic impedance comparing with acoustic impedance logs at Well-B (top). Bandpass filtering were applied to both inverted acoustic impedance and well data to create comparable relative inversion results (bottom).

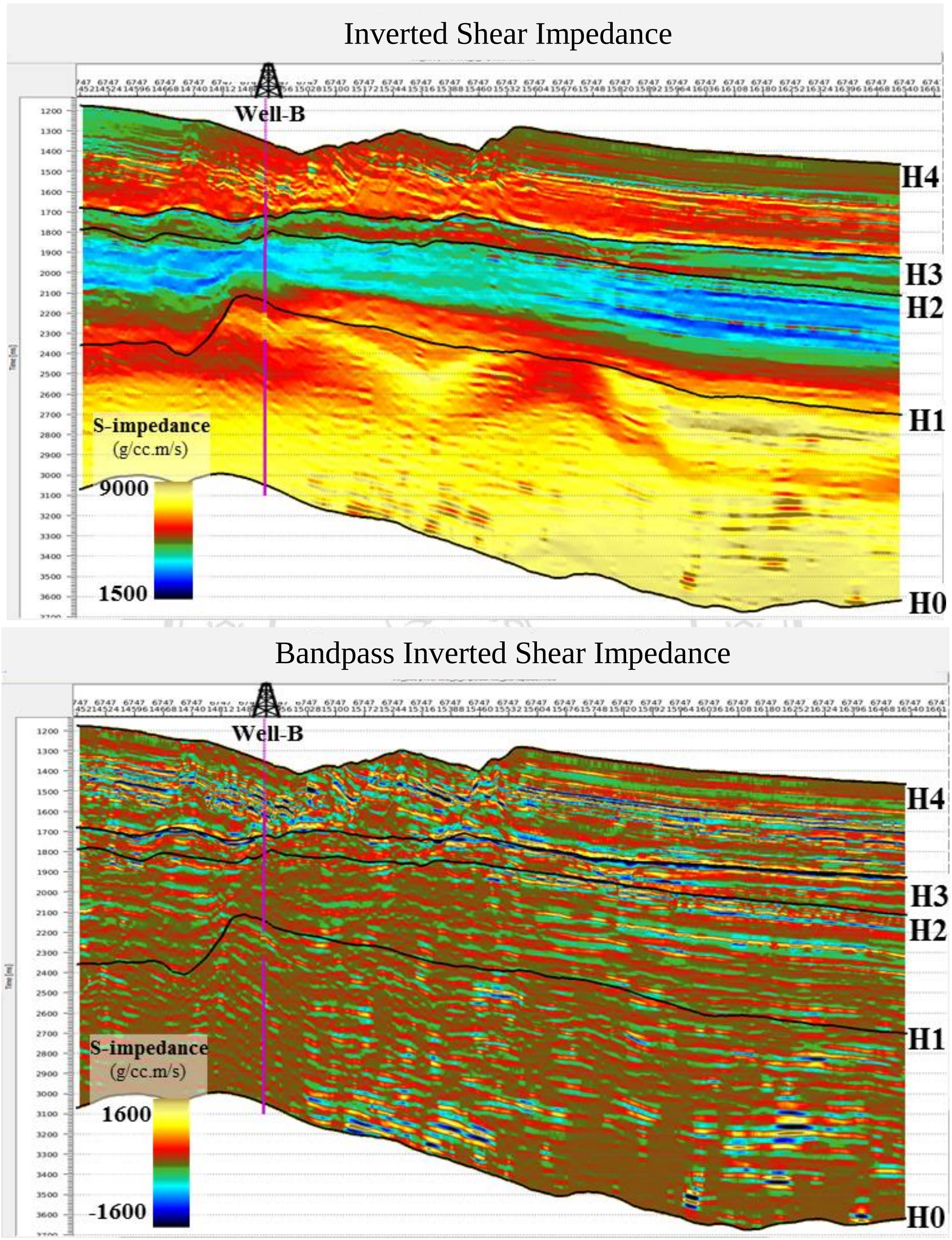

Figure C-8 Inline 6747 section of final absolute shear impedance comparing with shear impedance logs at Well-B (top). Bandpass filtering were applied to both inverted shear impedance and well data to create comparable relative inversion results (bottom).

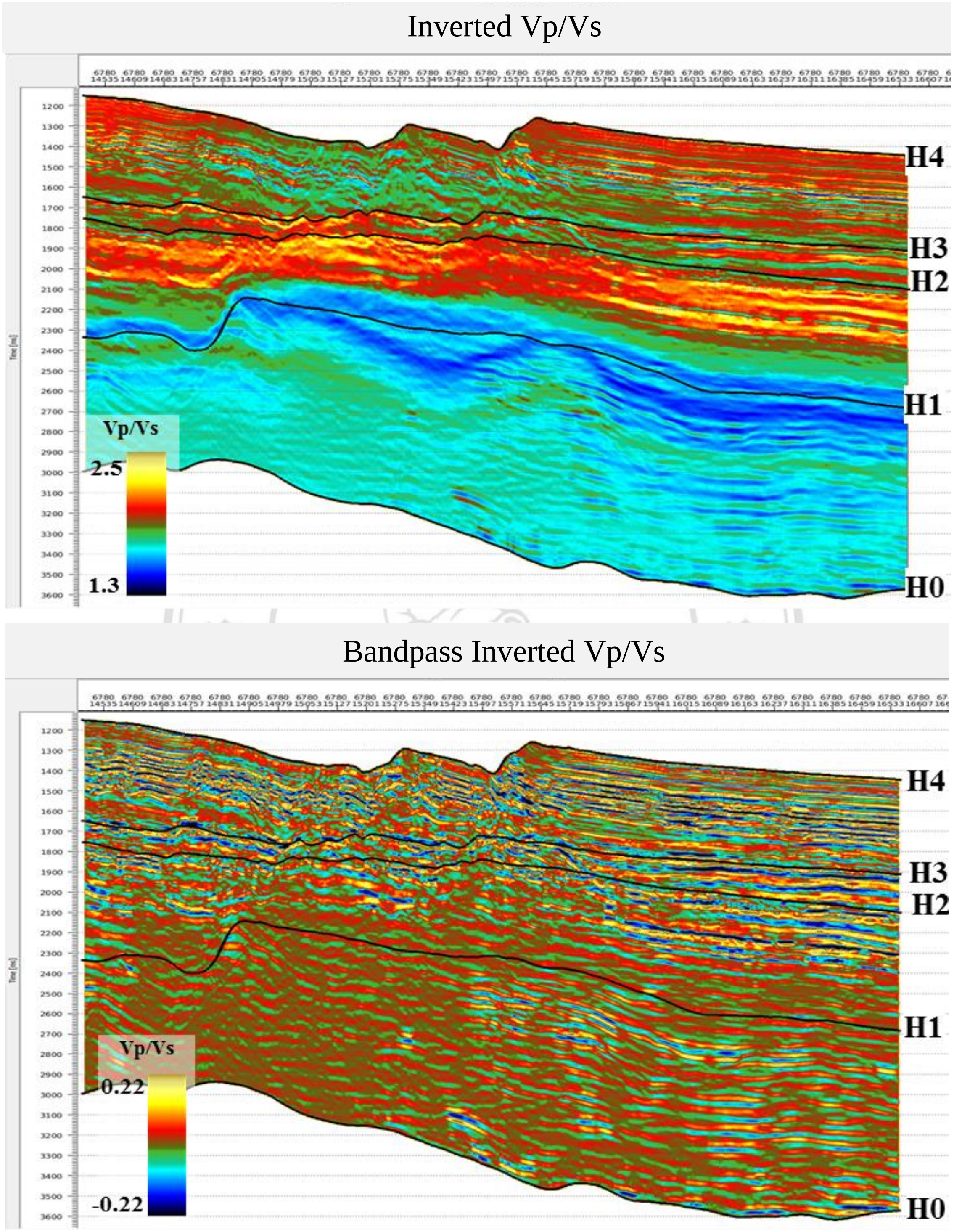

Figure C-9 Inline 6747 section of final absolute Vp/Vs comparing with Vp/Vs logs at Well-B (top). Bandpass filtering were applied to both inverted Vp/Vs and well data to create comparable relative inversion results (bottom).

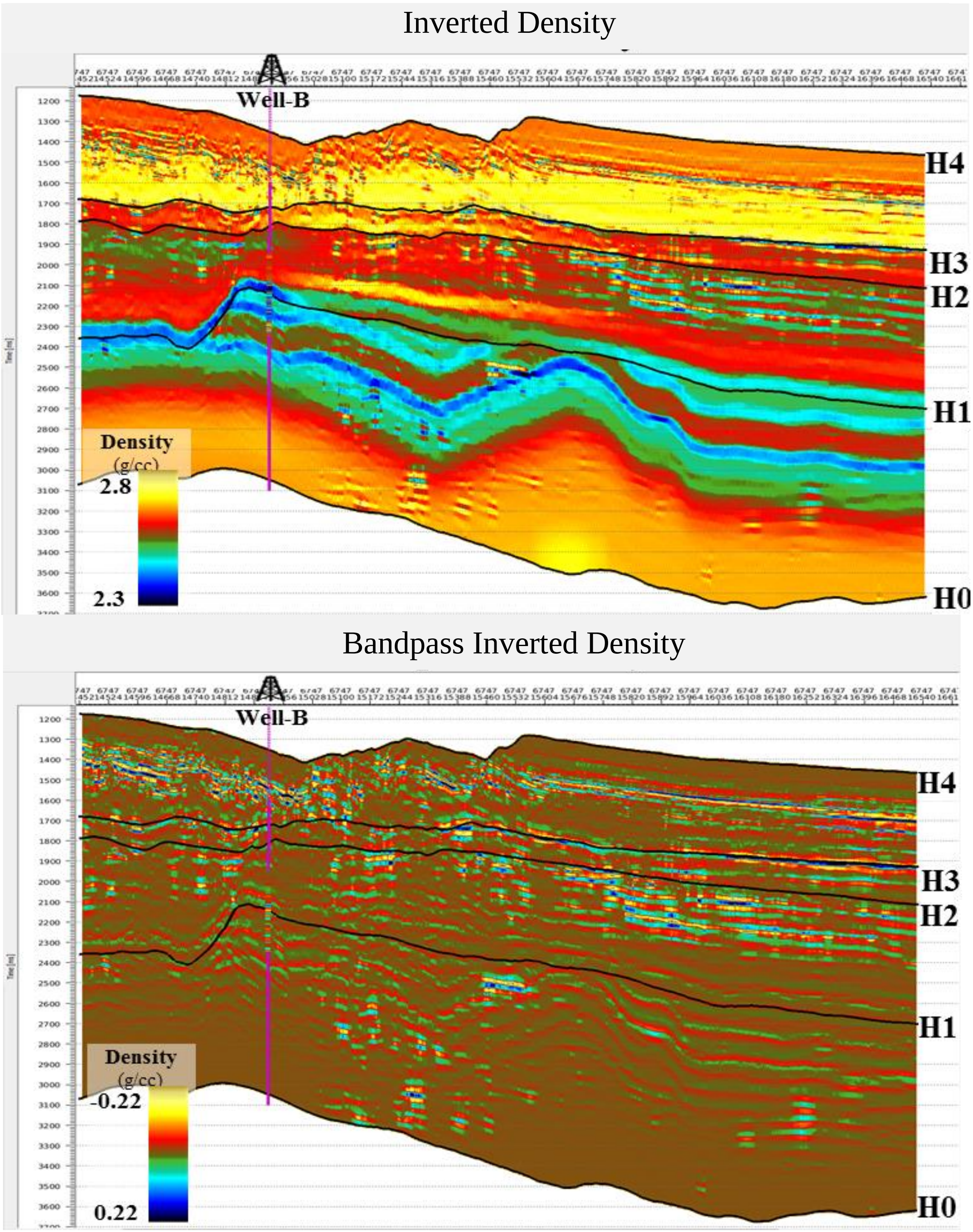

Figure C-10 Inline 6747 section of final absolute density comparing with density logs at Well-B (top). Bandpass filtering were applied to both inverted density and well data to create comparable relative inversion results (bottom).

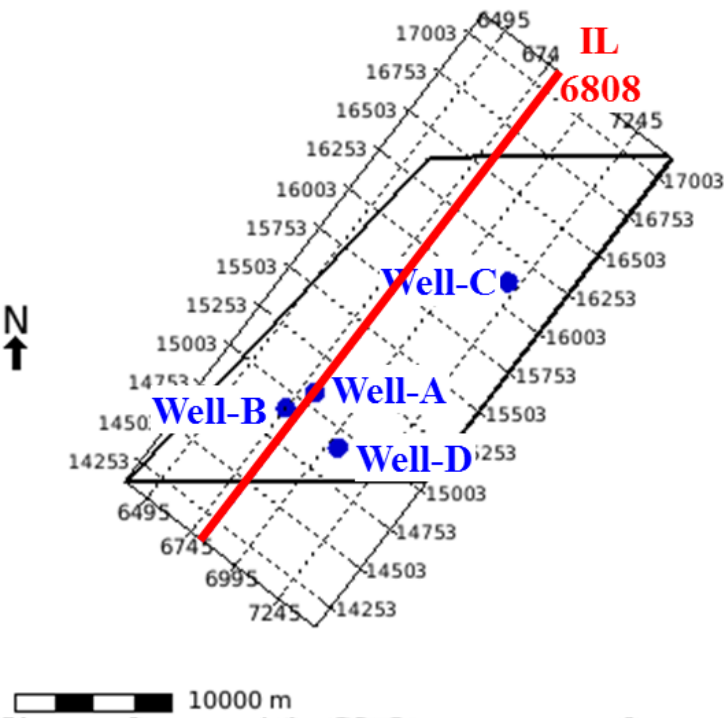

Figure C-11 Map location of inline 6808 that passed through Well-A location.

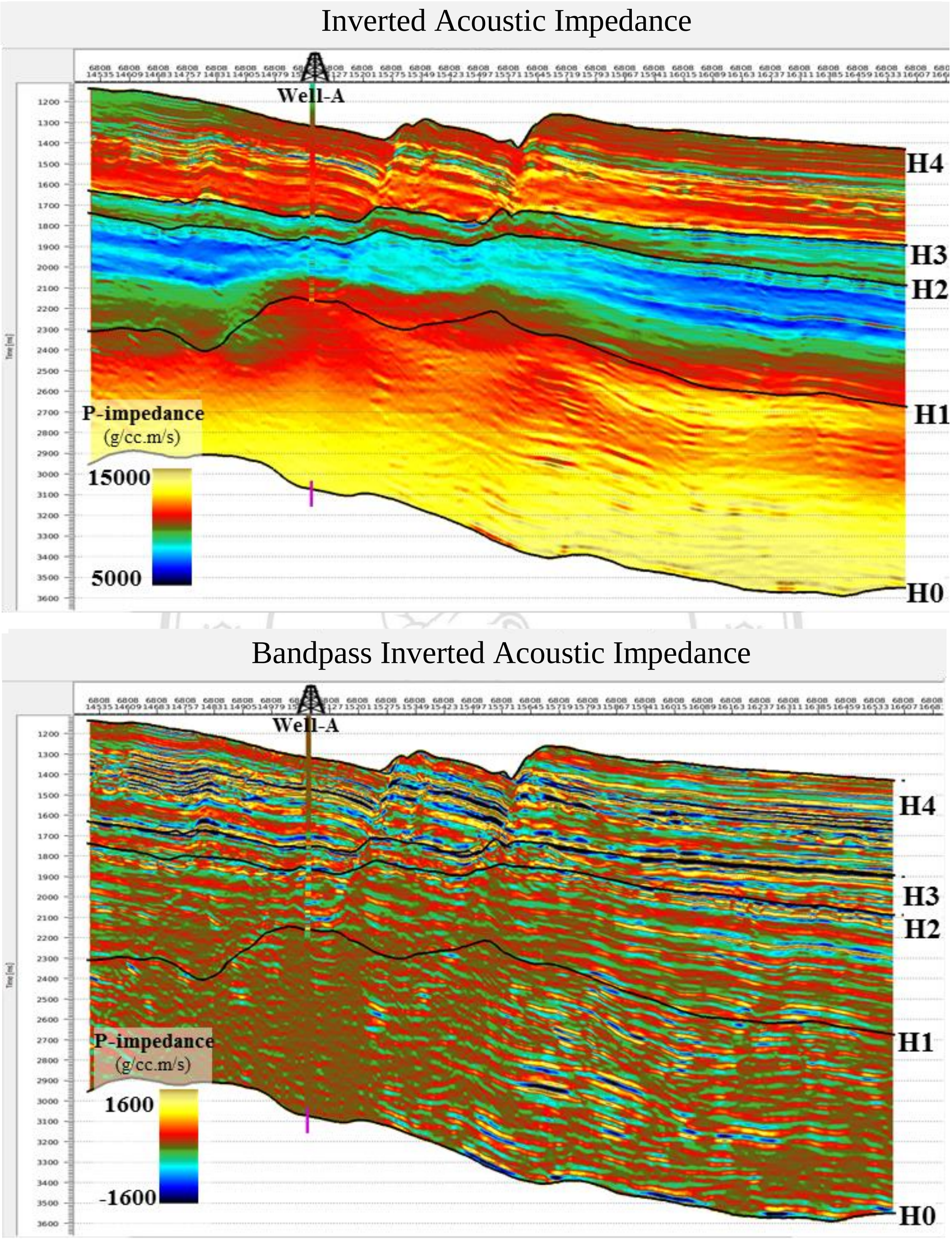

Figure C-12 Inline 6808 section of final absolute acoustic impedance comparing with acoustic impedance logs at Well-A (top). Bandpass filtering were applied to both inverted acoustic impedance and well data to create comparable relative inversion results (bottom).

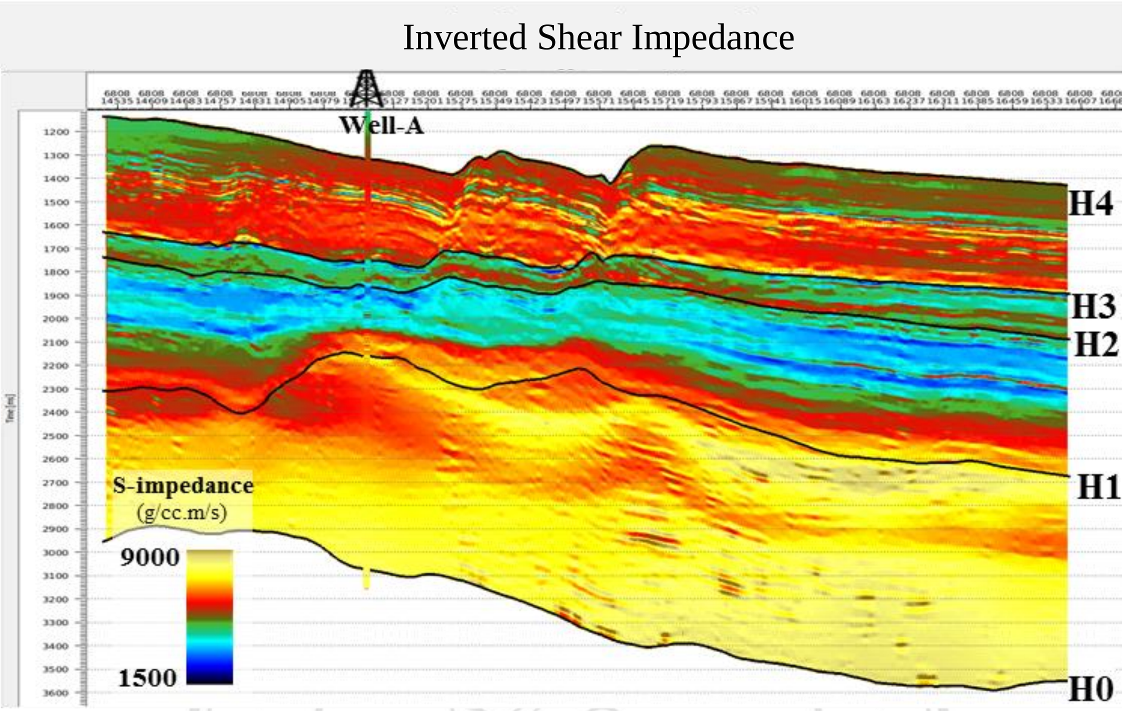

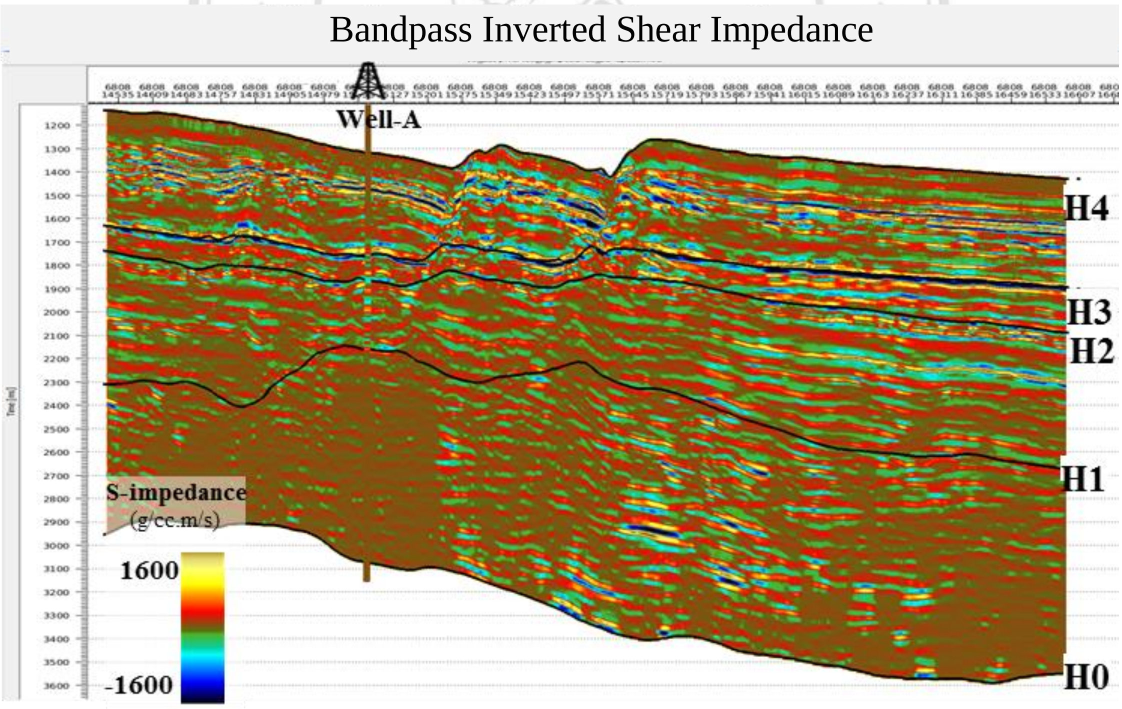

Figure C-13 Inline 6808 section of final absolute shear impedance comparing with shear impedance logs at Well-A (top). Bandpass filtering were applied to both inverted shear impedance and well data to create comparable relative inversion results (bottom).

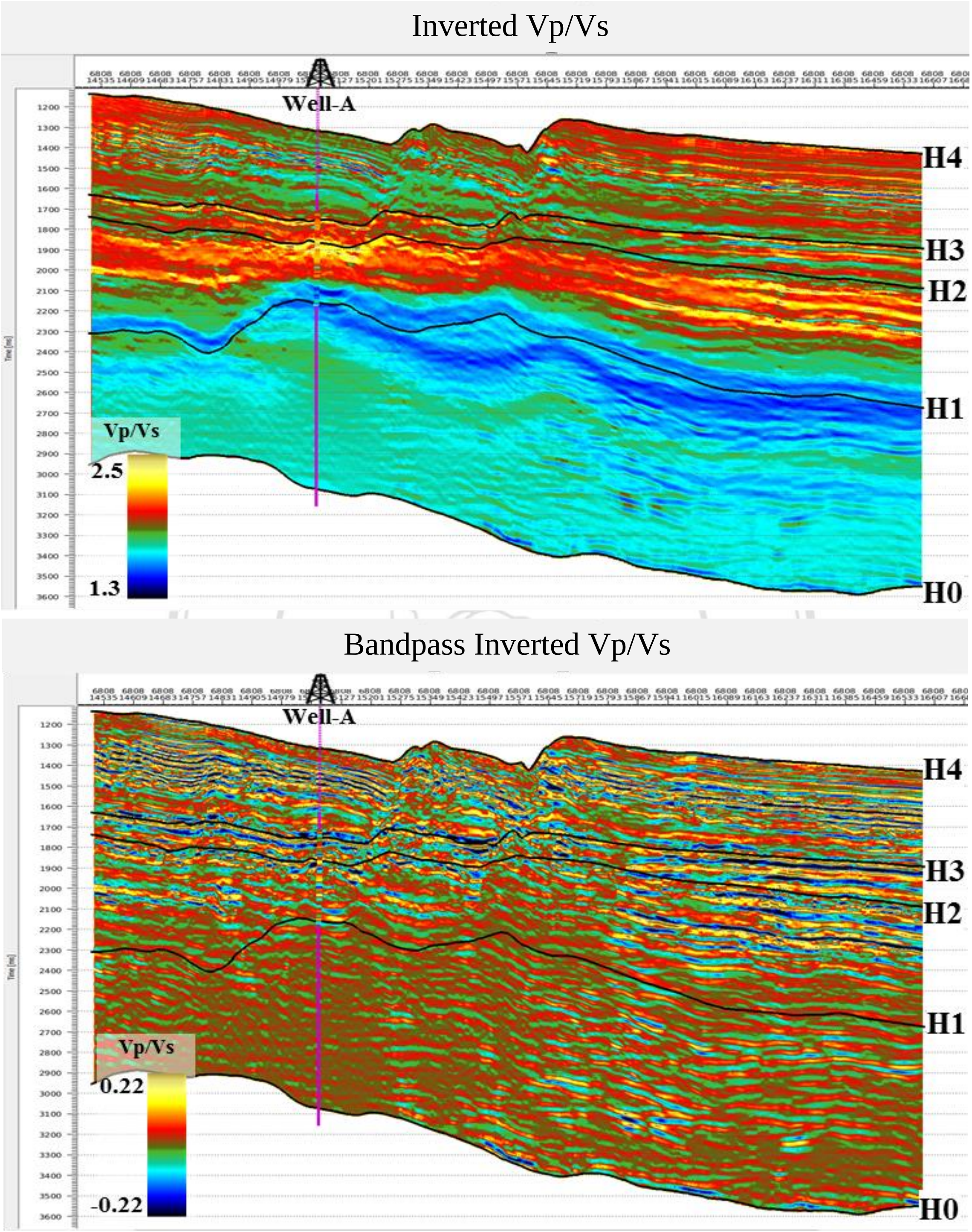

Figure C-14 Inline 6808 section of final absolute Vp/Vs comparing with Vp/Vs logs at Well-A (top). Bandpass filtering were applied to both inverted Vp/Vs and well data to create comparable relative inversion results (bottom).

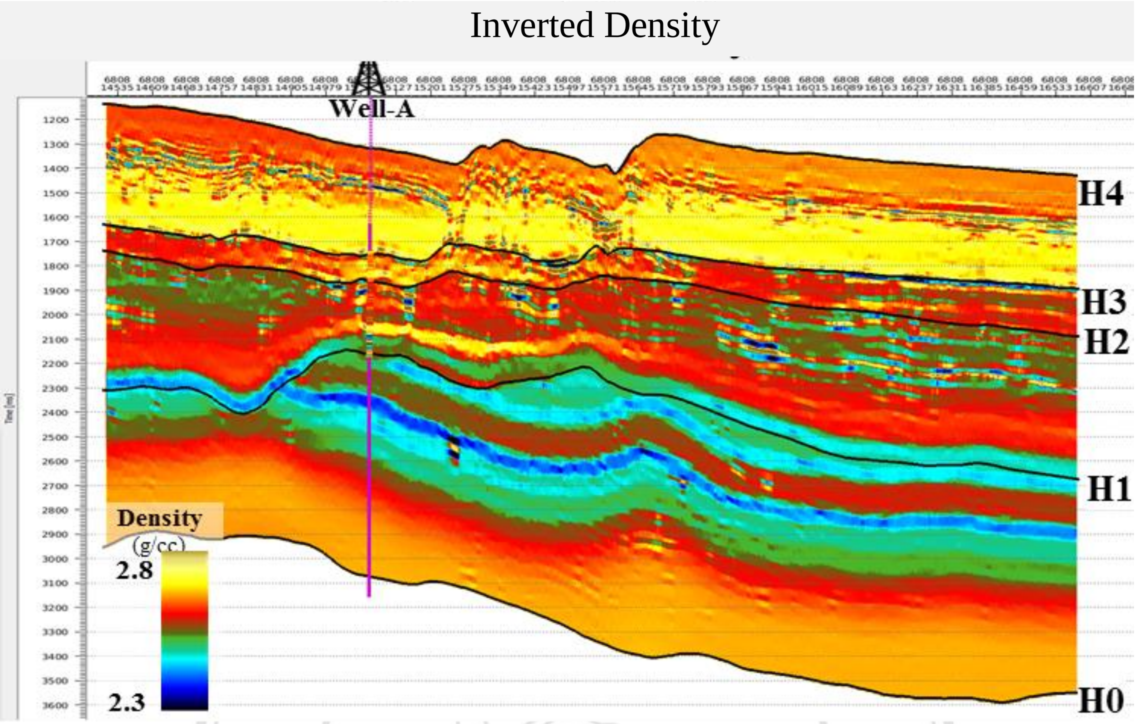

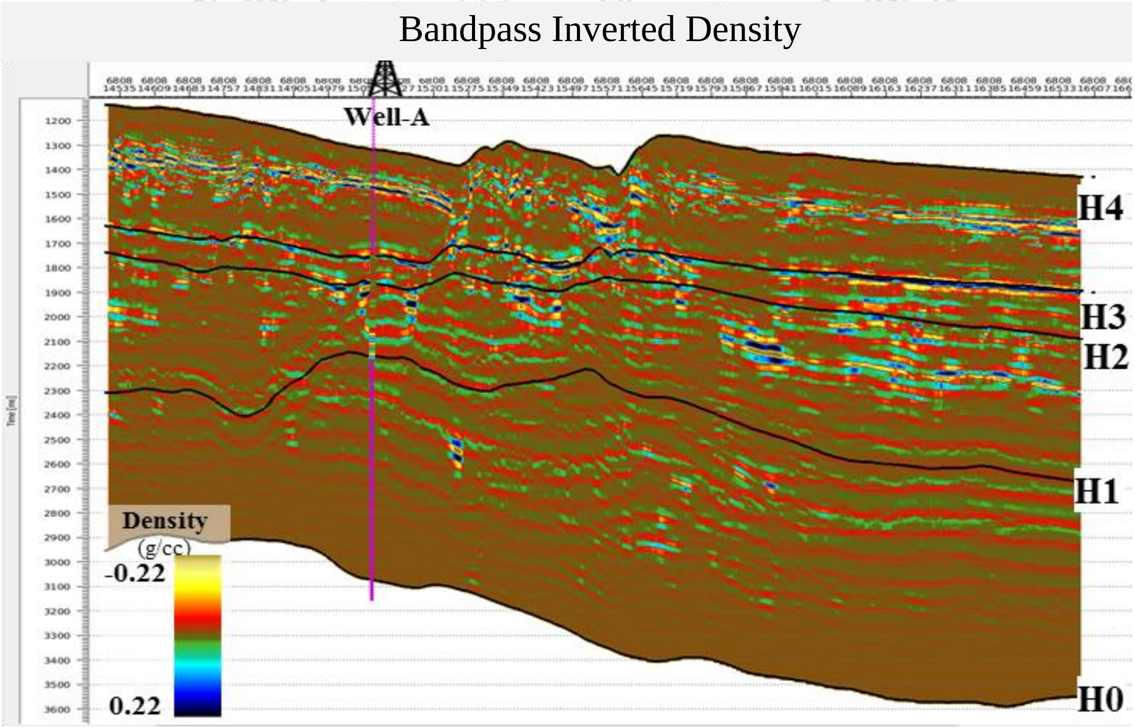

Figure C-15 Inline 6808 section of final absolute density comparing with density logs at Well-A (top). Bandpass filtering were applied to both inverted density and well data to create comparable relative inversion results (bottom).

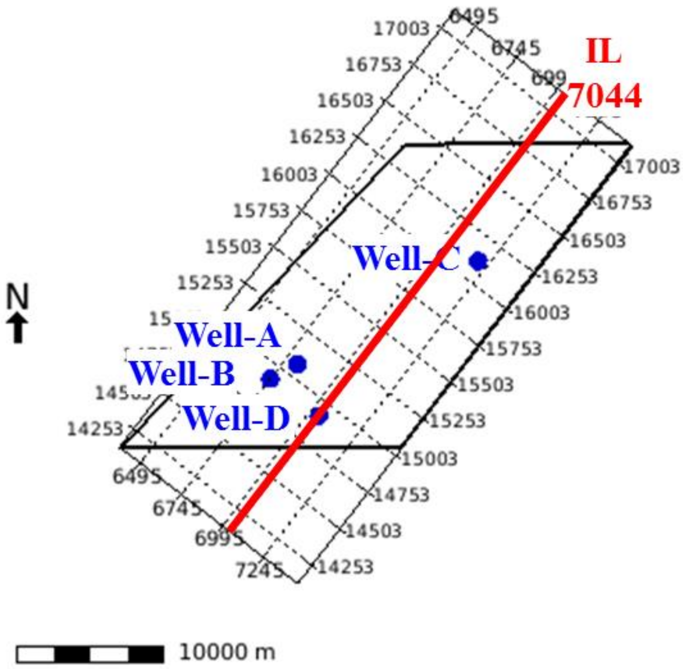

Figure C-16 Map location of inline 7044 that passed through Well-D location.

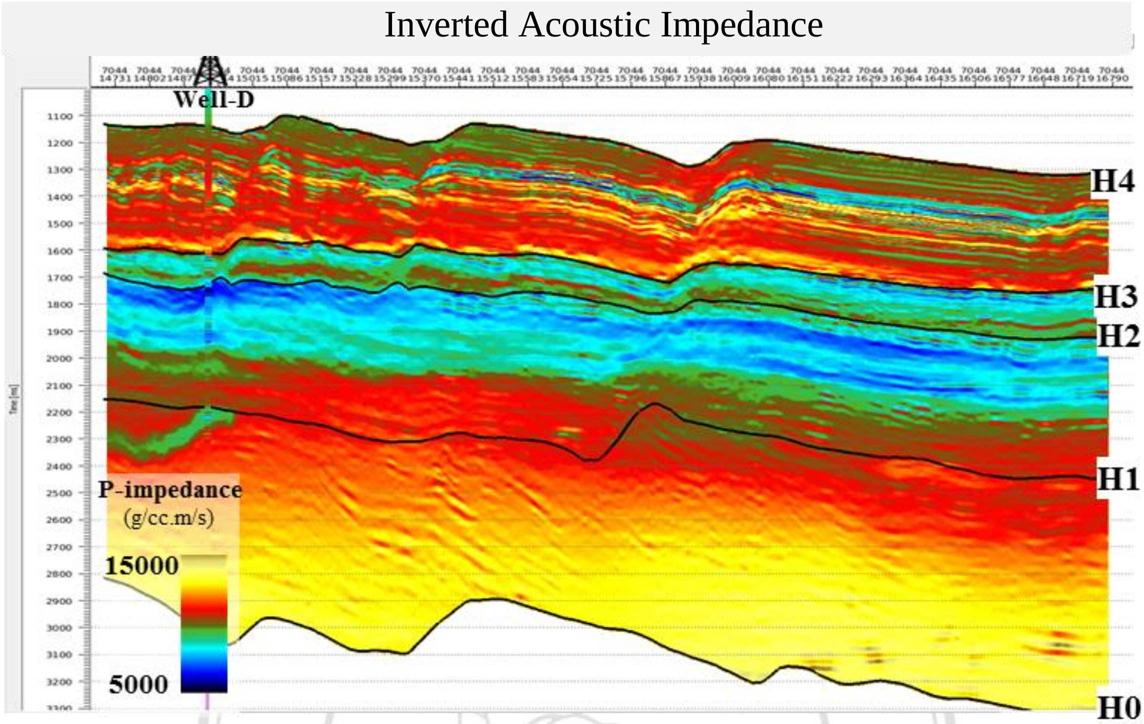

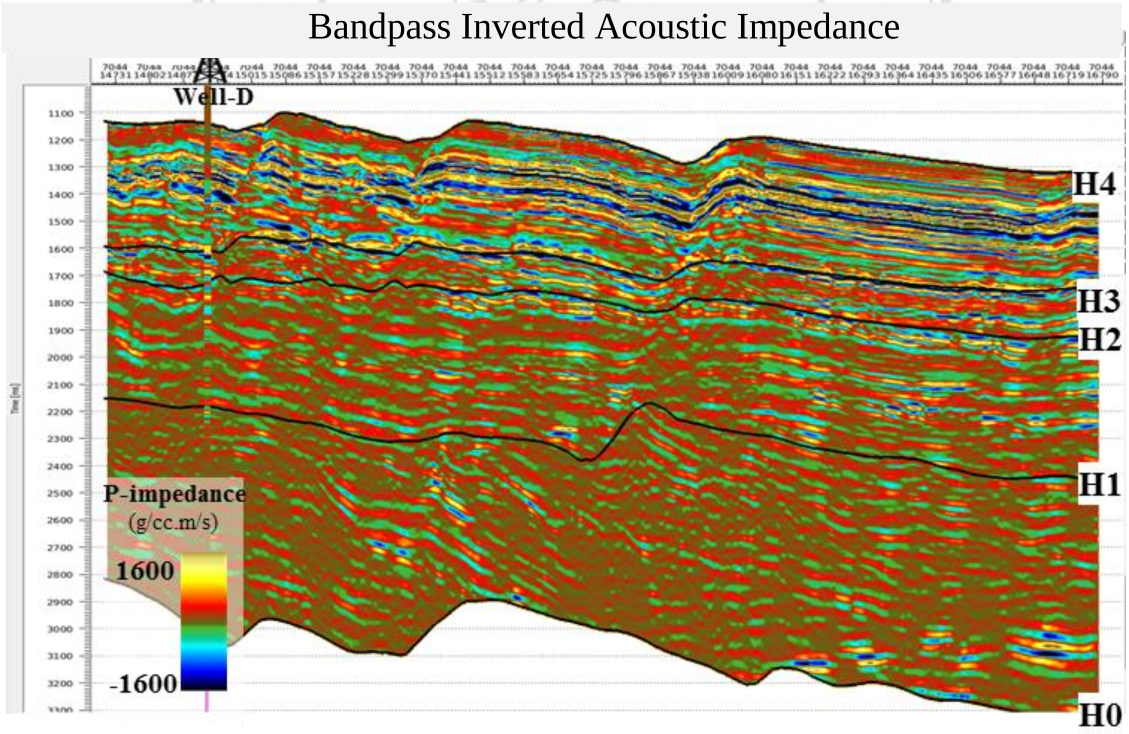

Figure C-17 Inline 7044 section of final absolute acoustic impedance comparing with acoustic impedance logs at Well-D (top). Bandpass filtering were applied to both inverted acoustic impedance and well data to create comparable relative inversion results (bottom).

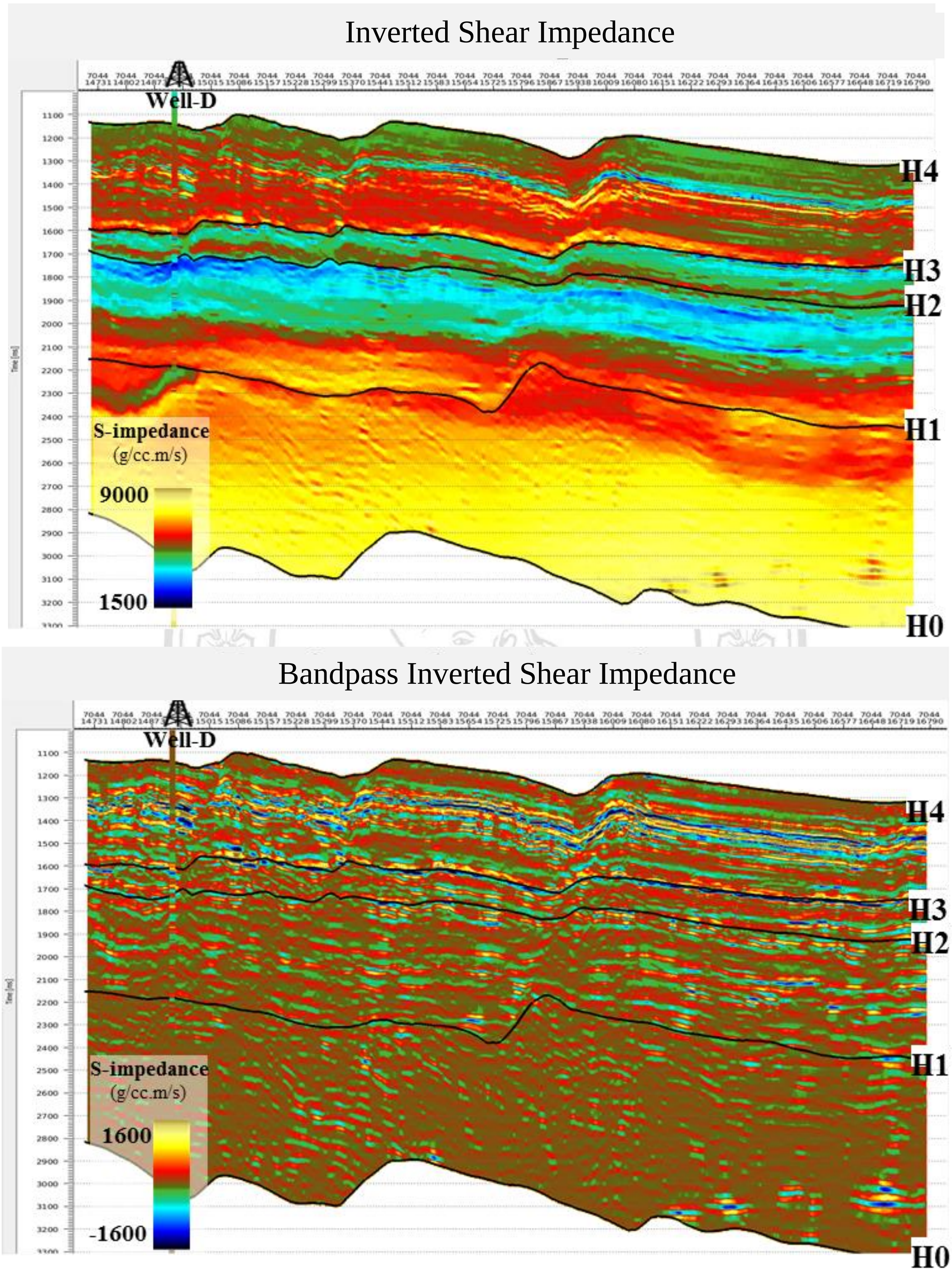

Figure C-18 Inline 7044 section of final absolute shear impedance comparing with shear impedance logs at Well-D (top). Bandpass filtering were applied to both inverted shear impedance and well data to create comparable relative inversion results (bottom).

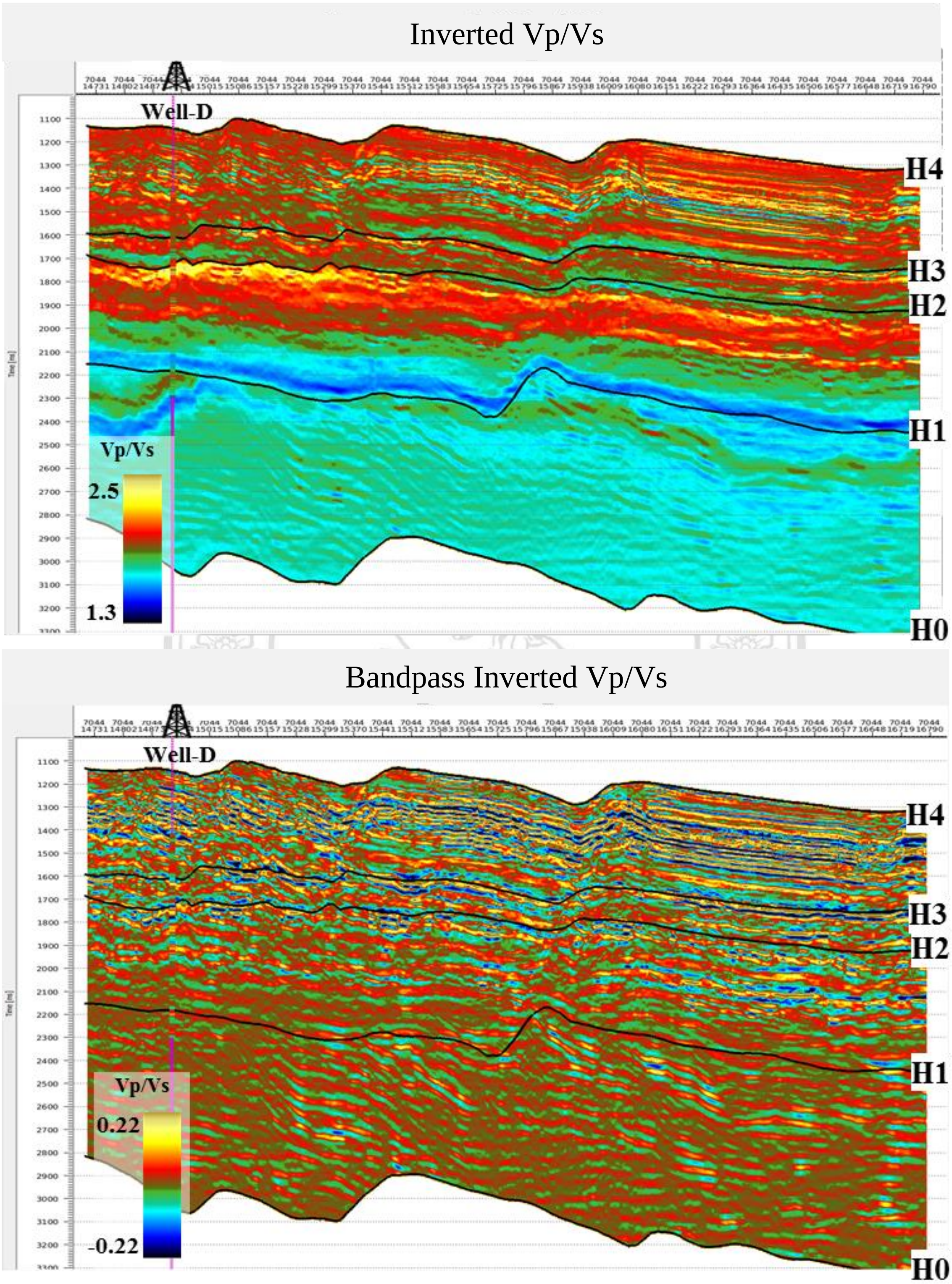

Figure C-19 Inline 7044 section of final absolute Vp/Vs comparing with Vp/Vs logs at Well-D (top). Bandpass filtering were applied to both inverted Vp/Vs and well data to create comparable relative inversion results (bottom).

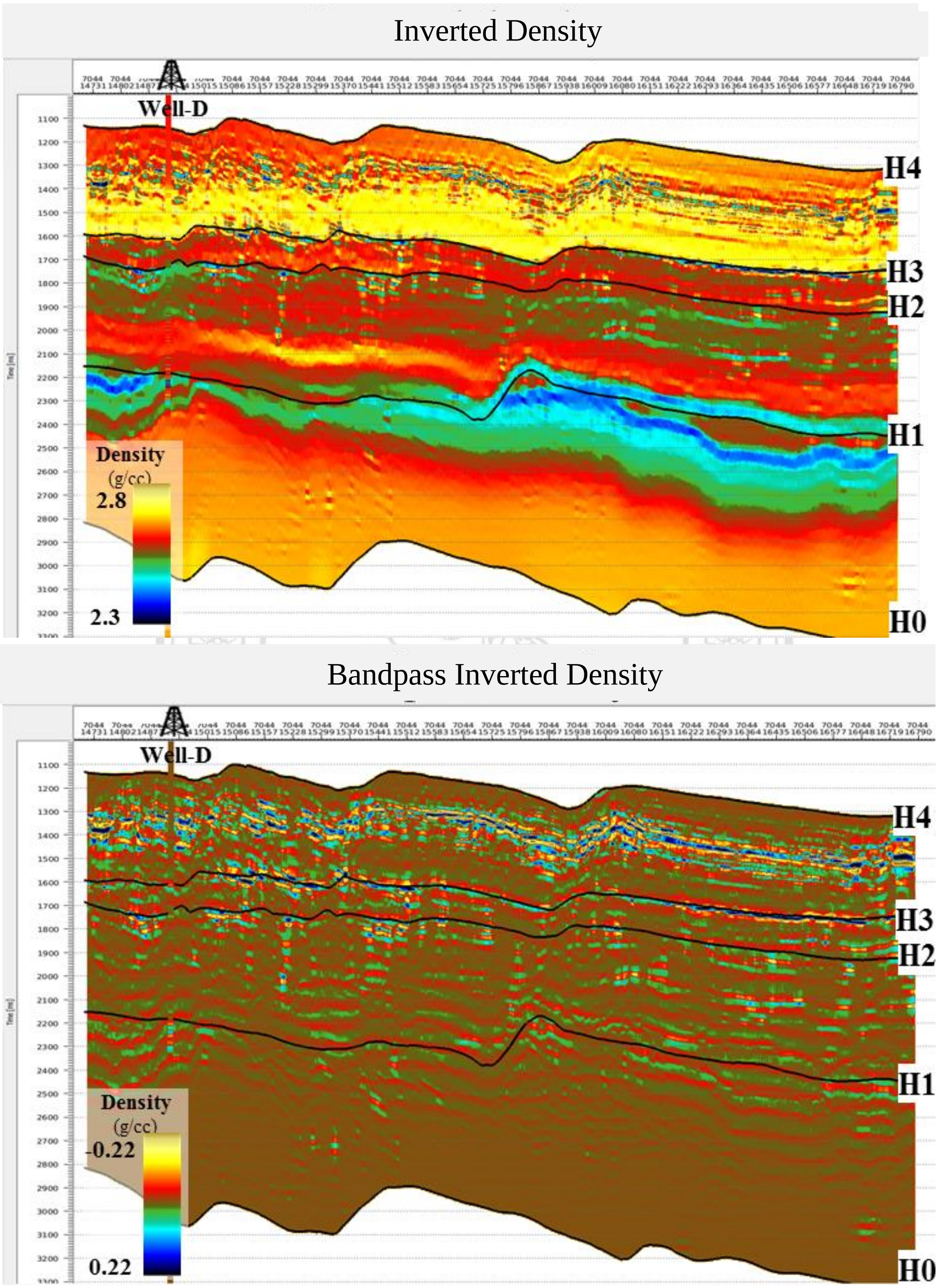

Figure C-20 Inline 7044 section of final absolute density comparing with density logs at Well-D (top). Bandpass filtering were applied to both inverted density and well data to create comparable relative inversion results (bottom).

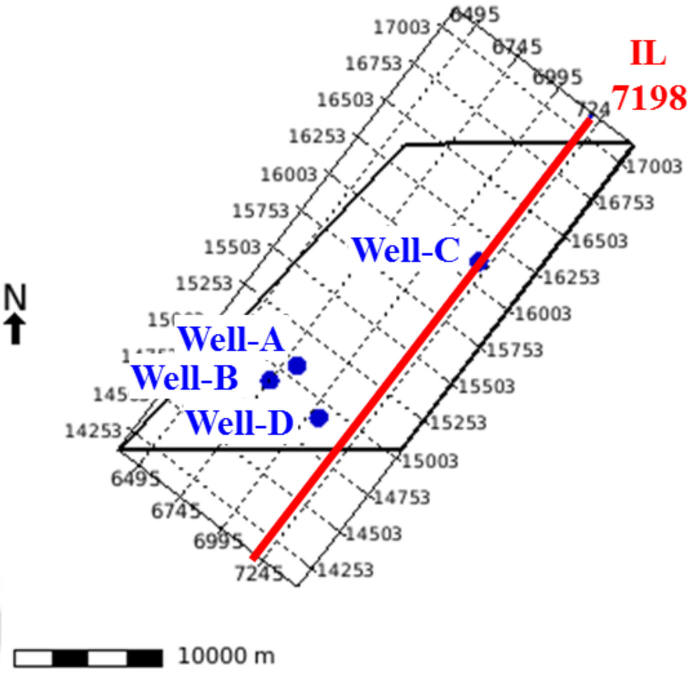

Figure C-21 Map location of inline 7198 that passed through Well-C location.

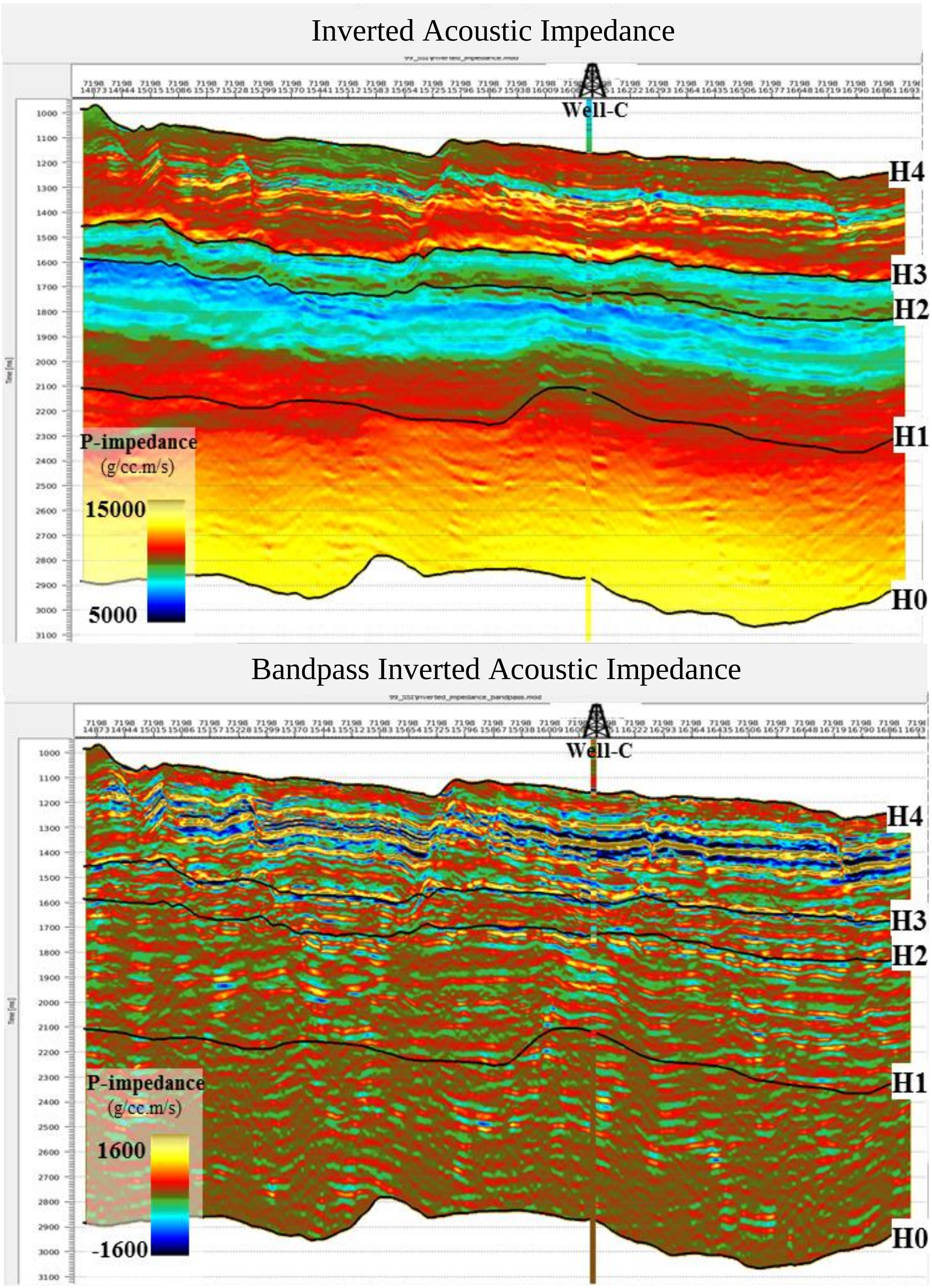

Figure C-22 Inline 7198 section of final absolute acoustic impedance comparing with acoustic impedance logs at Well-C (top). Bandpass filtering were applied to both inverted acoustic impedance and well data to create comparable relative inversion results (bottom).

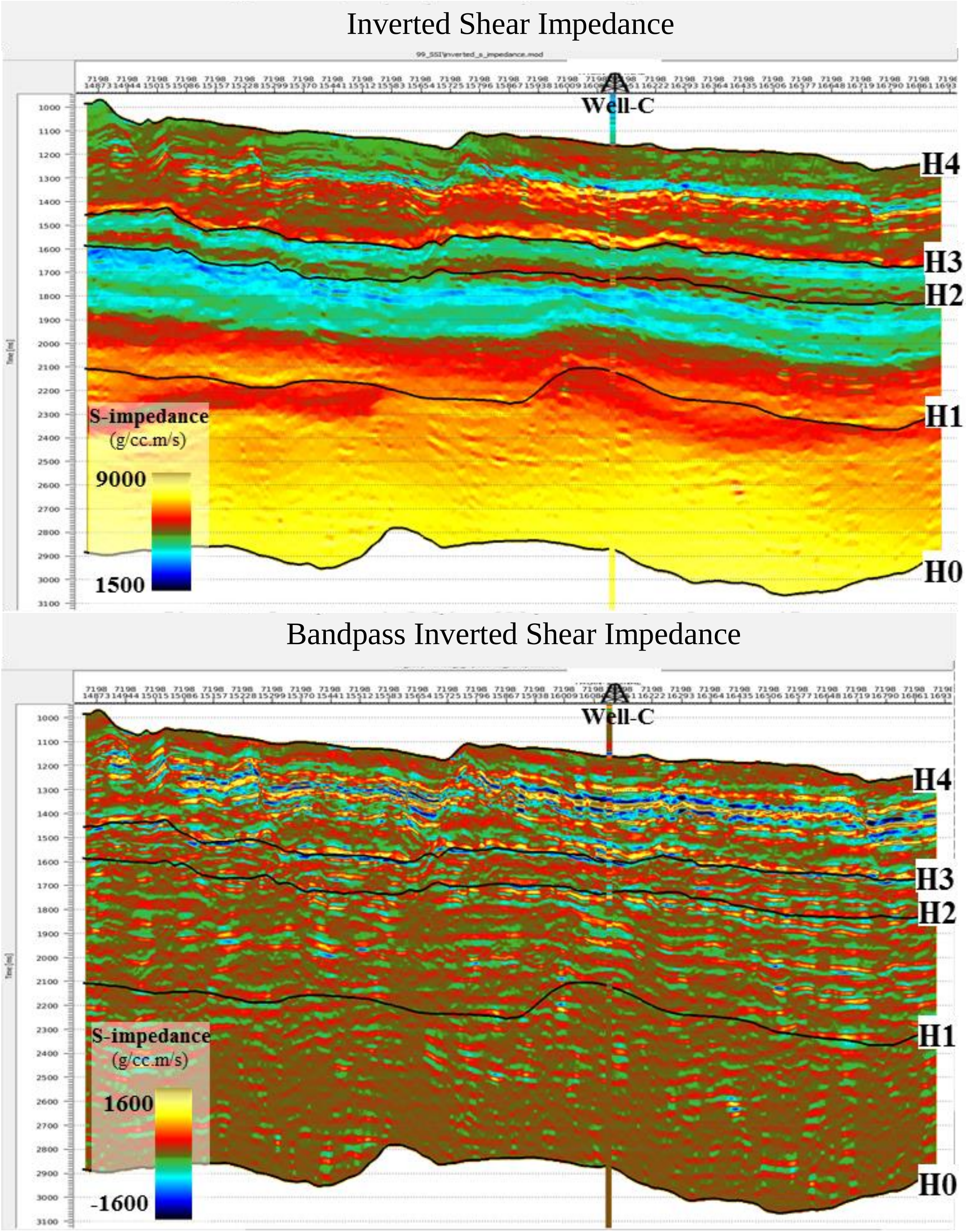

Figure C-23 Inline 7198 section of final absolute shear impedance comparing with shear impedance logs at Well-C (top). Bandpass filtering were applied to both inverted shear impedance and well data to create comparable relative inversion results (bottom).

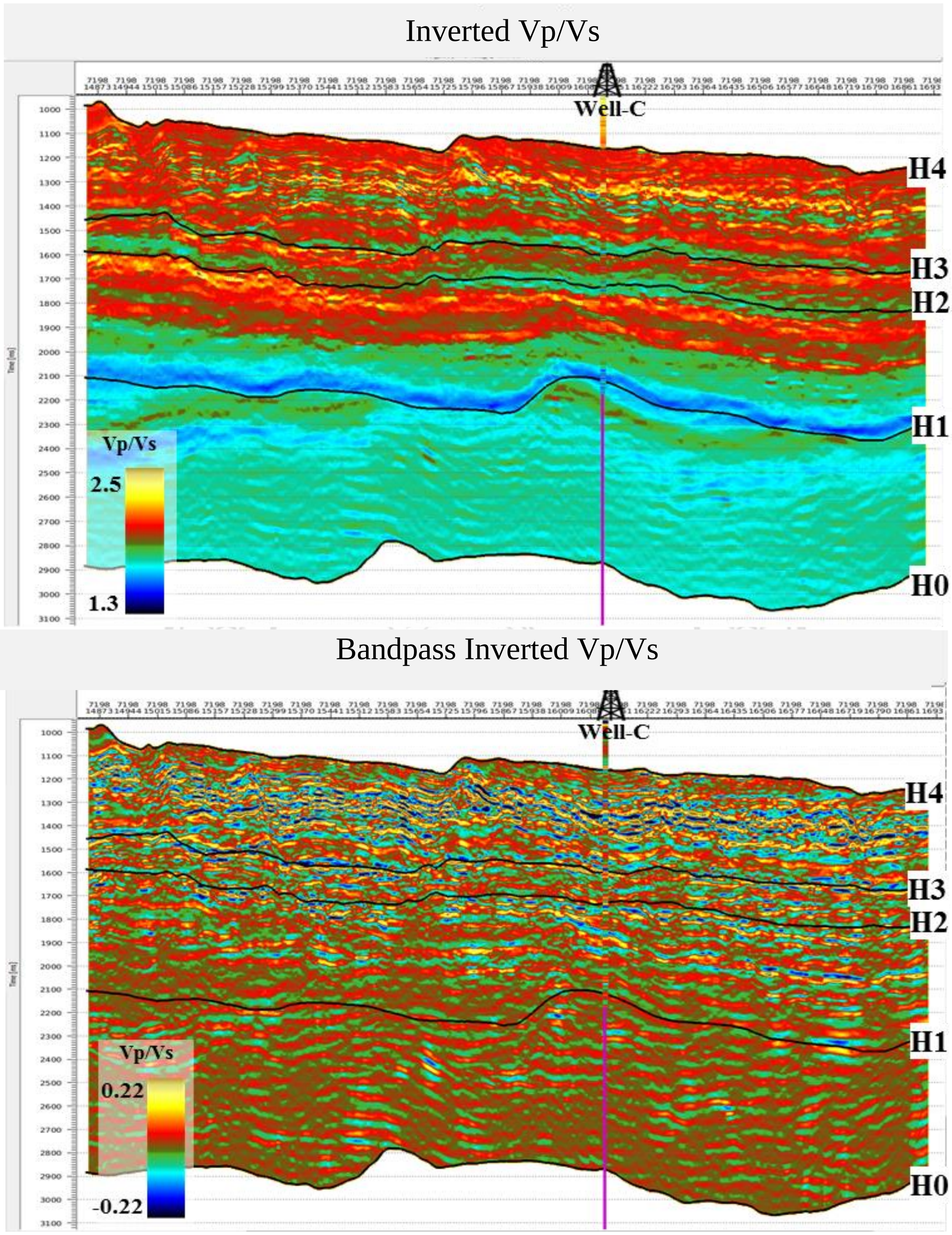

Figure C-24 Inline 7198 section of final absolute Vp/Vs comparing with Vp/Vs logs at Well-C (top). Bandpass filtering were applied to both inverted Vp/Vs and well data to create comparable relative inversion results (bottom).

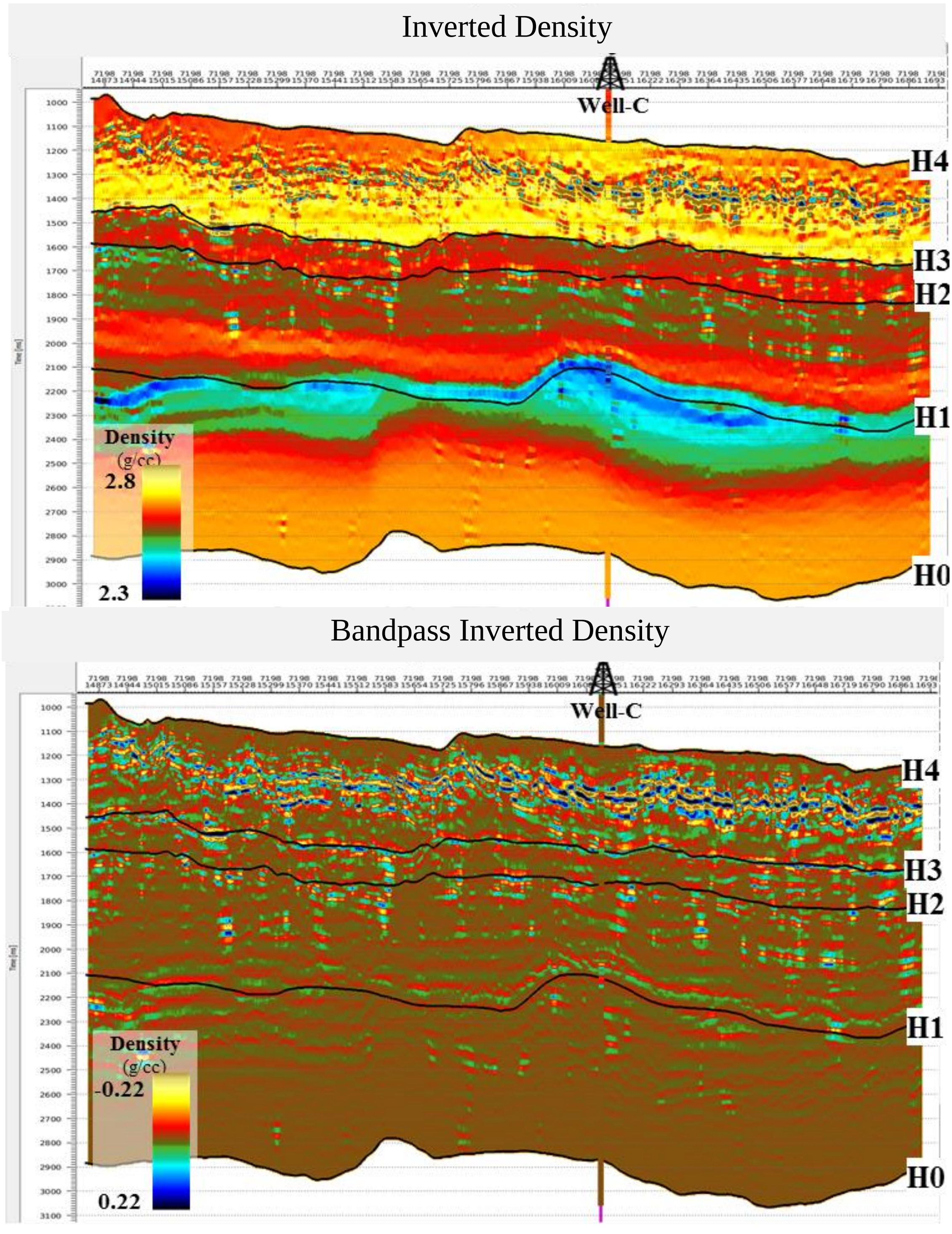

Figure C-25 Inline 7198 section of final absolute density comparing with density logs at Well-C (top). Bandpass filtering were applied to both inverted density and well data to create comparable relative inversion results (bottom).

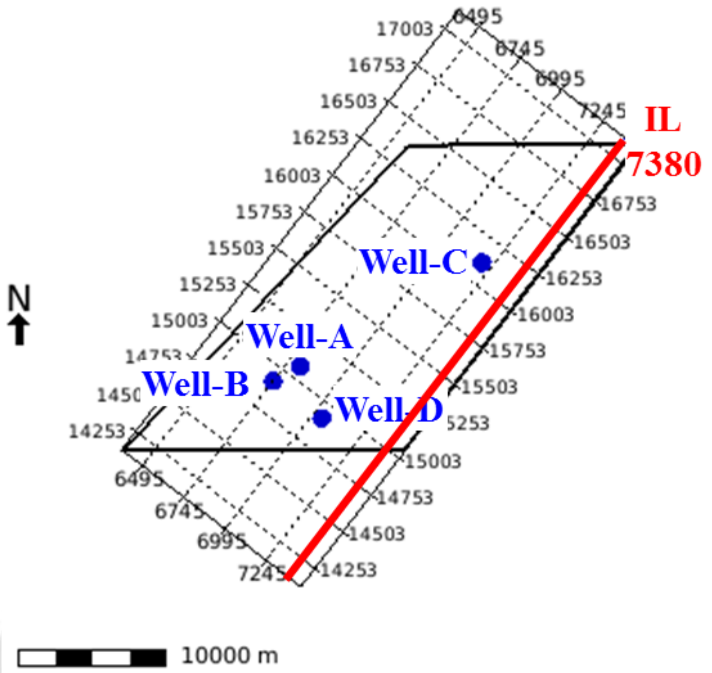

Figure C-26 Map location of inline 7380.

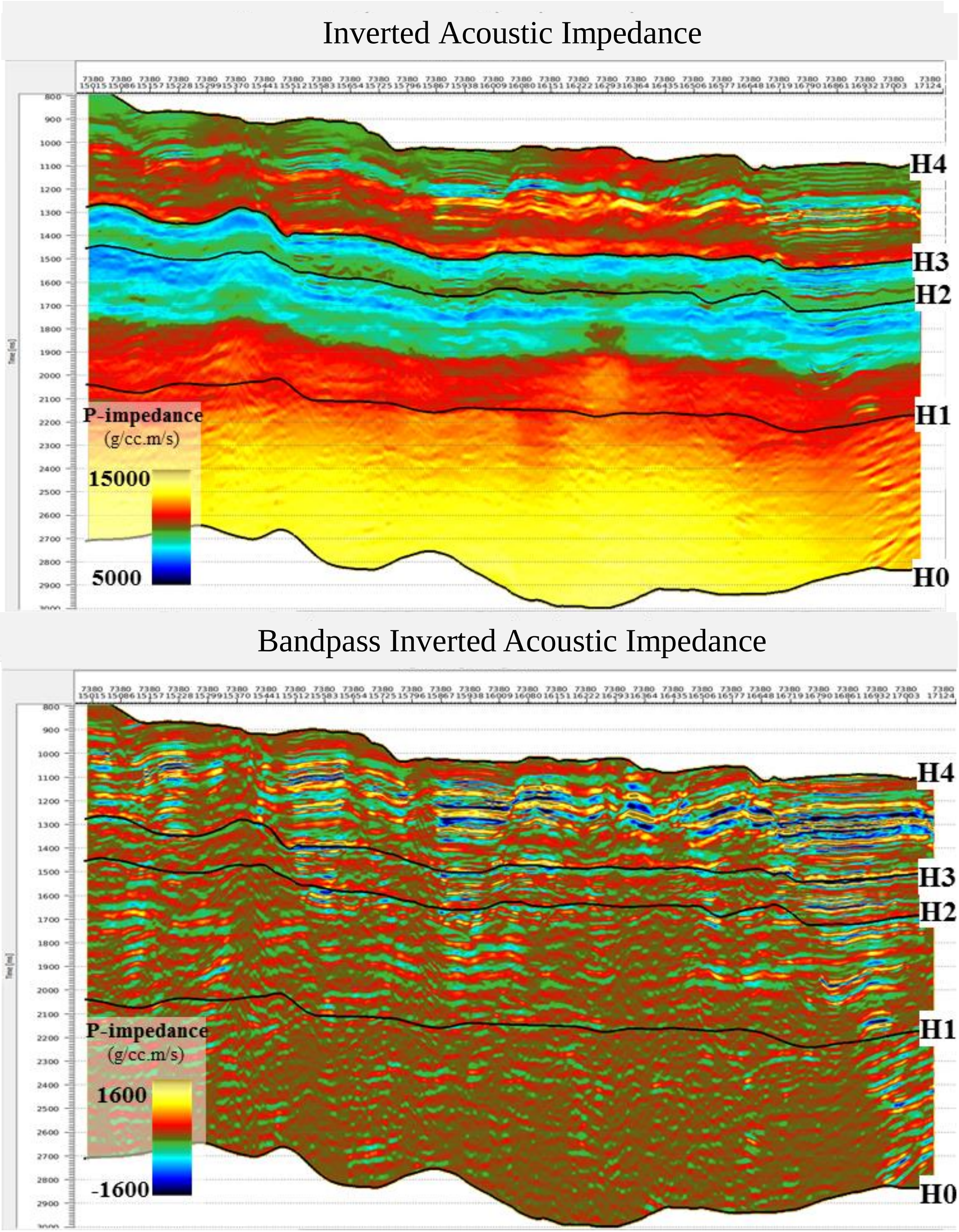

Figure C-27 Inline 7380 section of final absolute acoustic impedance (top) and bandpass filtering were applied to inverted acoustic impedance to create comparable relative inversion results (bottom).

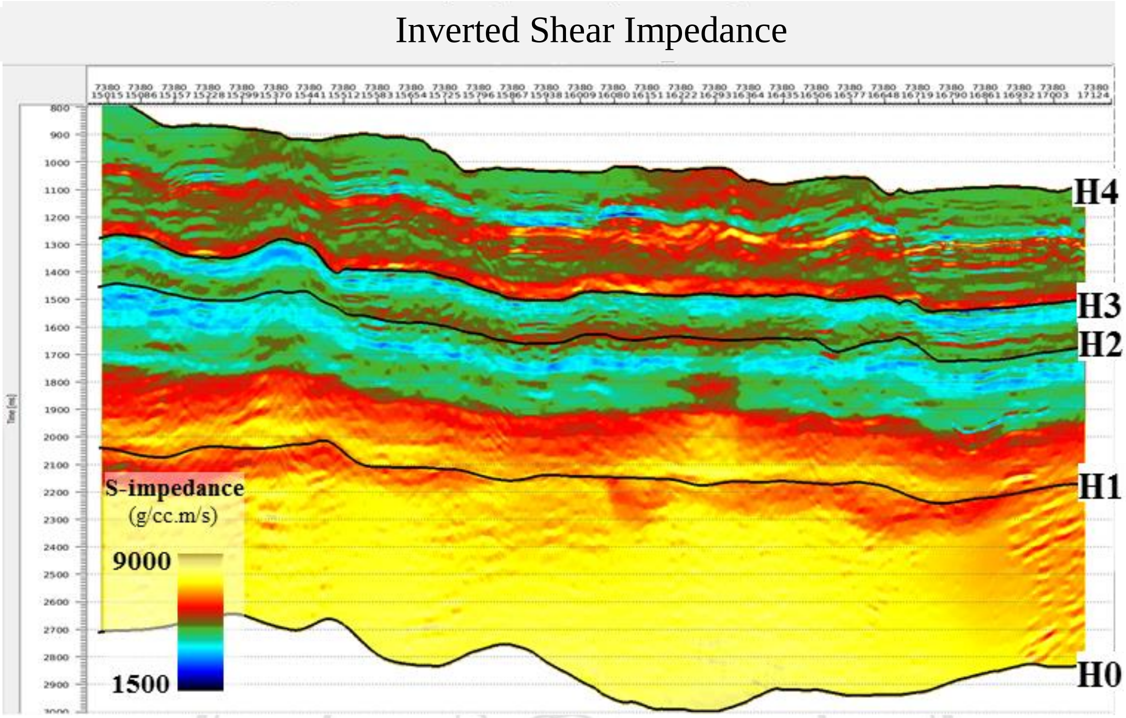

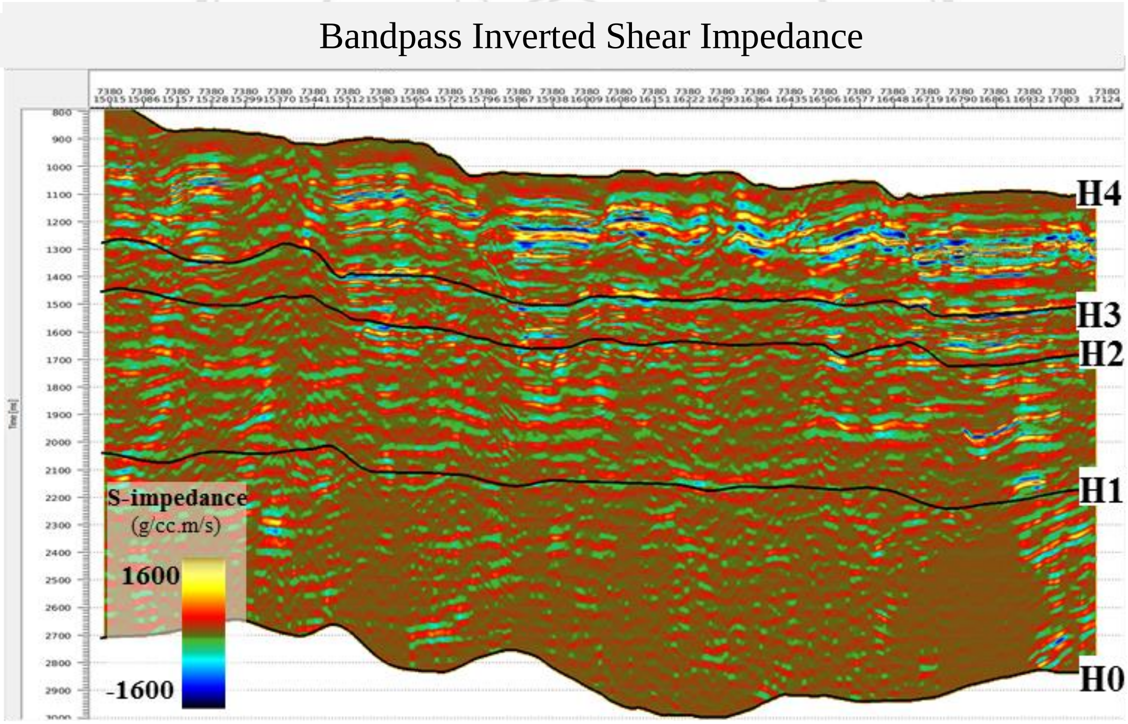

Figure C-28 Inline 7380 section of final absolute shear impedance (top) and bandpass filtering were applied to inverted shear impedance to create comparable relative inversion results (bottom).

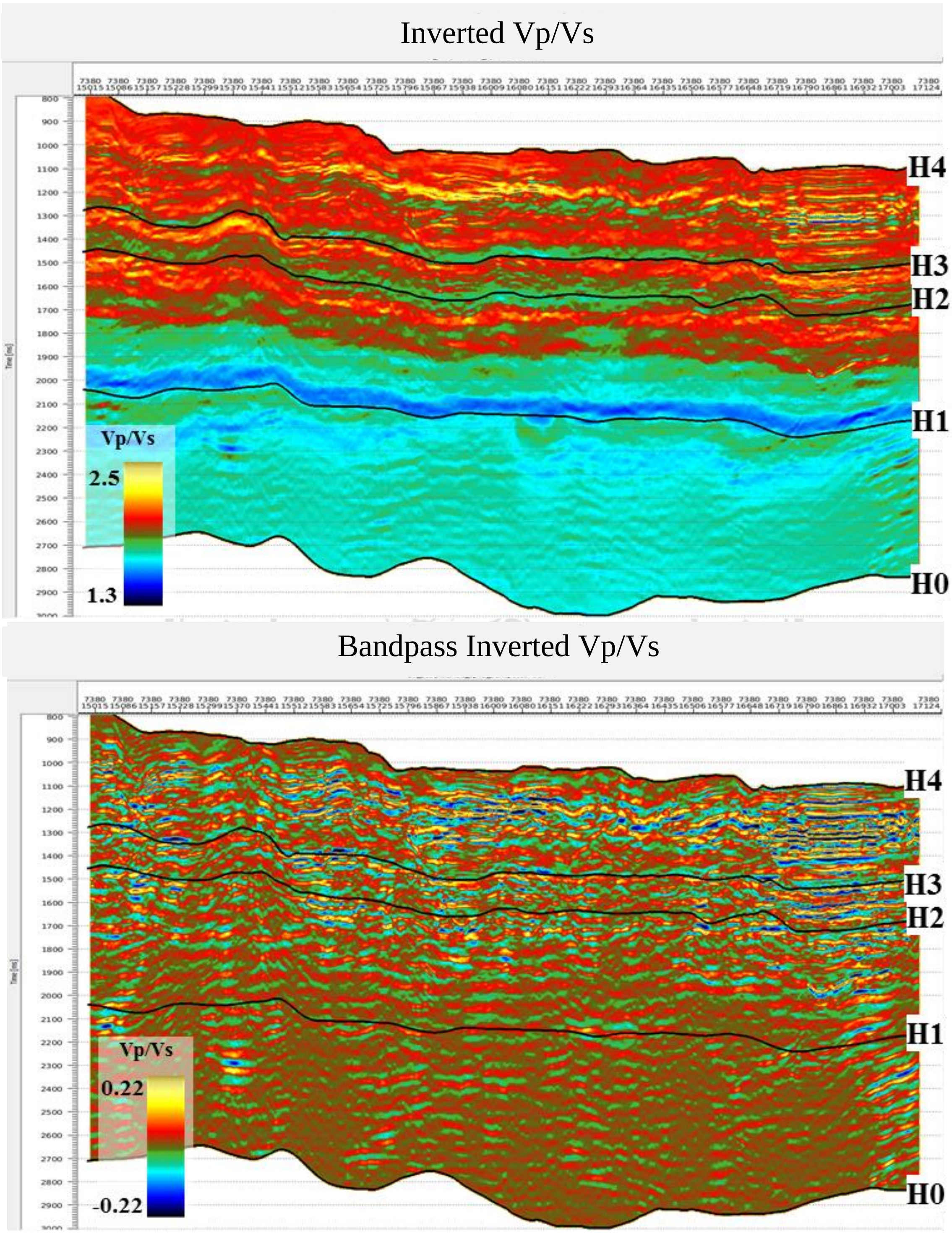

Figure C-29 Inline 7380 section of final absolute Vp/Vs (top) and bandpass filtering were applied to inverted Vp/Vs to create comparable relative inversion results (bottom).

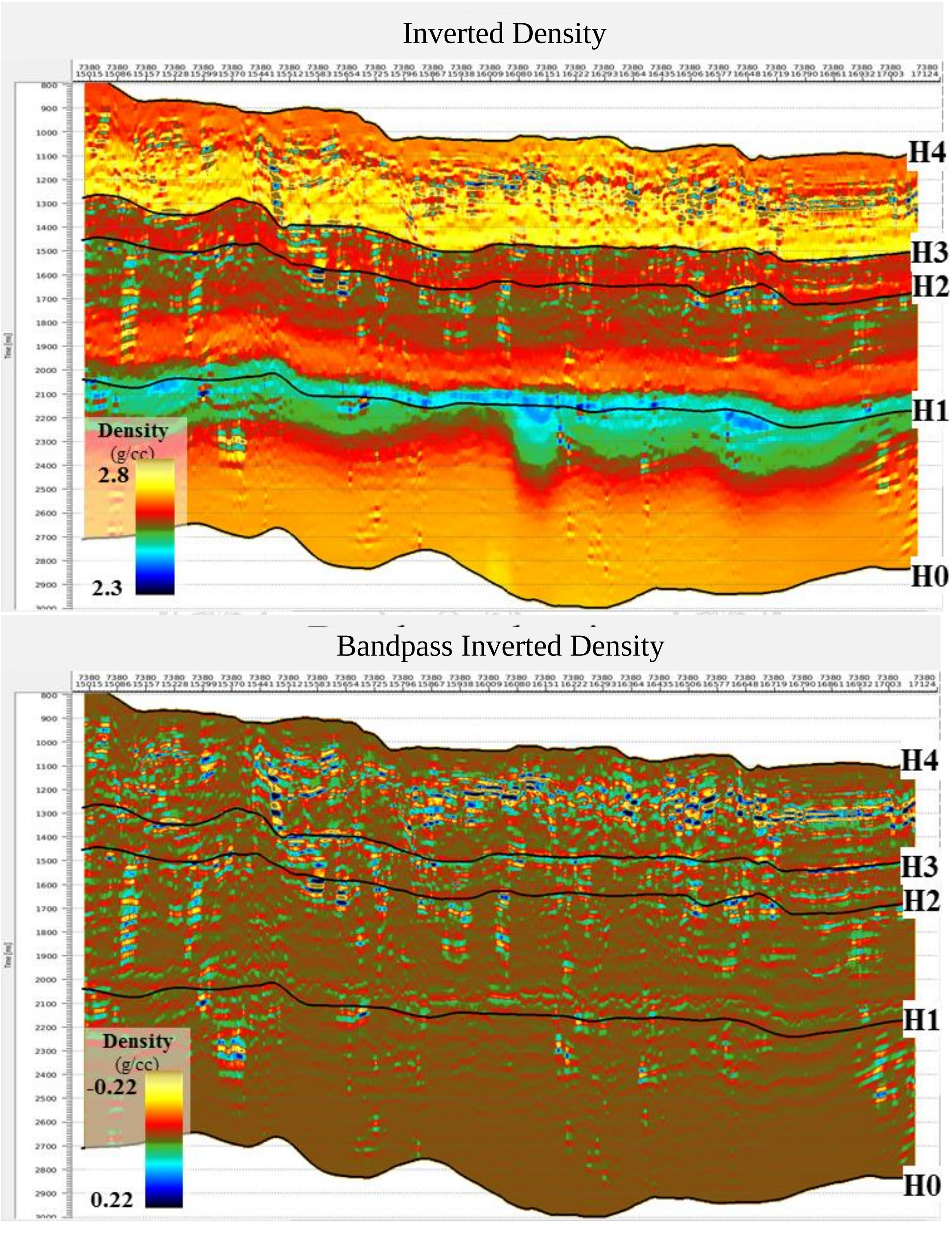

Figure C-30 Inline 7380 section of final absolute density (top) and bandpass filtering were applied to inverted density to create comparable relative inversion results (bottom).

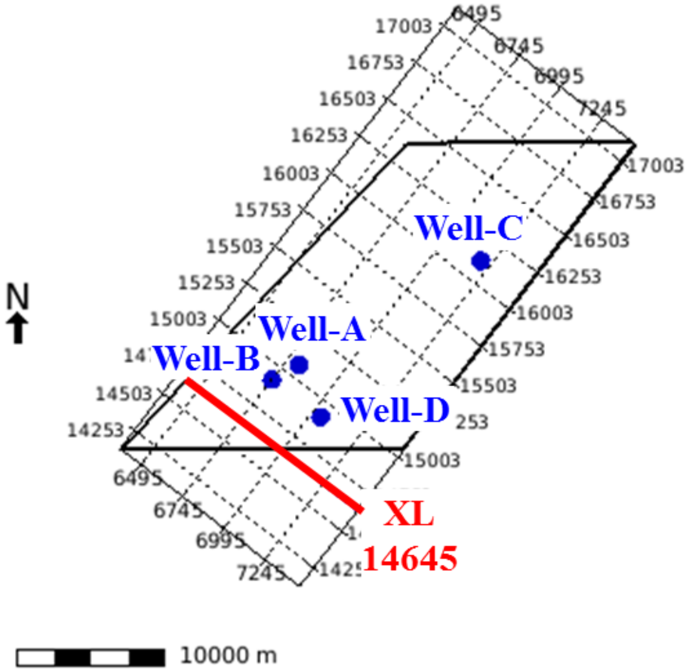

Figure C-31 Map location of crossline 14645.

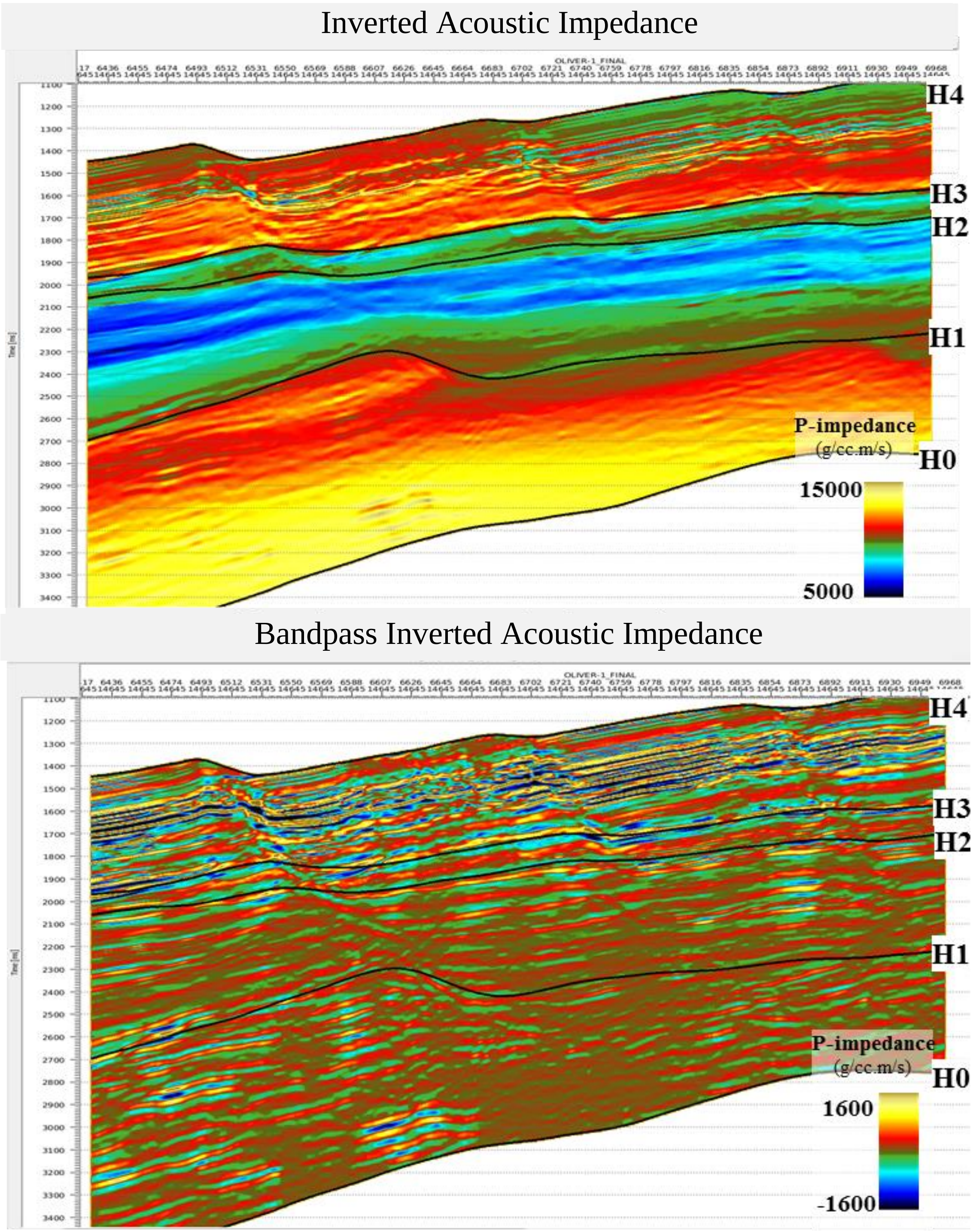

Figure C-32 Crossline 14645 section of final absolute acoustic impedance (top) and bandpass filtering were applied to inverted acoustic impedance to create comparable relative inversion results (bottom).

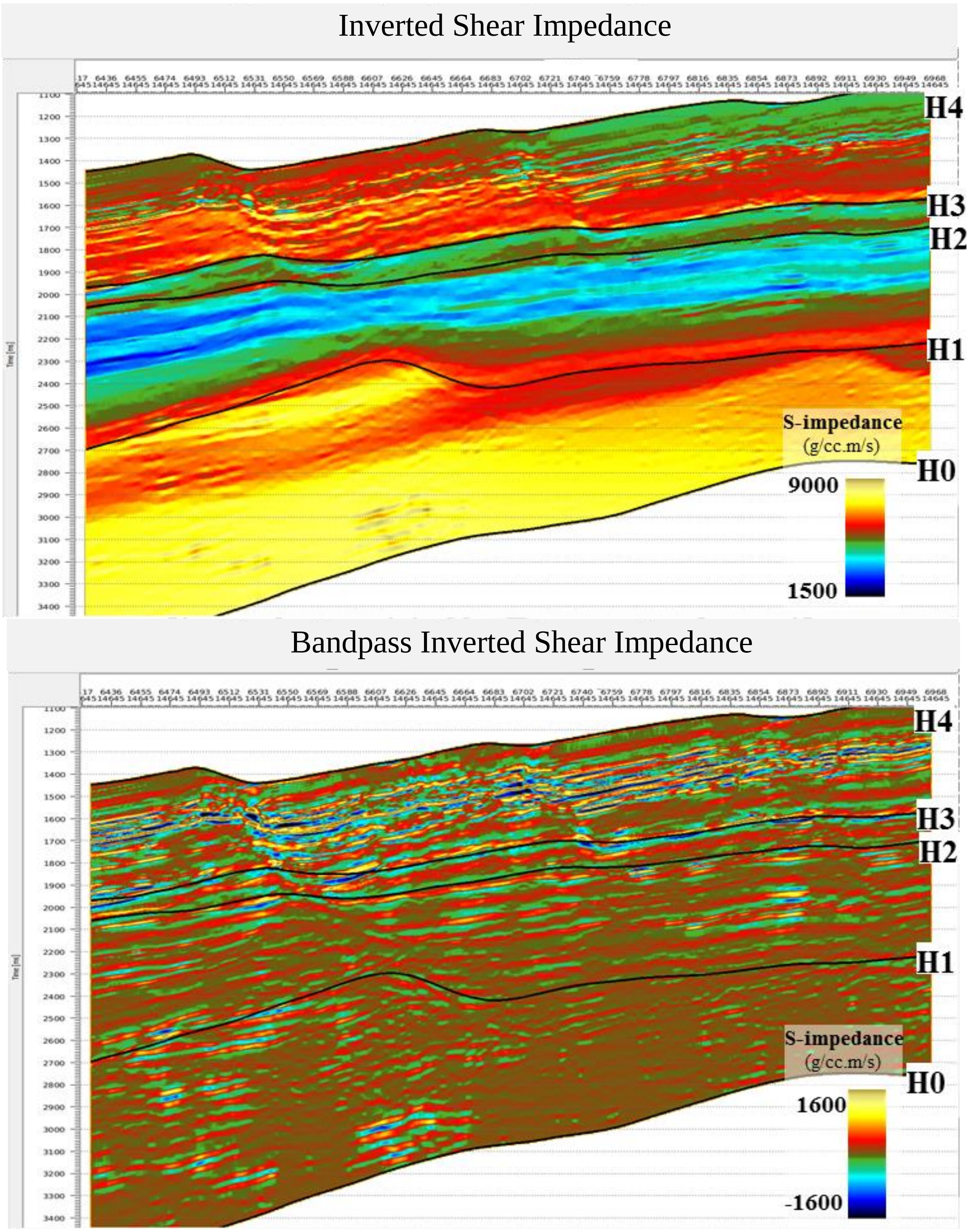

Figure C-33 Crossline 14645 section of final absolute shear impedance (top) and bandpass filtering were applied to inverted shear impedance to create comparable relative inversion results (bottom).

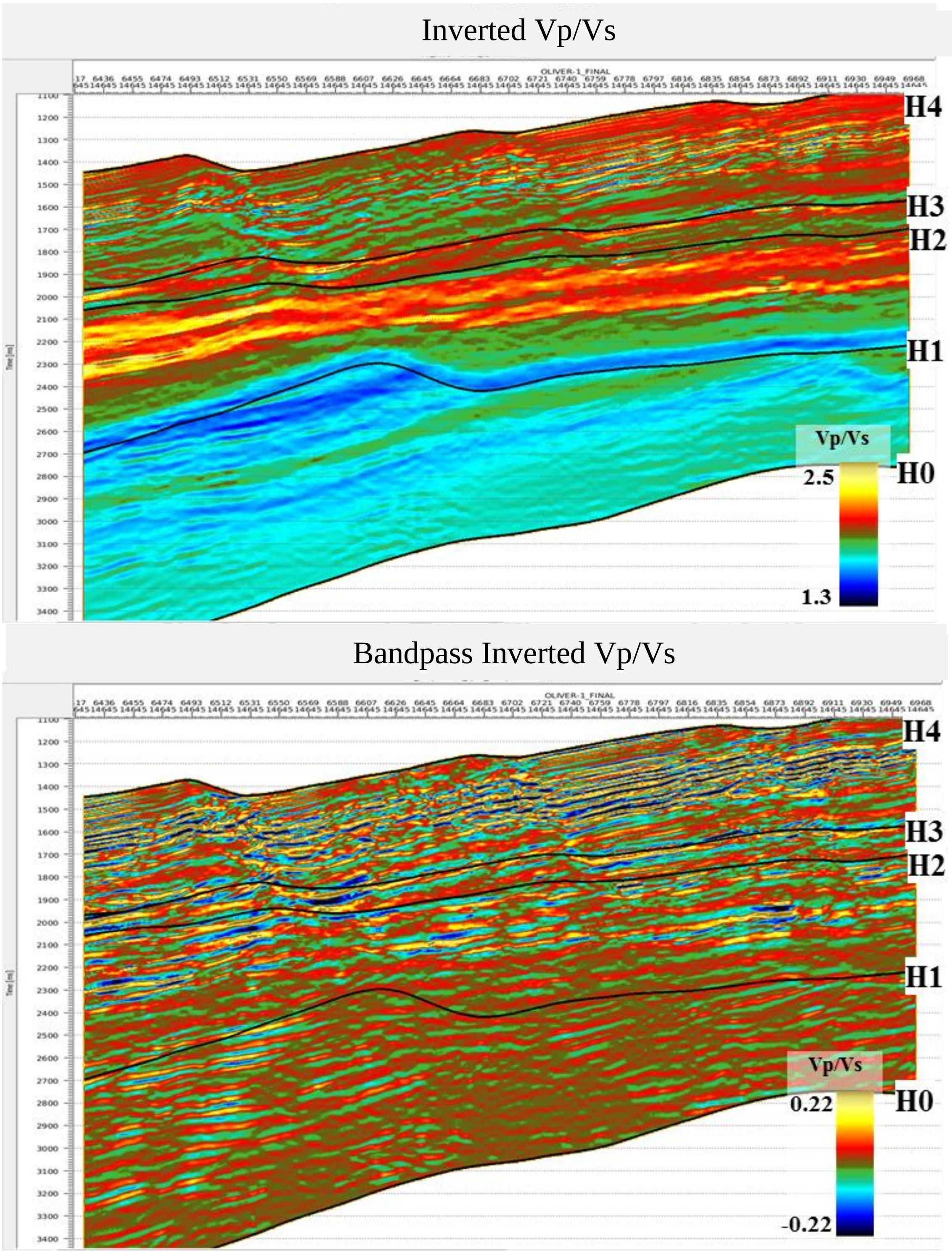

Figure C-34 Crossline 14645 section of final absolute Vp/Vs (top) and bandpass filtering were applied to inverted Vp/Vs to create comparable relative inversion results (bottom).

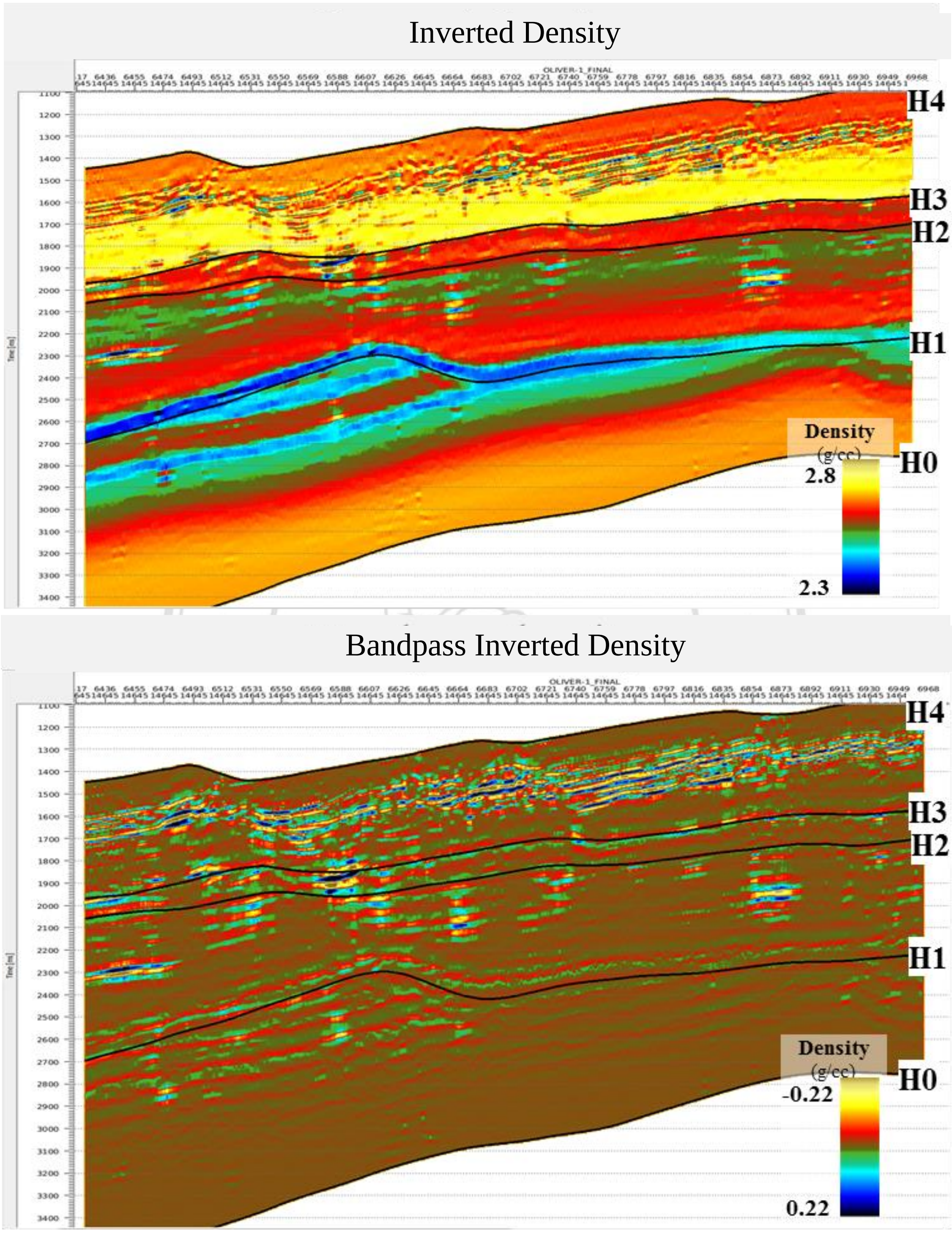

Figure C-35 Crossline 14645 section of final absolute density (top) and bandpass filtering were applied to inverted density to create comparable relative inversion results (bottom).

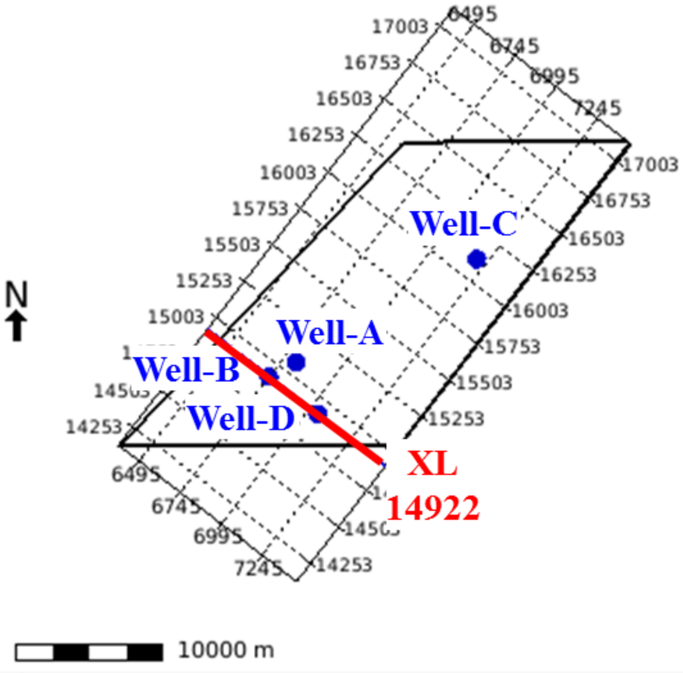

Figure C-36 Map location of crossline 14922 that passed through Wells-B and -C location.

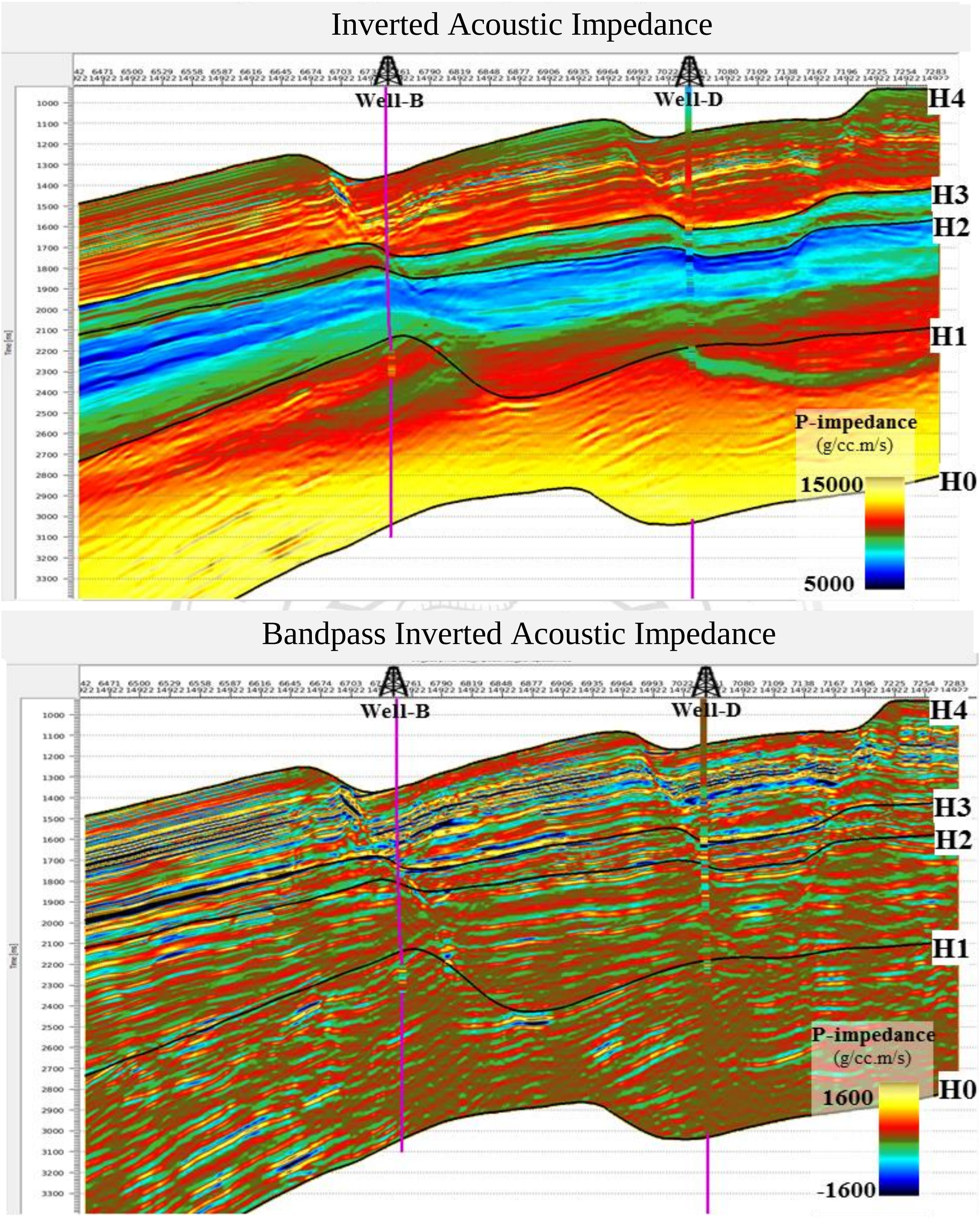

Figure C-37 Crossline 14922 section of final absolute acoustic impedance comparing with acoustic impedance logs at Wells-B and -D (top). Bandpass filtering were applied to both inverted acoustic impedance and well data to create comparable relative inversion results (bottom).

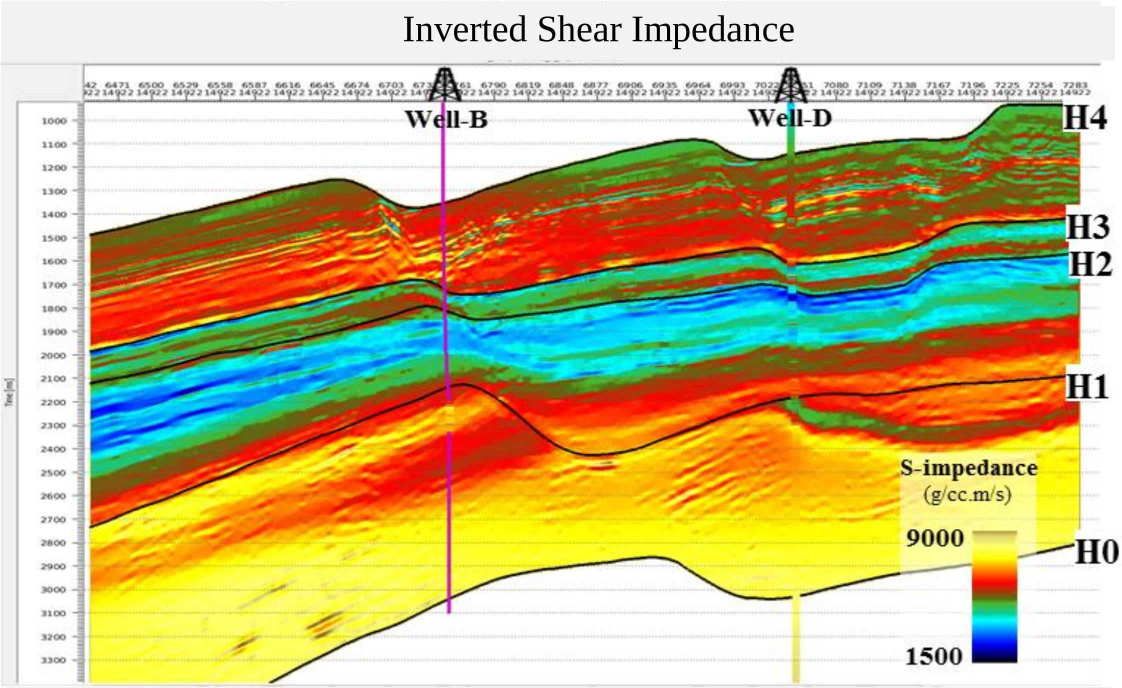

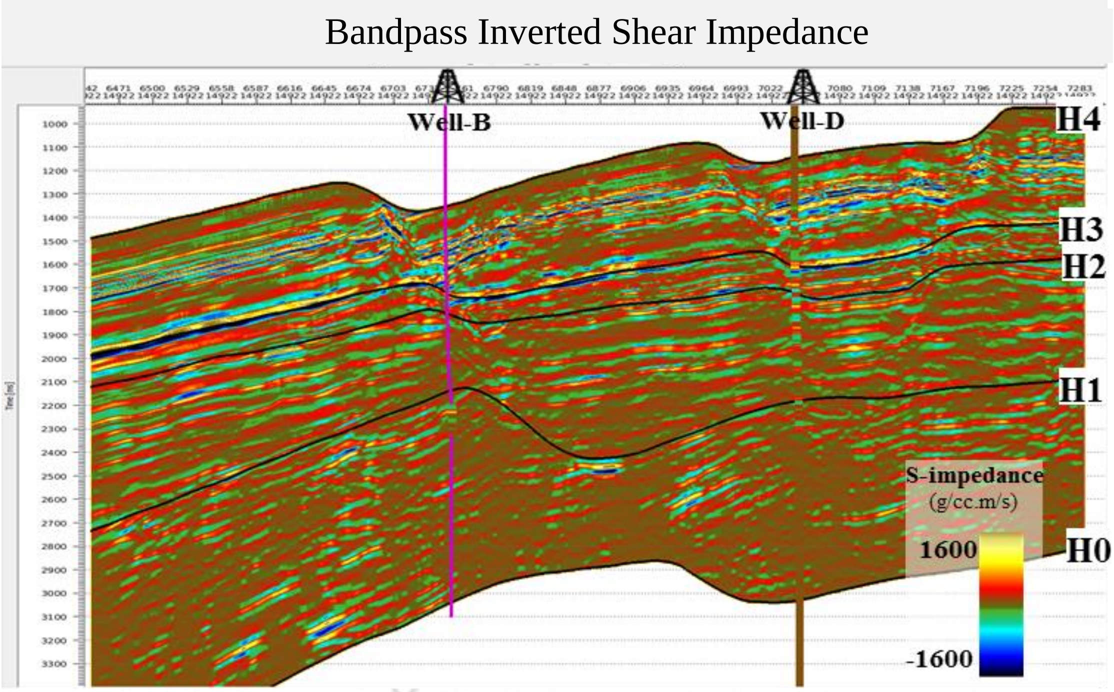

Figure C-38 Crossline 14922 section of final absolute shear impedance comparing with shear impedance logs at Wells-B and -D (top). Bandpass filtering were applied to both inverted shear impedance and well data to create comparable relative inversion results (bottom).

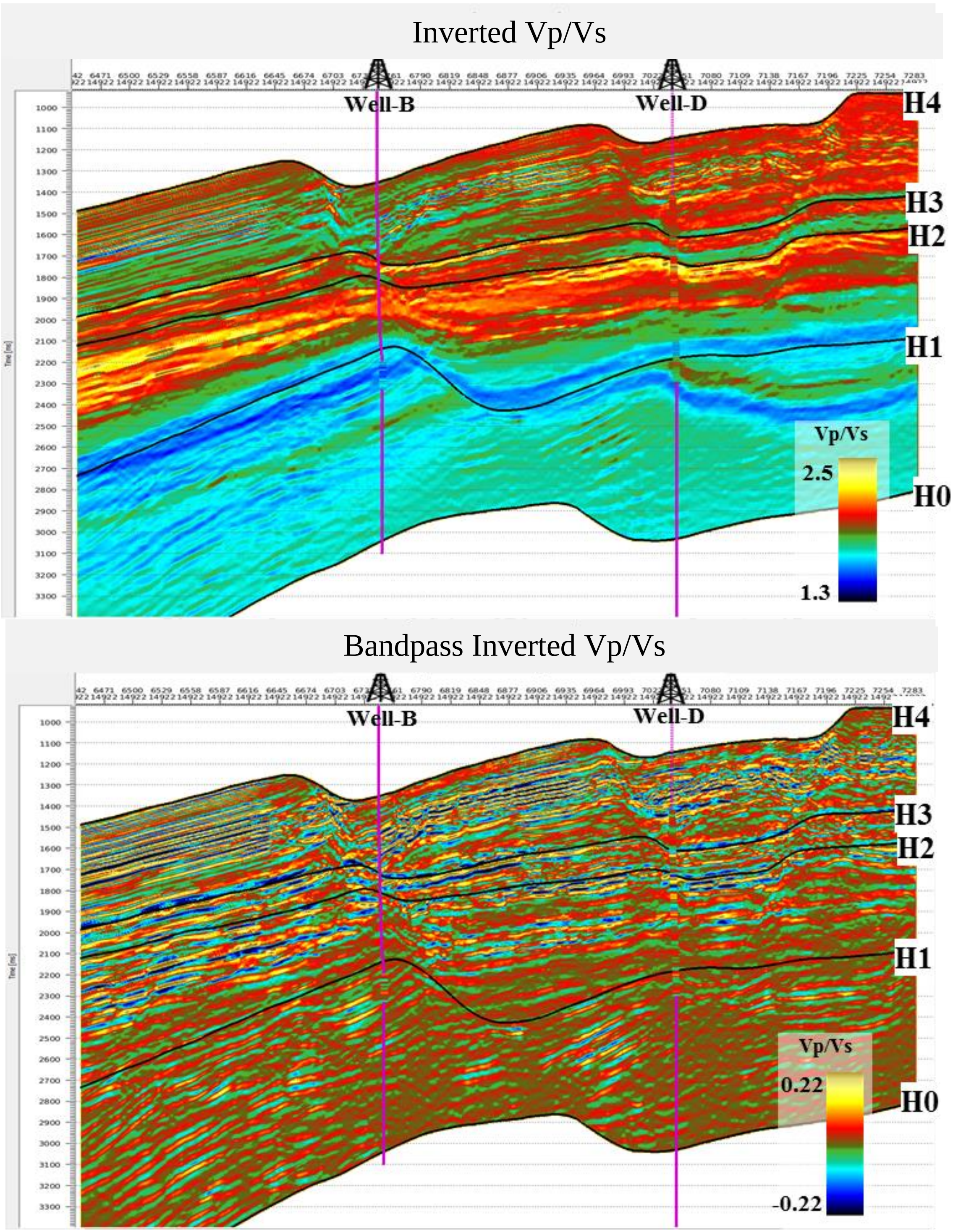

Figure C-39 Crossline 14922 section of final absolute Vp/Vs comparing with Vp/Vs logs at Wells-B and -D (top). Bandpass filtering were applied to both inverted Vp/Vs and well data to create comparable relative inversion results (bottom).

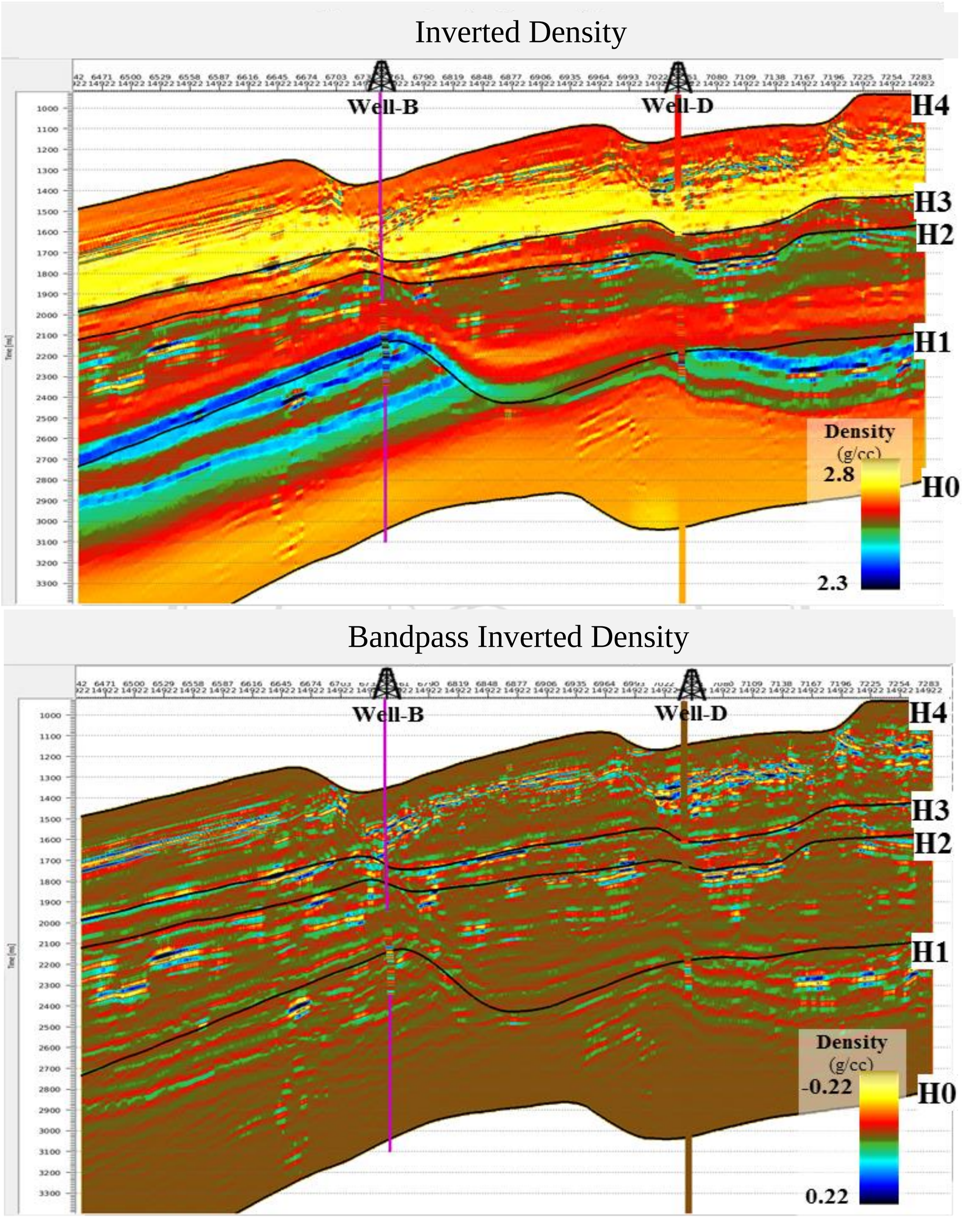

Figure C-40 Crossline 14922 of final absolute density comparing with density logs at Wells-B and -D (top). Bandpass filtering were applied to both inverted density and well data to create comparable relative inversion results (bottom).

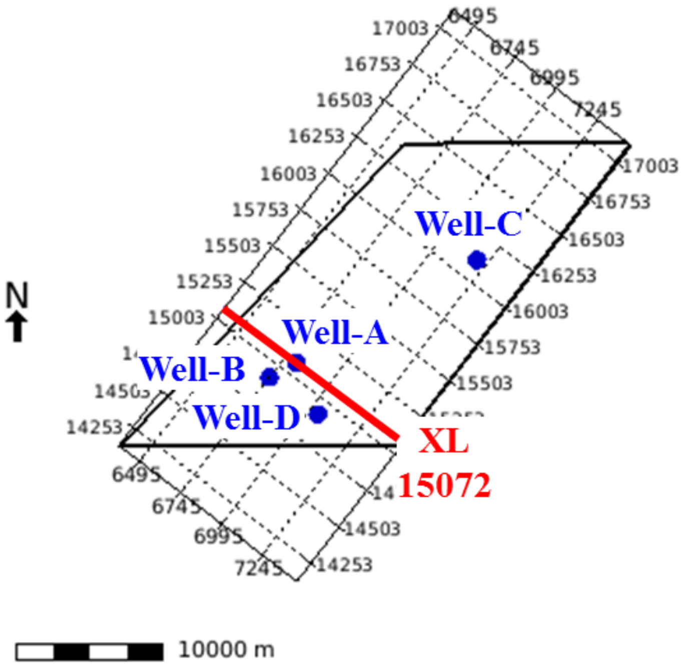

Figure C-41 Map location of crossline 15072 that passed through Well-A location.

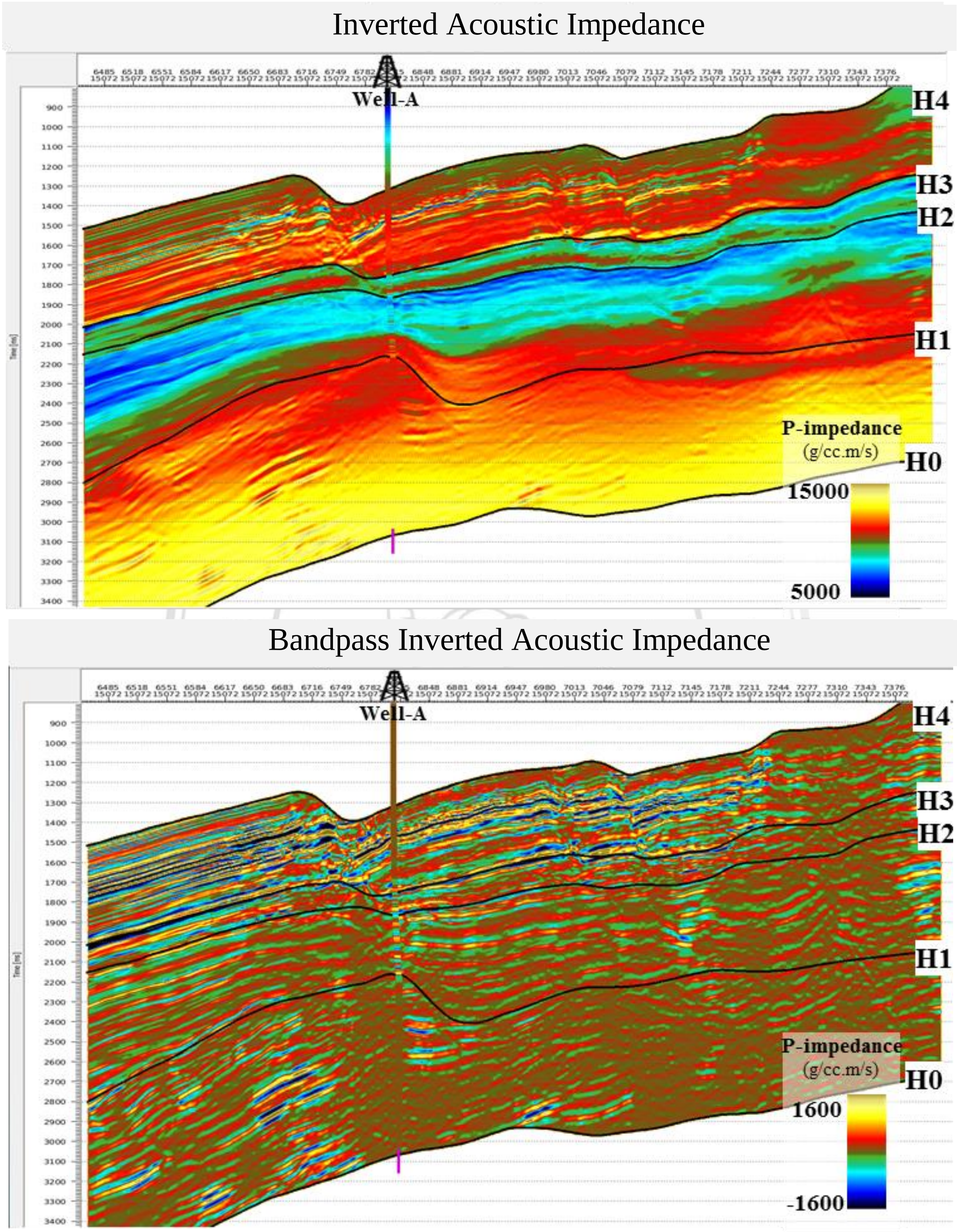

Figure C-42 Crossline 15072 section of final absolute acoustic impedance comparing with acoustic impedance logs at Well-A (top). Bandpass filtering were applied to both inverted acoustic impedance and well data to create comparable relative inversion results (bottom).

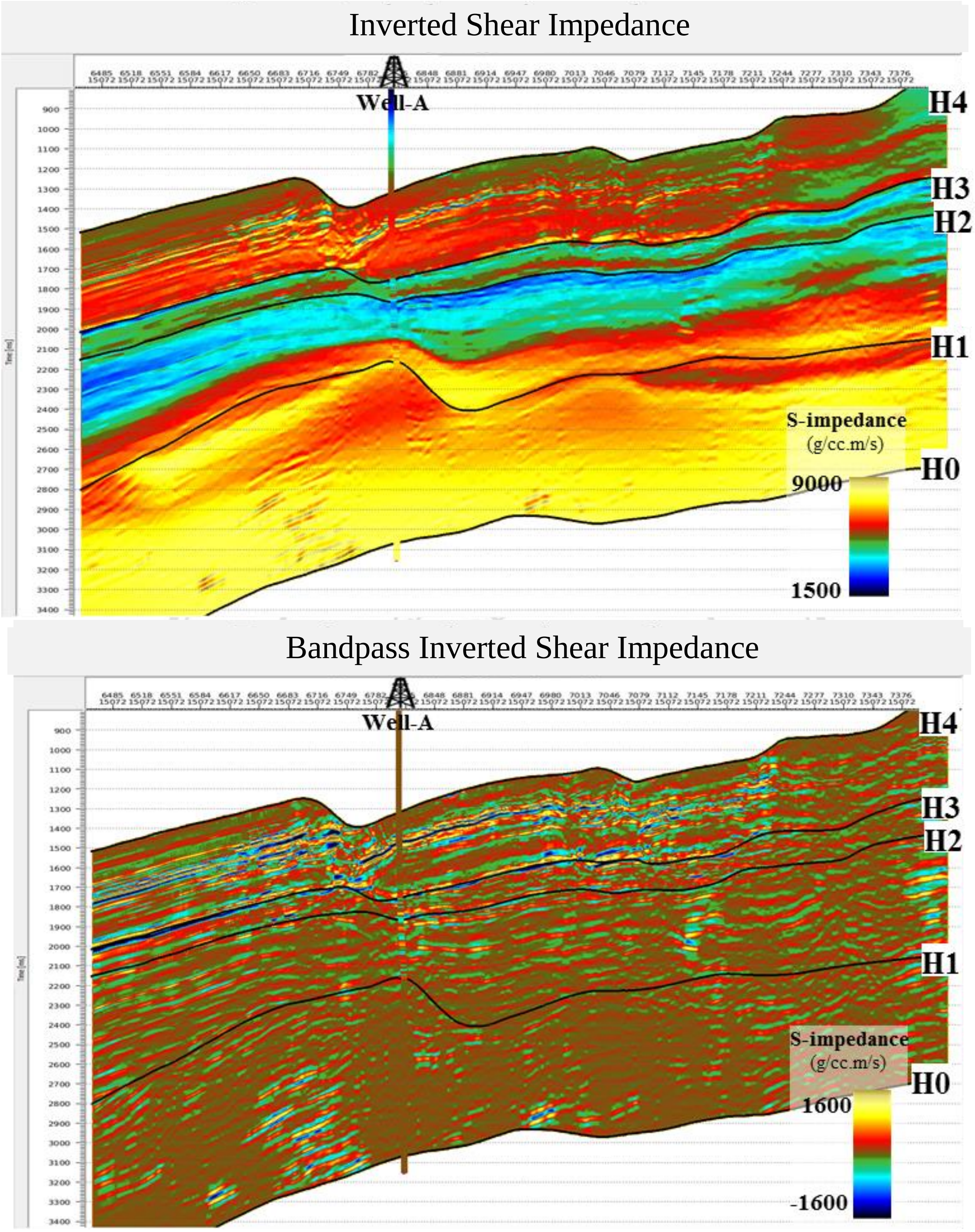

Figure C-43 Crossline 15072 section of final absolute shear impedance comparing with shear impedance logs at Well-A (top). Bandpass filtering were applied to both inverted shear impedance and well data to create comparable relative inversion results (bottom).

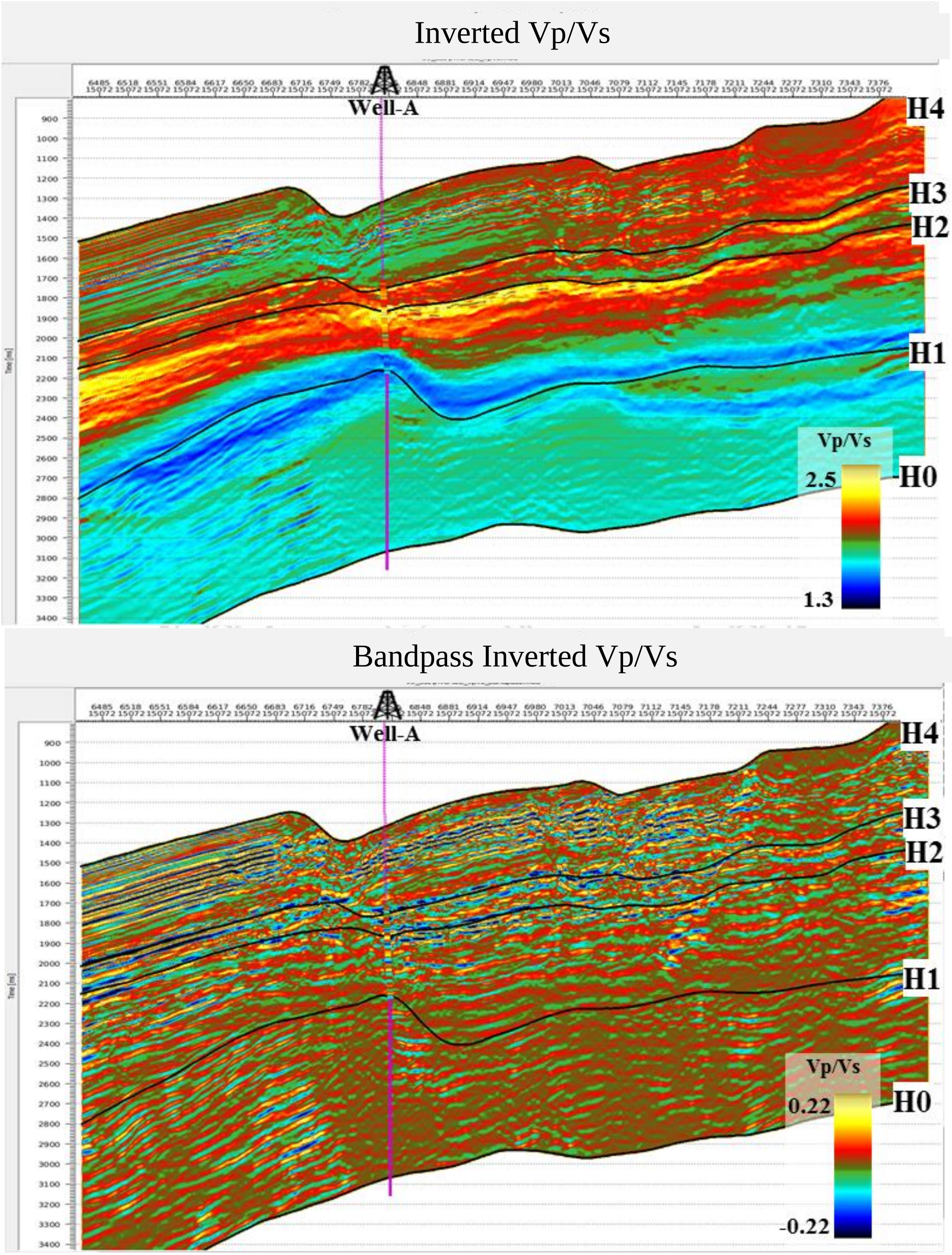

Figure C-44 Crossline 15072 section of final absolute Vp/Vs comparing with Vp/Vs logs at Well-A (top). Bandpass filtering were applied to both inverted Vp/Vs and well data to create comparable relative inversion results (bottom).

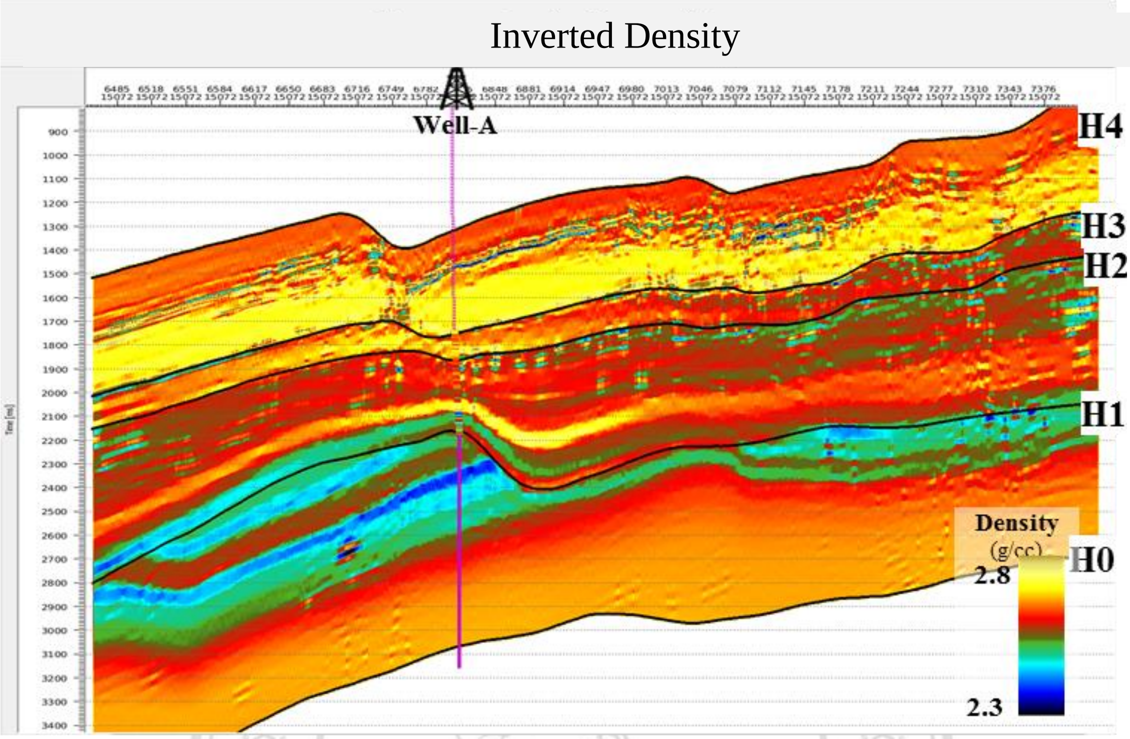

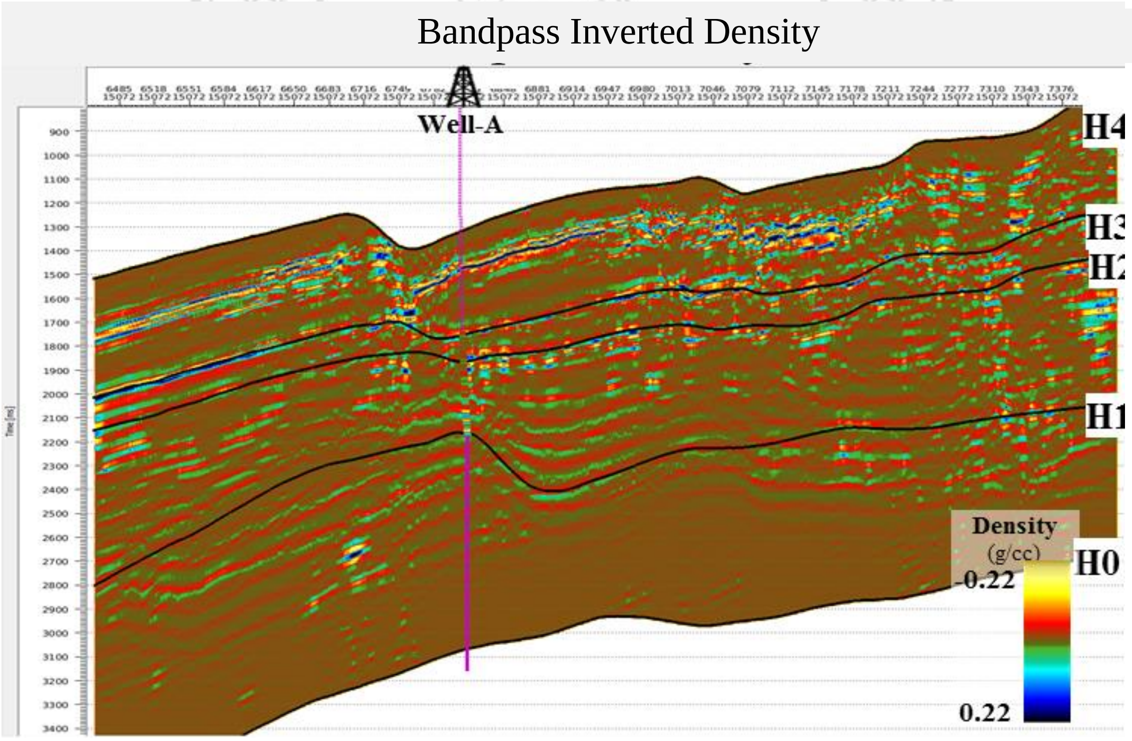

Figure C-45 Crossline 15072 section of final absolute density comparing with density logs at Well-A (top). Bandpass filtering were applied to both inverted density and well data to create comparable relative inversion results (bottom).

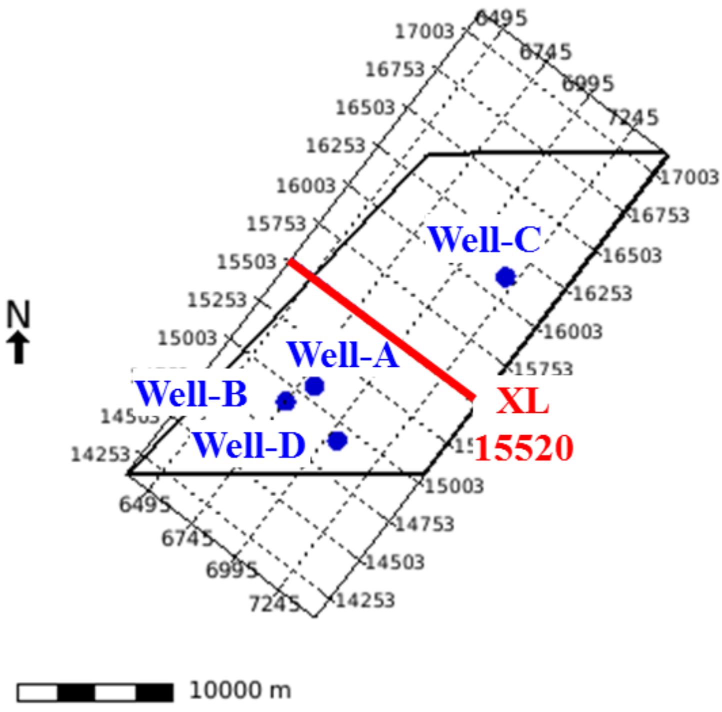

Figure C-46 Map location of crossline 15520.

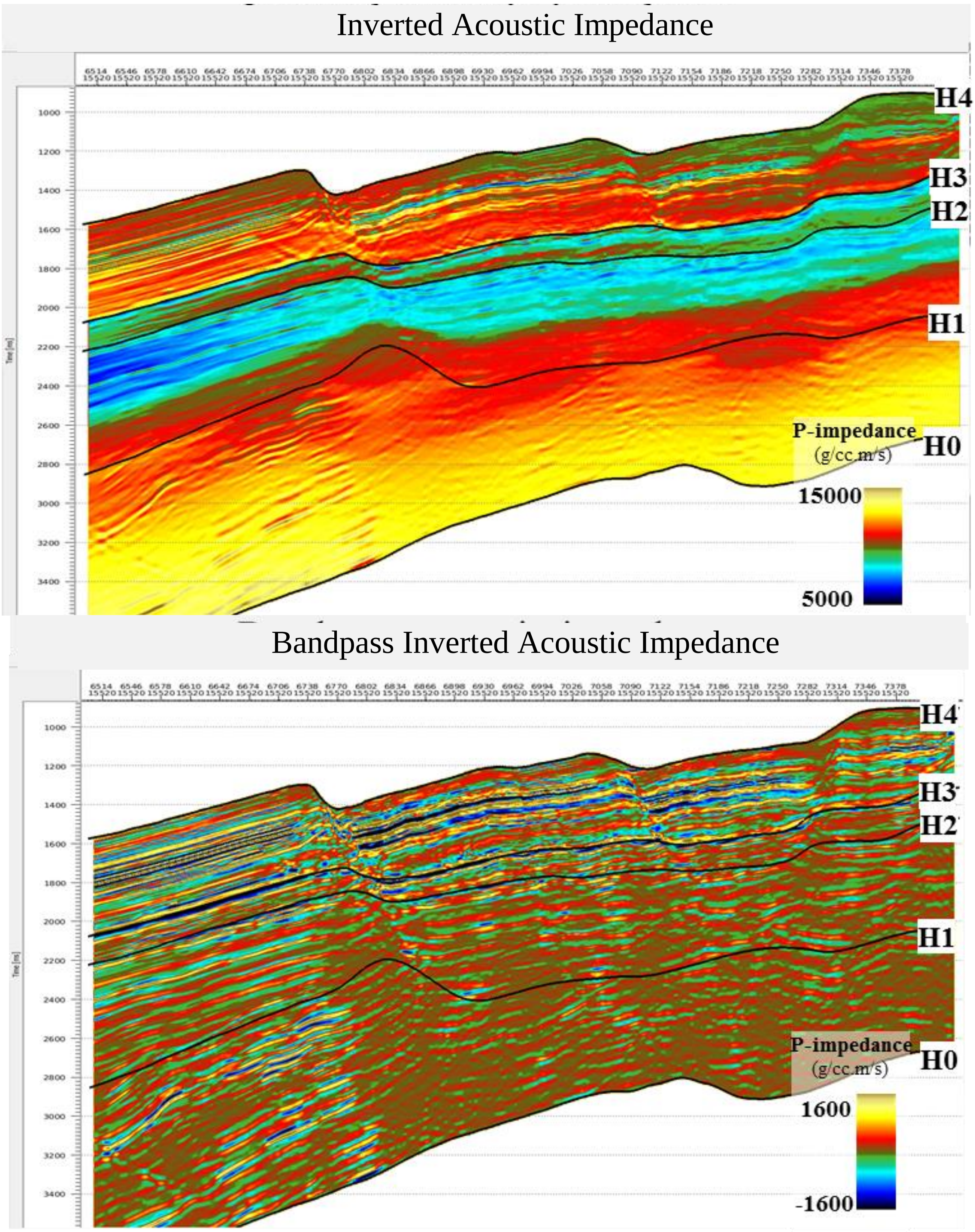

Figure C-47 Crossline 15520 section of final absolute acoustic impedance (top) and bandpass filtering were applied to inverted acoustic impedance to create comparable relative inversion results (bottom).

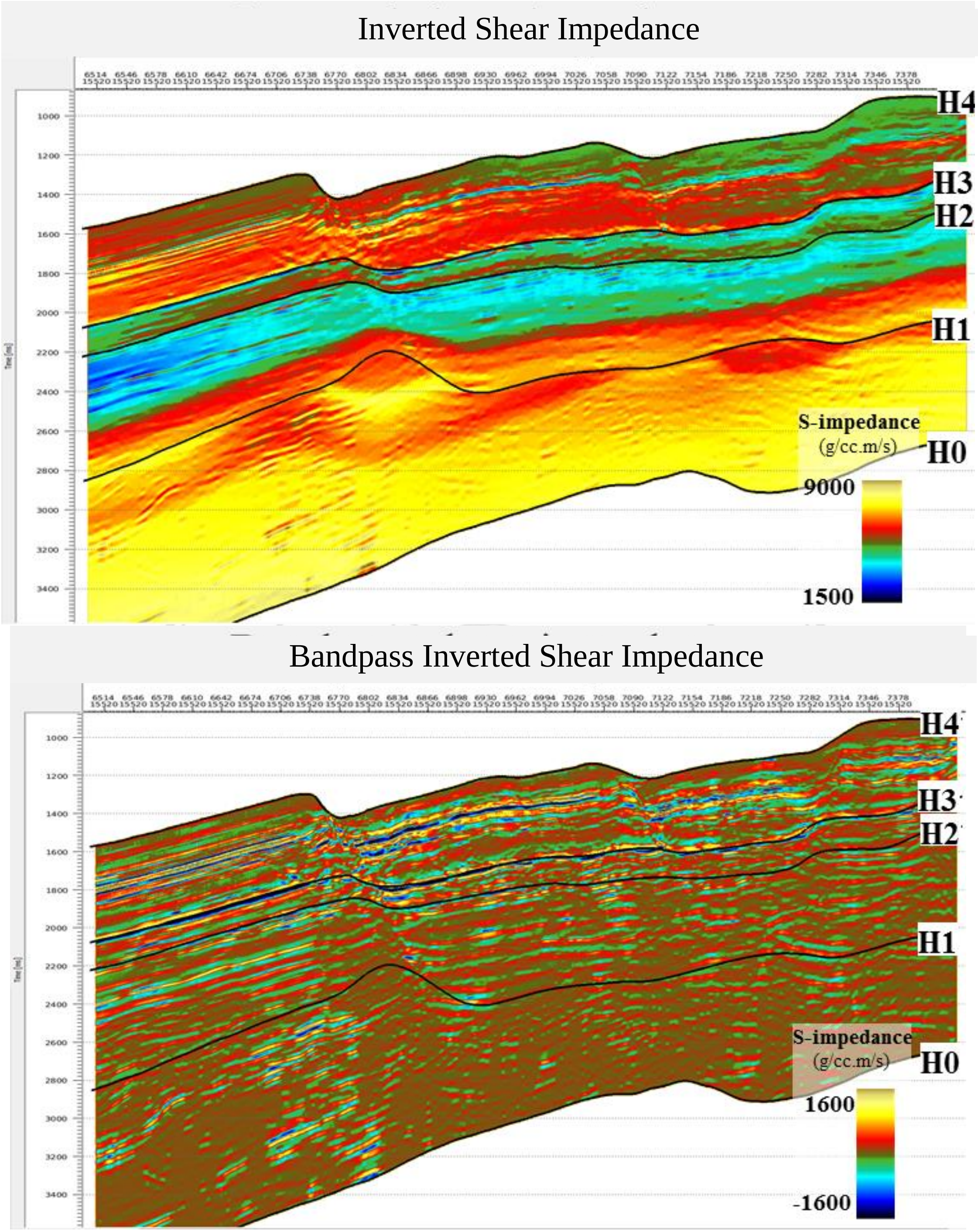

Figure C-48 Crossline 15520 section of final absolute shear impedance (top) and bandpass filtering were applied to inverted shear impedance to create comparable relative inversion results (bottom).

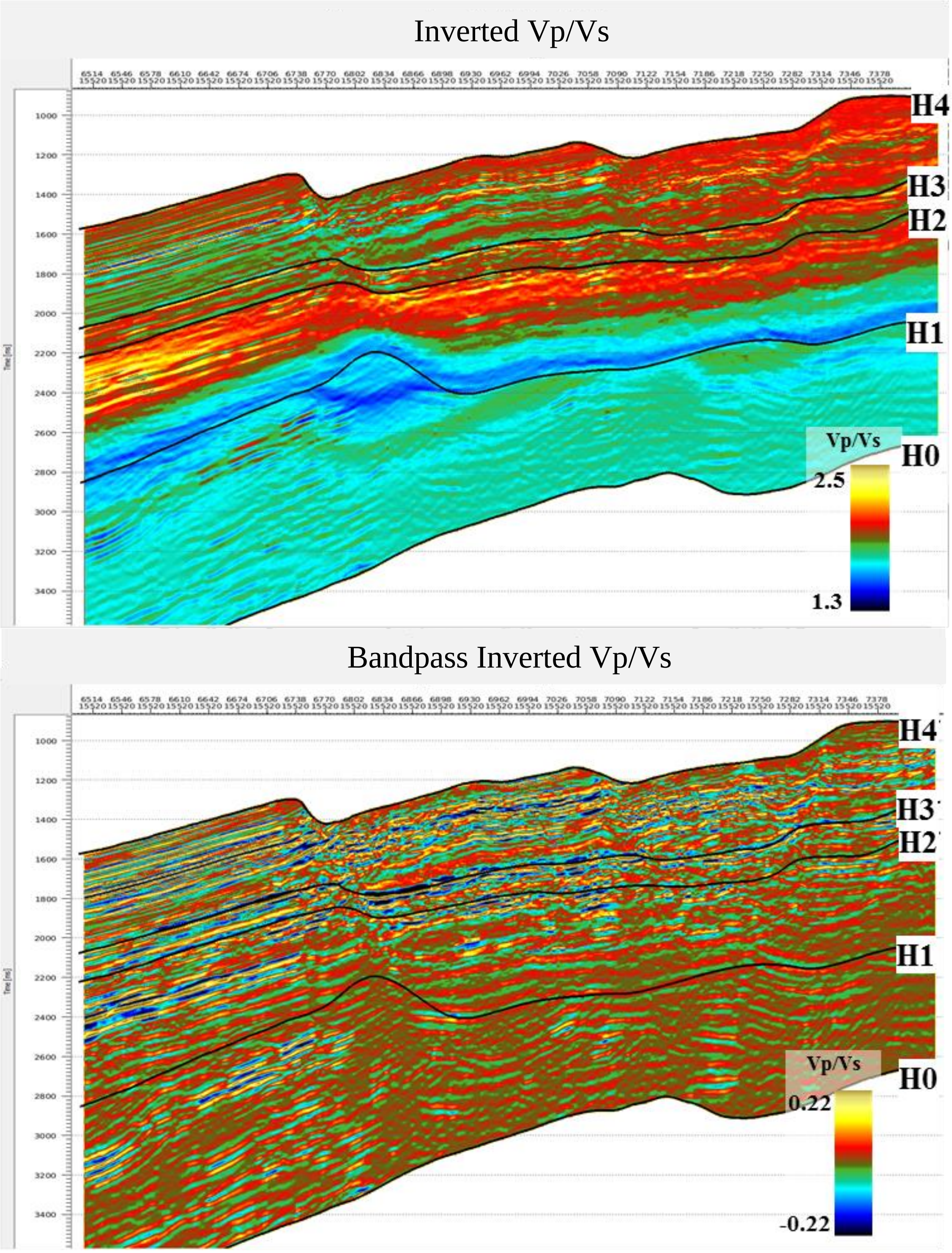

Figure C-49 Crossline 15520 section of final absolute Vp/Vs (top) and bandpass filtering were applied to inverted Vp/Vs to create comparable relative inversion results (bottom).

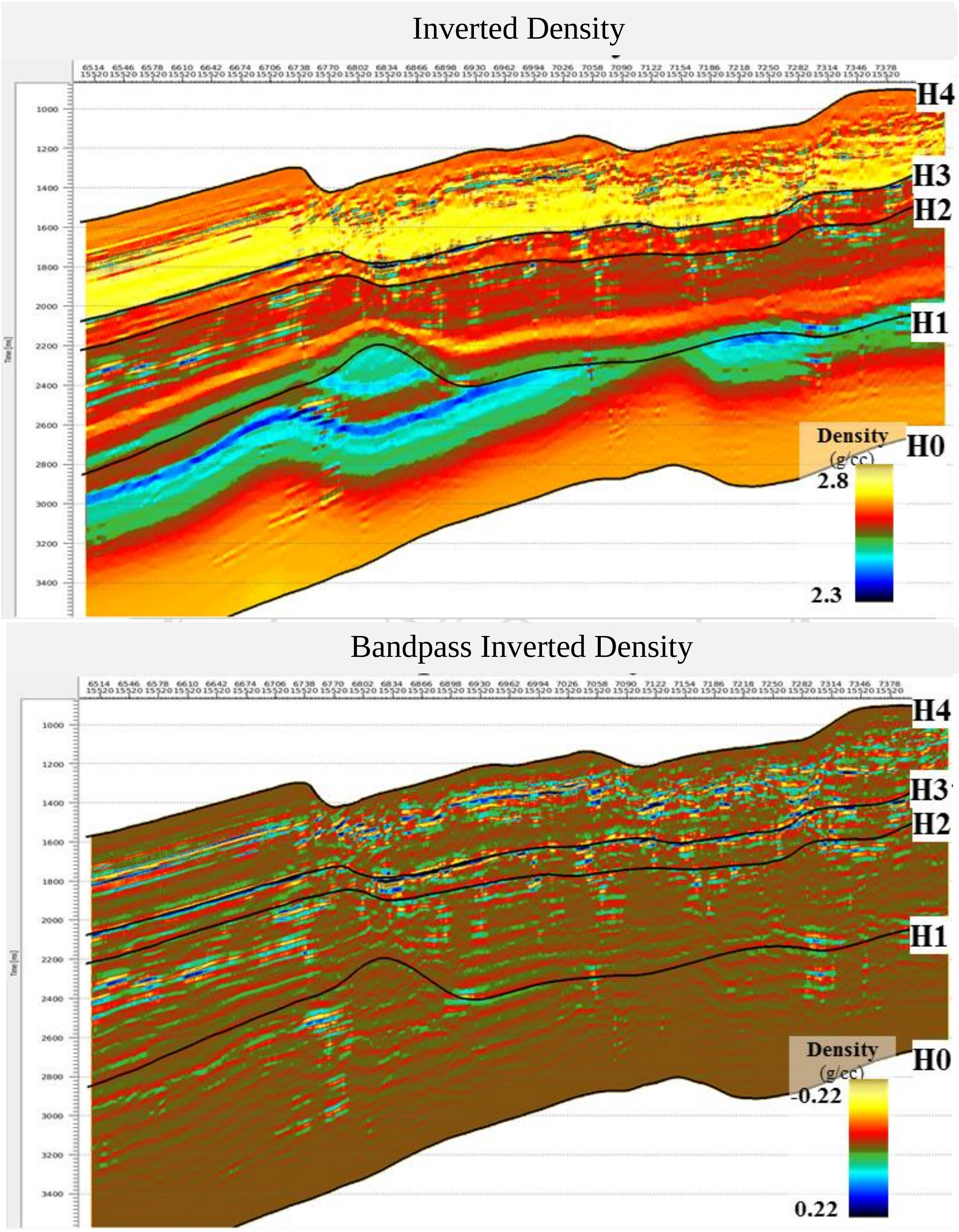

Figure C-50 Crossline 15520 section of final absolute density (top) and bandpass filtering were applied to inverted density to create comparable relative inversion results (bottom).

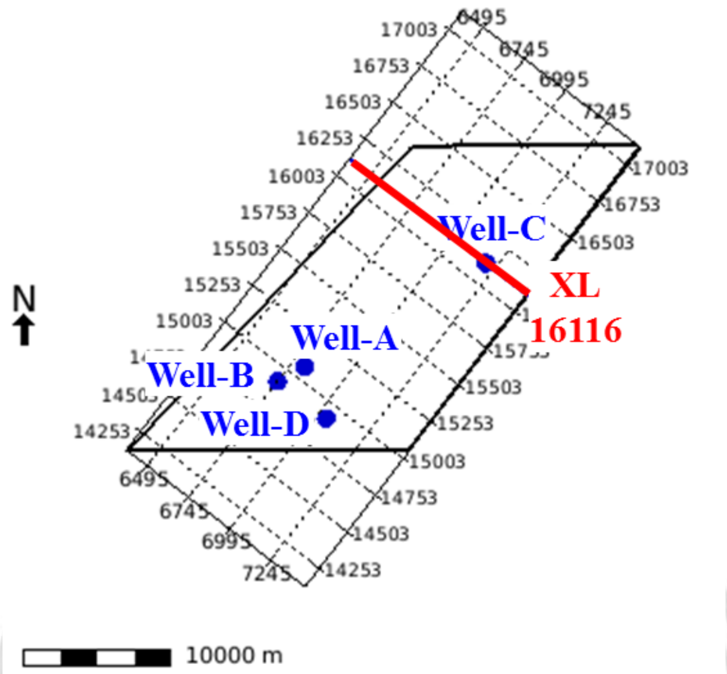

Figure C-51 Map location of crossline 16116 that passed through Well-C location.

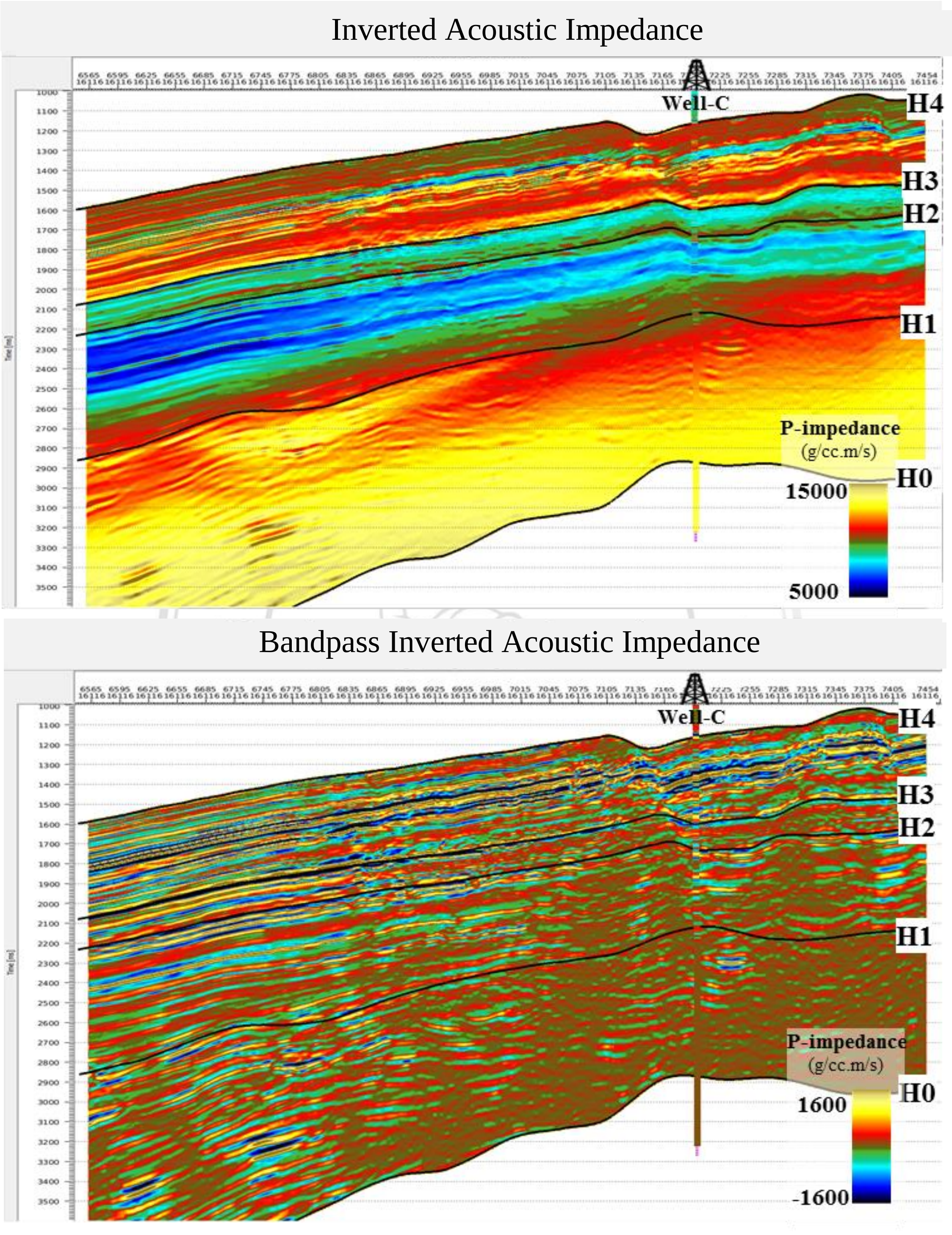

Figure C-52 Crossline 16116 section of final absolute acoustic impedance comparing with acoustic impedance logs at Well-C (top). Bandpass filtering were applied to both inverted acoustic impedance and well data to create comparable relative inversion results (bottom).

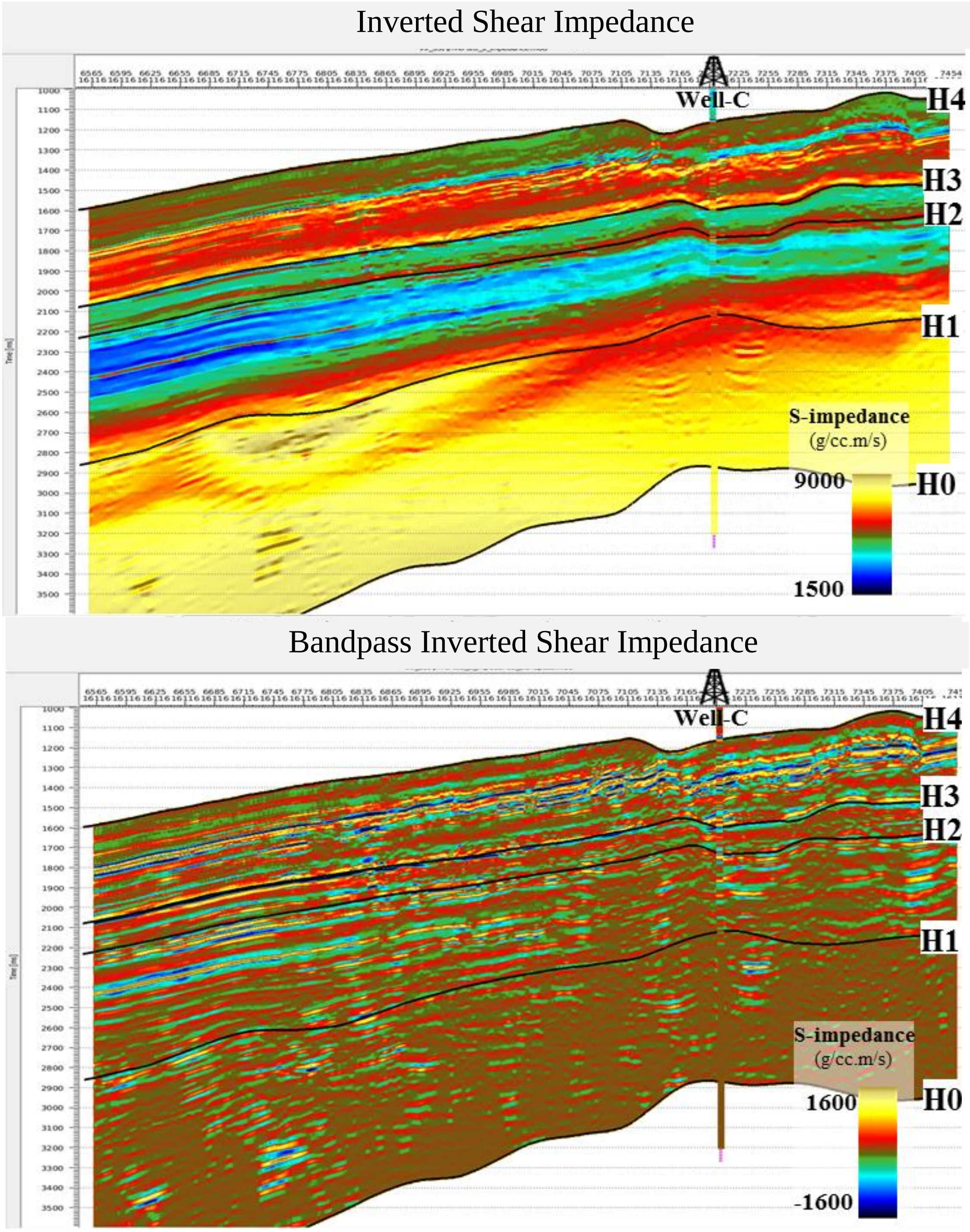

Figure C-53 Crossline 16116 section of final absolute shear impedance comparing with shear impedance logs at Well-C (top). Bandpass filtering were applied to both inverted shear impedance and well data to create comparable relative inversion results (bottom).

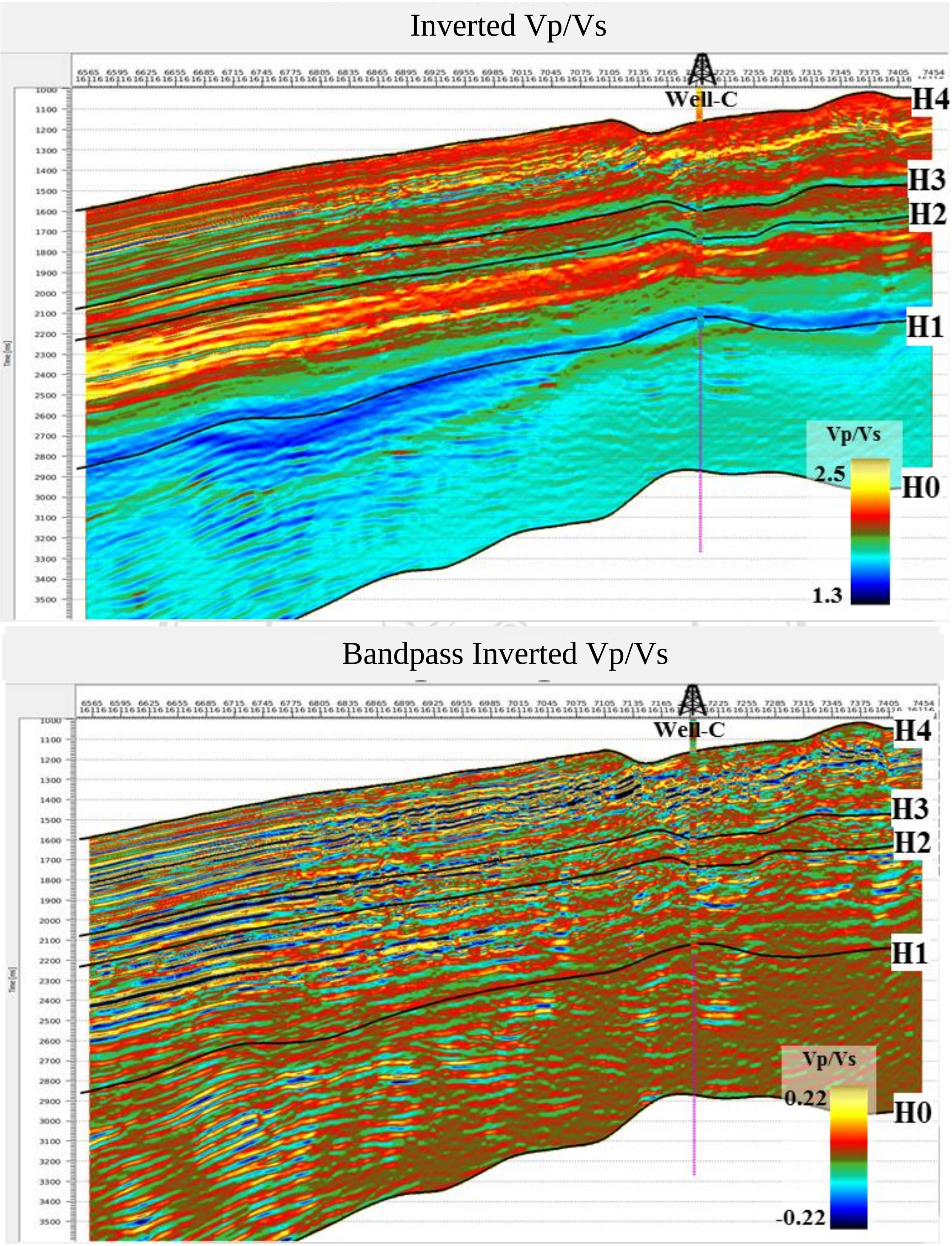

Figure C-54 Crossline 16116 section of final absolute Vp/Vs comparing with Vp/Vs logs at Well-C (top). Bandpass filtering were applied to both inverted Vp/Vs and well data to create comparable relative inversion results (bottom).

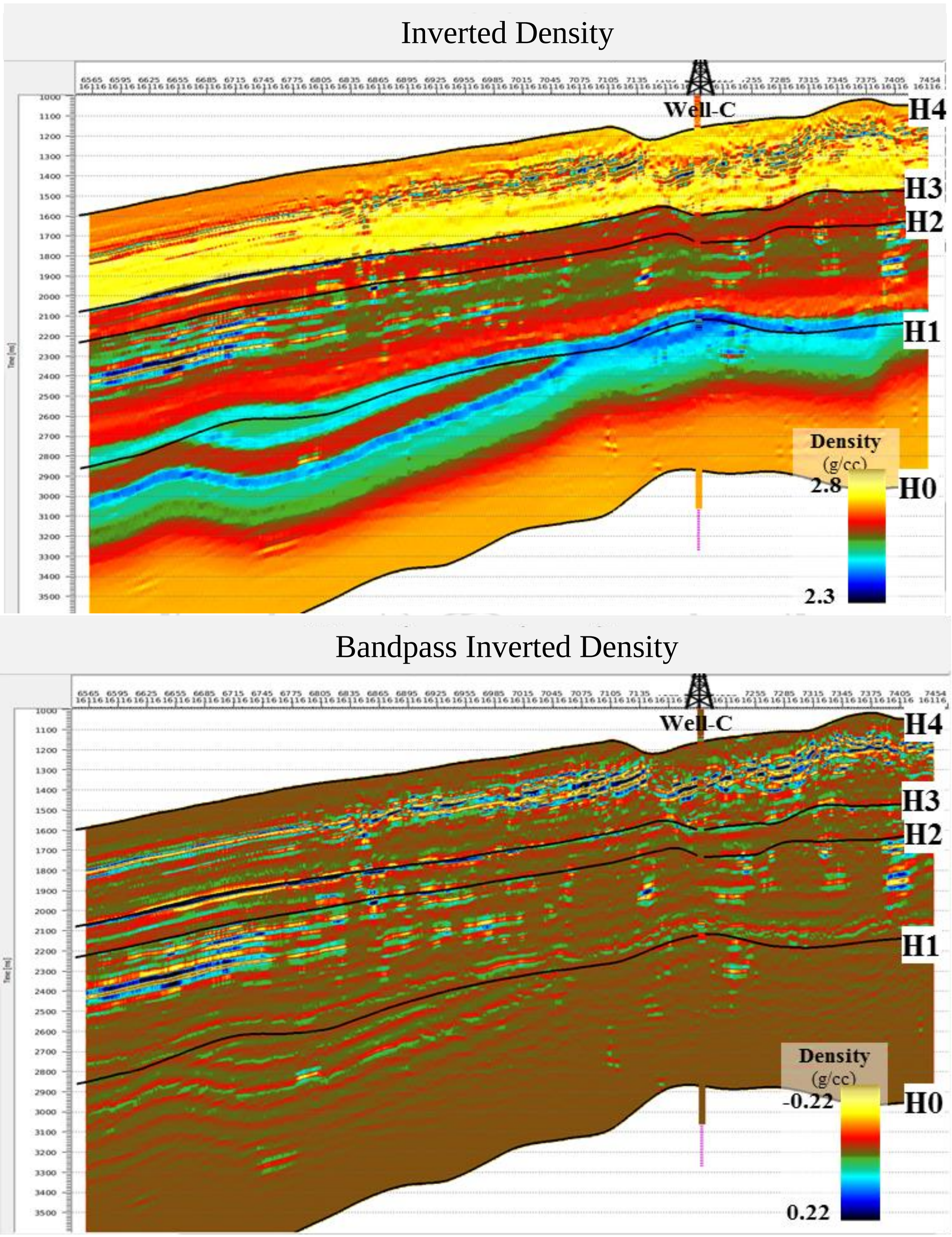

Figure C-55 Crossline 16116 section of final absolute density comparing with density logs at Well-C (top). Bandpass filtering were applied to both inverted density and well data to create comparable relative inversion results (bottom).

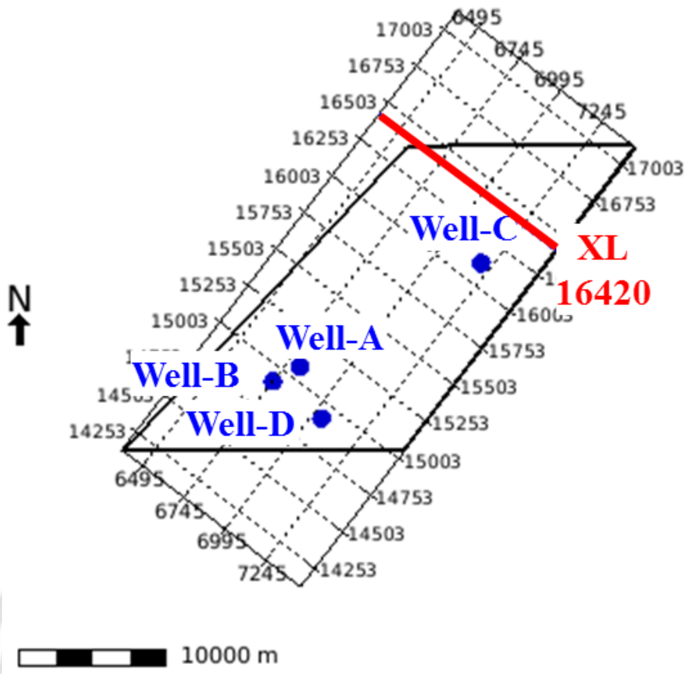

Figure C-56 Map location of crossline 16420.

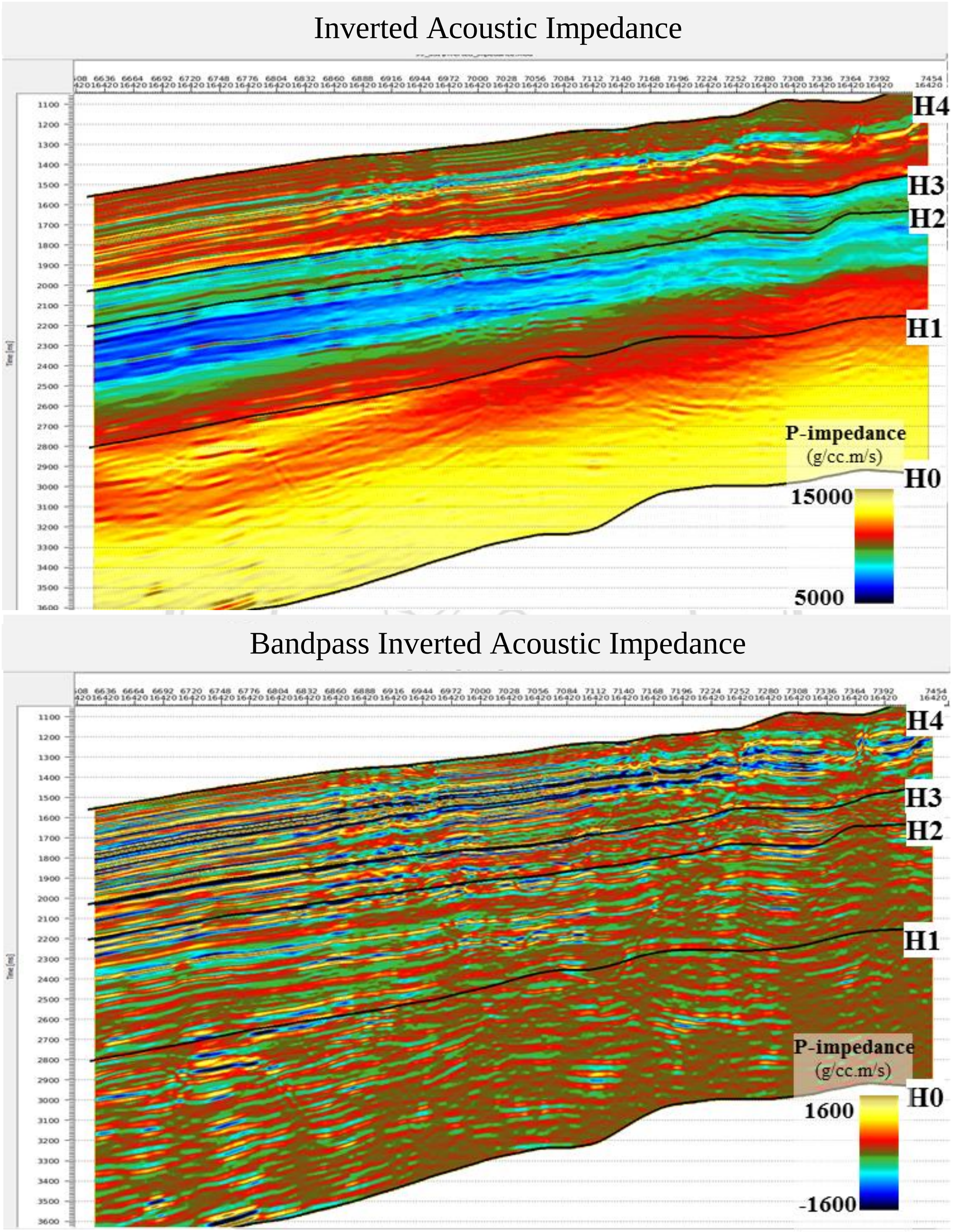

Figure C-57 Crossline 16420 section of final absolute acoustic impedance (top) and bandpass filtering were applied to inverted acoustic impedance to create comparable relative inversion results (bottom).

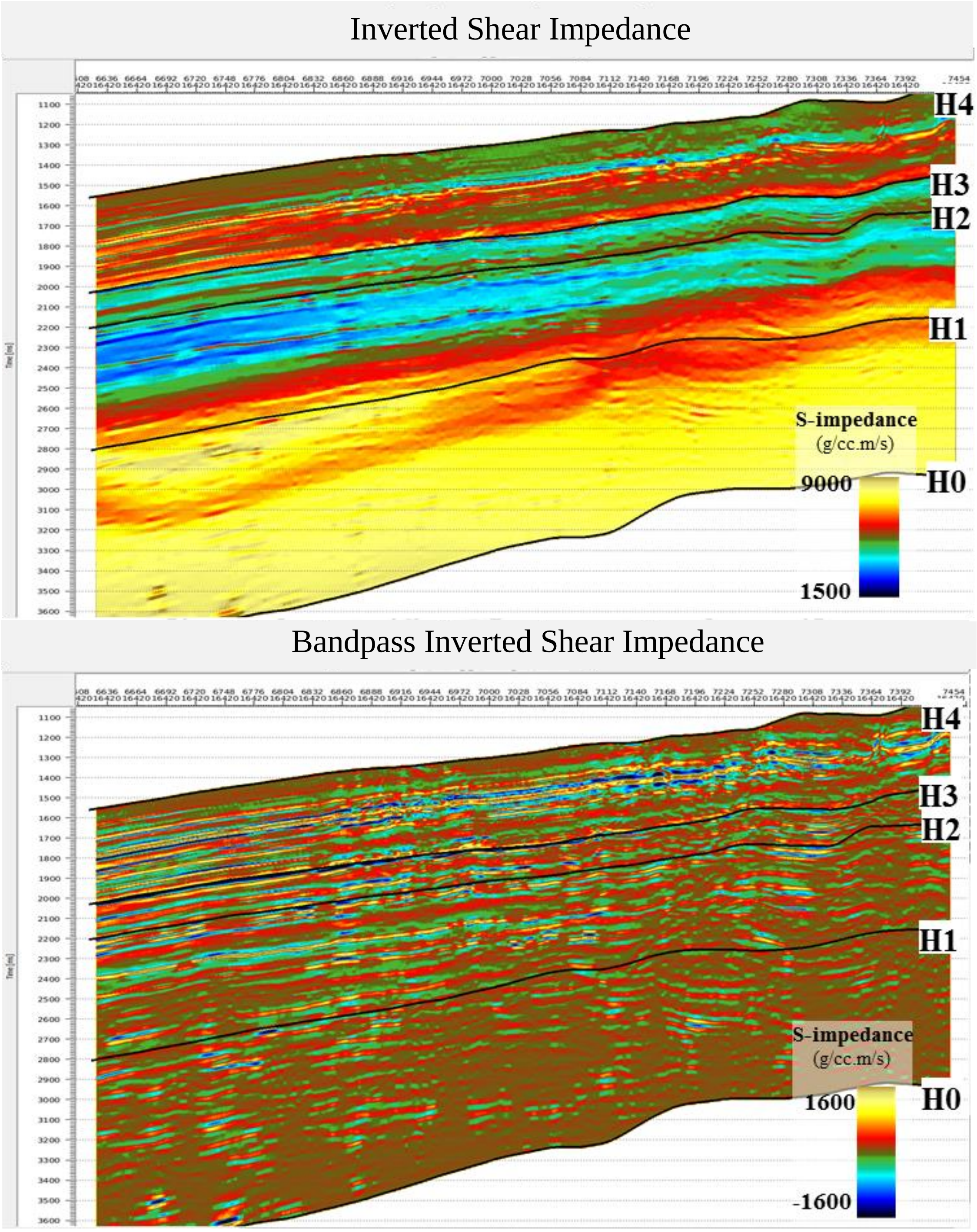

Figure C-58 Crossline 16420 section of final absolute shear impedance (top) and bandpass filtering were applied to inverted shear impedance to create comparable relative inversion results (bottom).

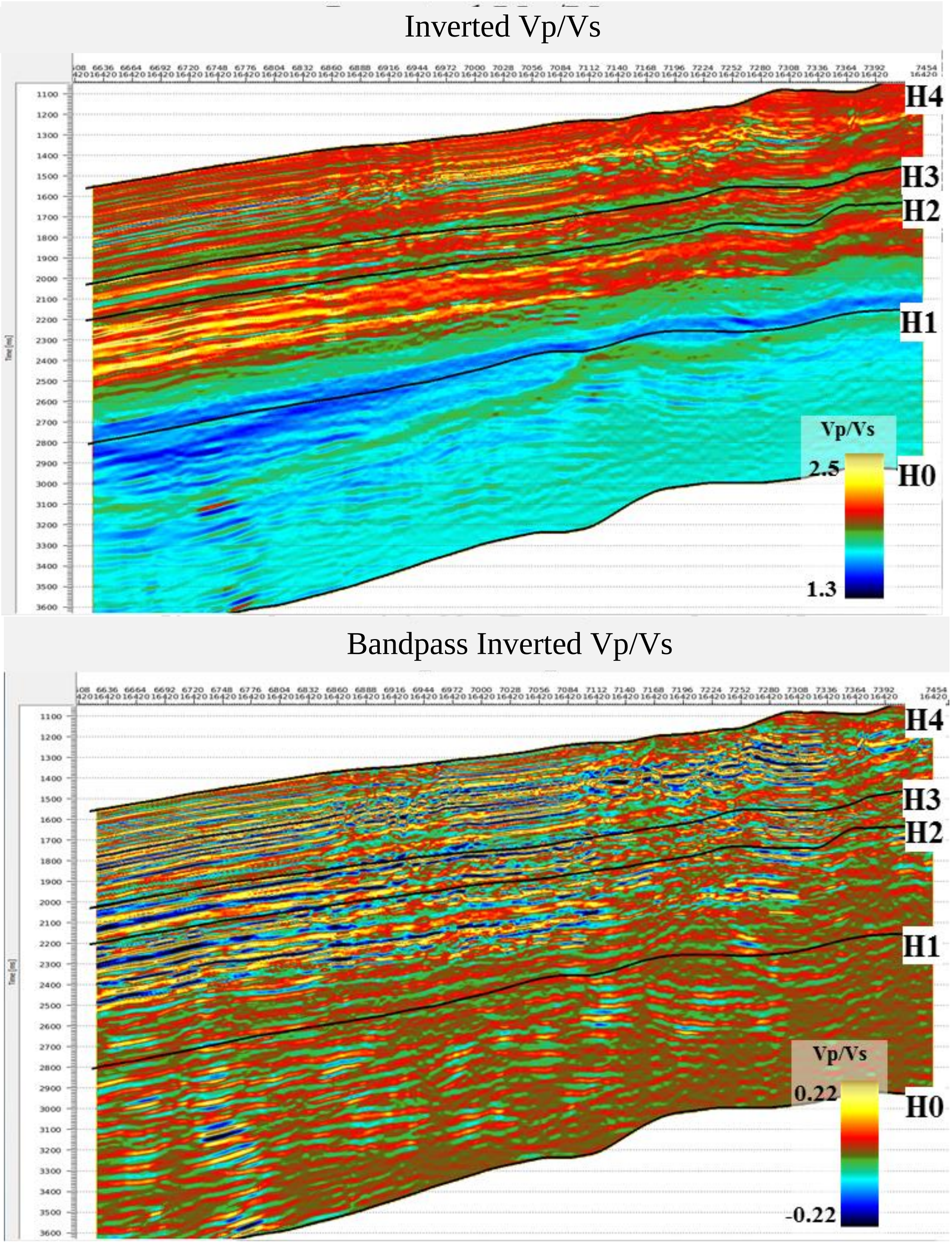

Figure C-59 Crossline 16420 section of final absolute Vp/Vs (top) and bandpass filtering were applied to inverted Vp/Vs to create comparable relative inversion results (bottom).

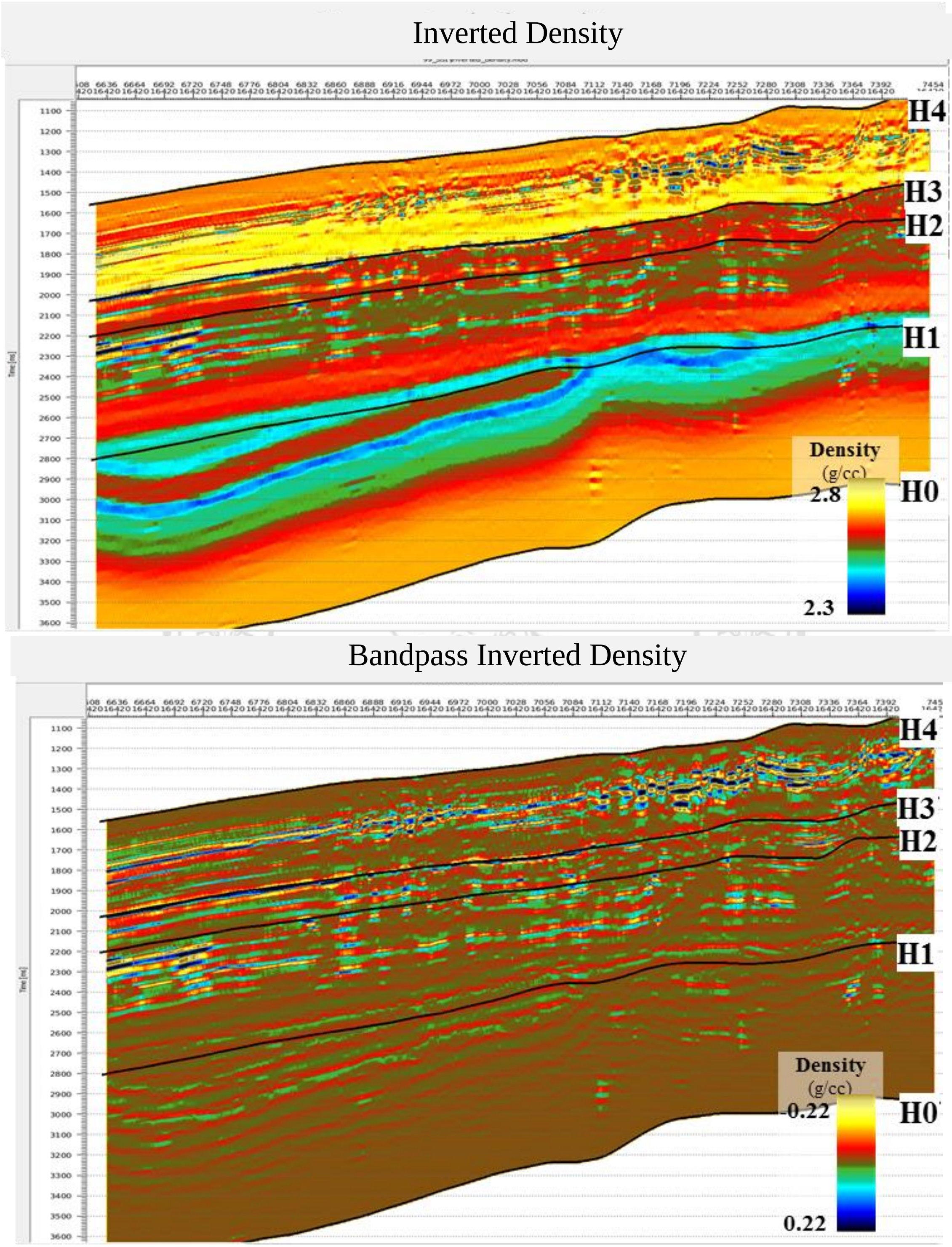

Figure C-60 Crossline 16420 section of final absolute density (top) and bandpass filtering were applied to inverted density to create comparable

APPENDIX D

Lithofacies Classification

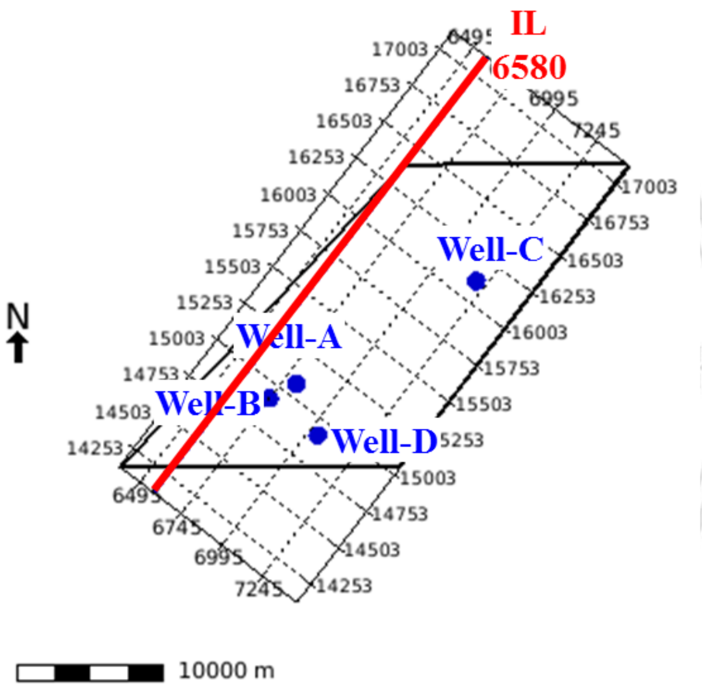

Figure D-1 Map location of inline 6580.

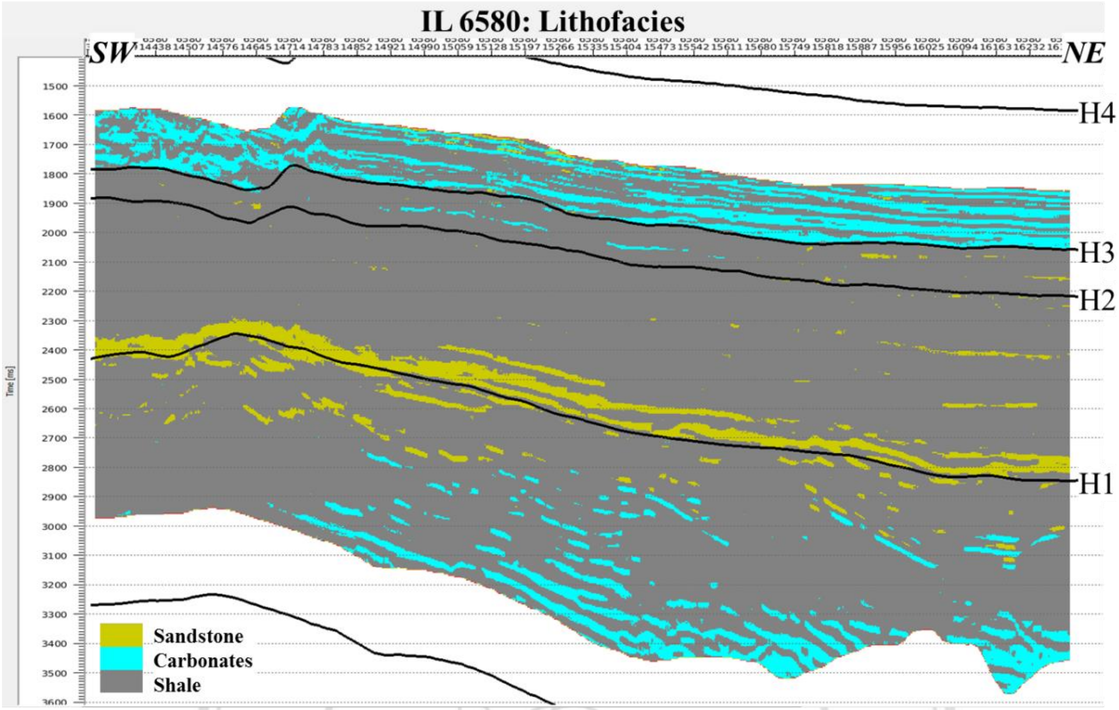

Figure D-2 Inline 6580 section showing lithofacies (most probable).

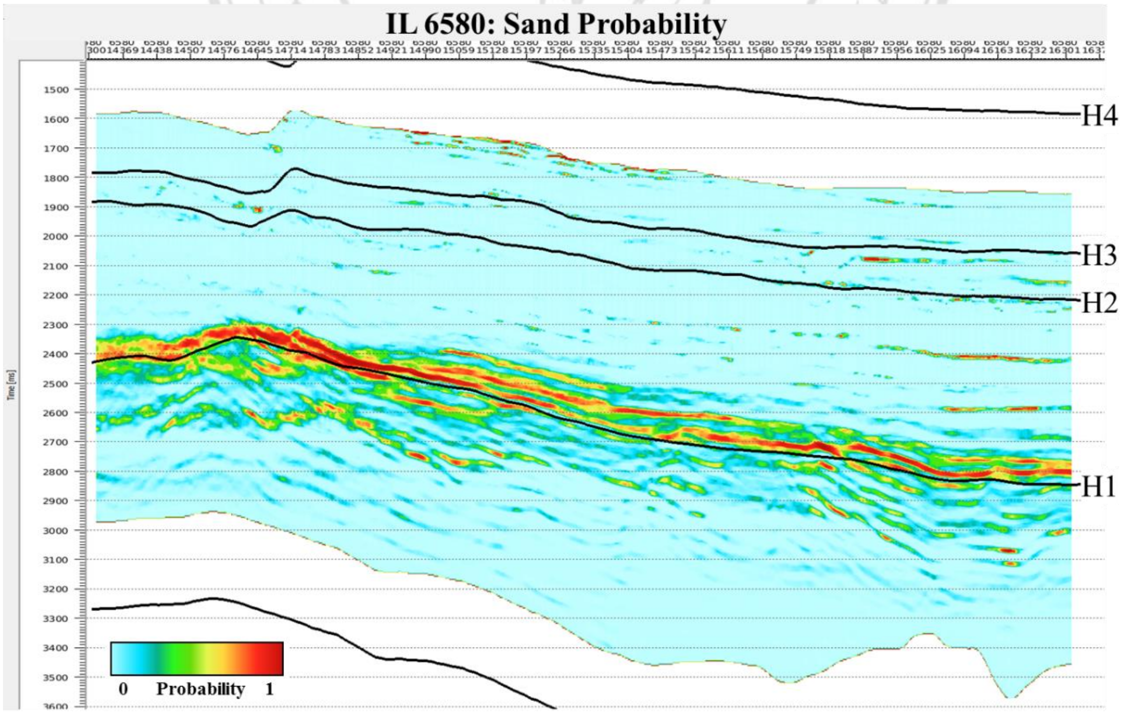

Figure D-3 Inline 6580 section showing the distribution of sand probability.

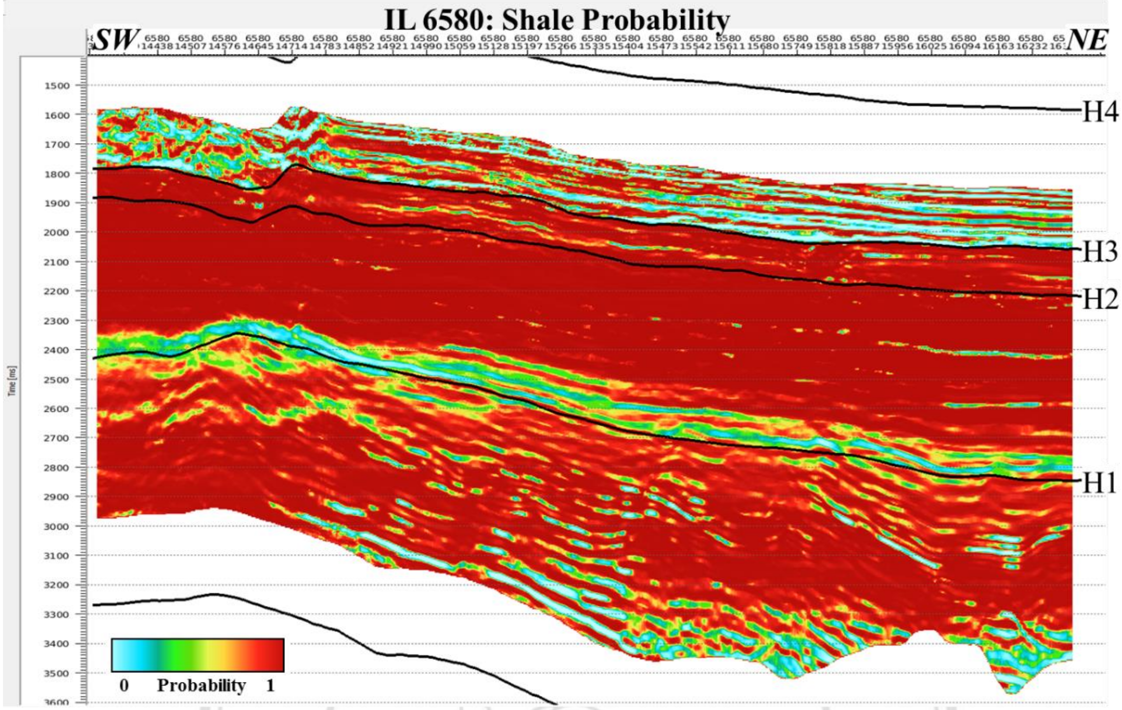

Figure D-4 Inline 6580 section showing the distribution of shale probability.

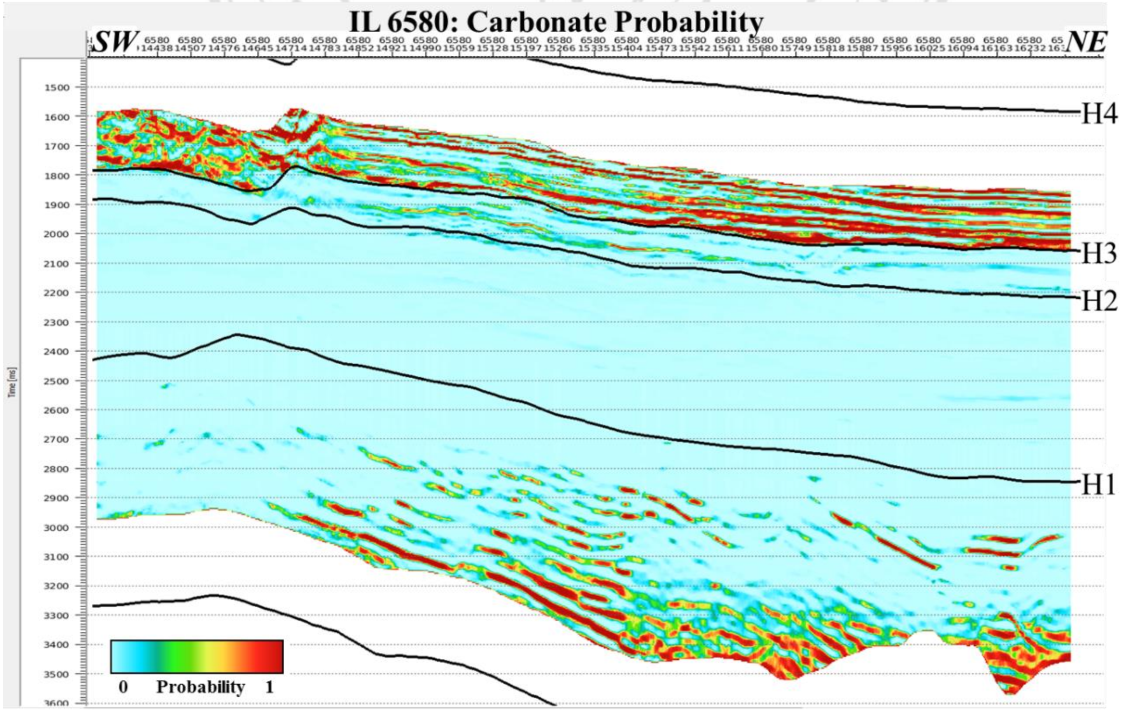

Figure D-5 Inline 6580 section showing the distribution of carbonate probability.

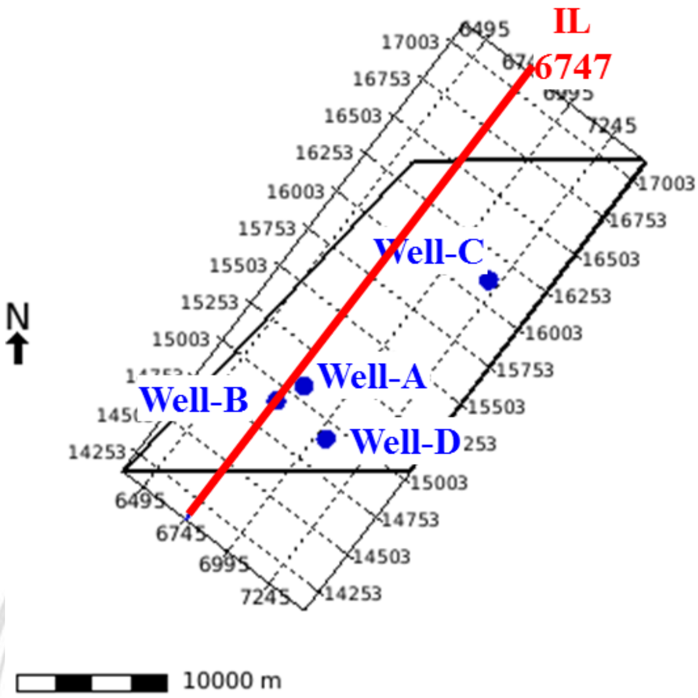

Figure D-6 Map location of inline 6747 that passed through Well-B location.

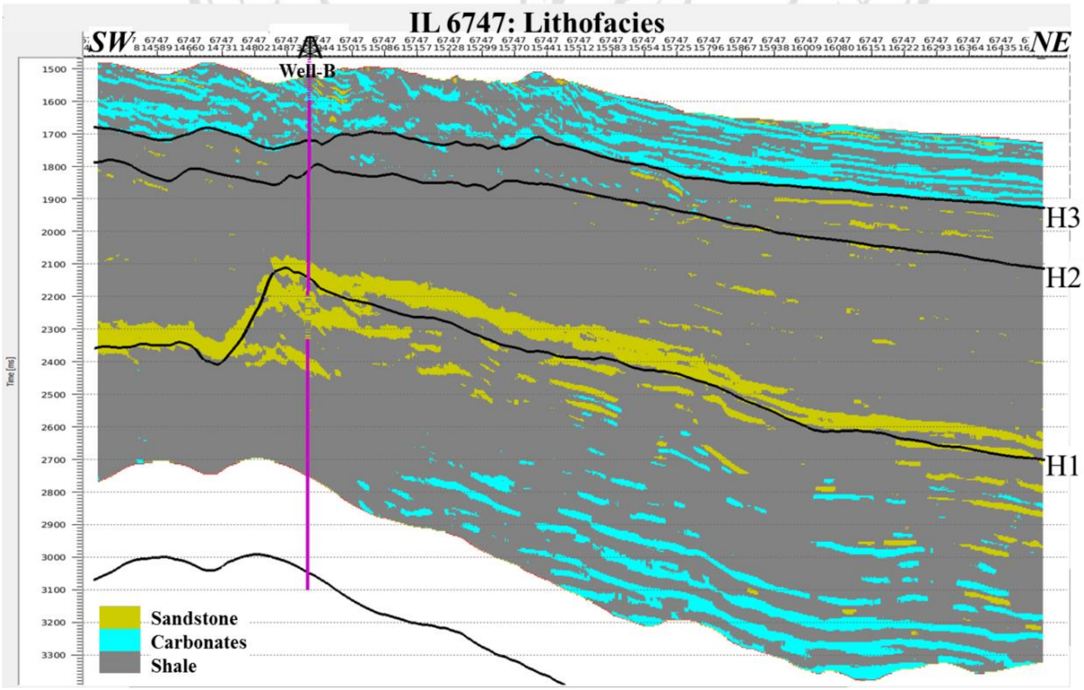

Figure D-7 Inline 6747 section showing lithology log of Well-B was properly captured by the lithofacies cube (most probable).

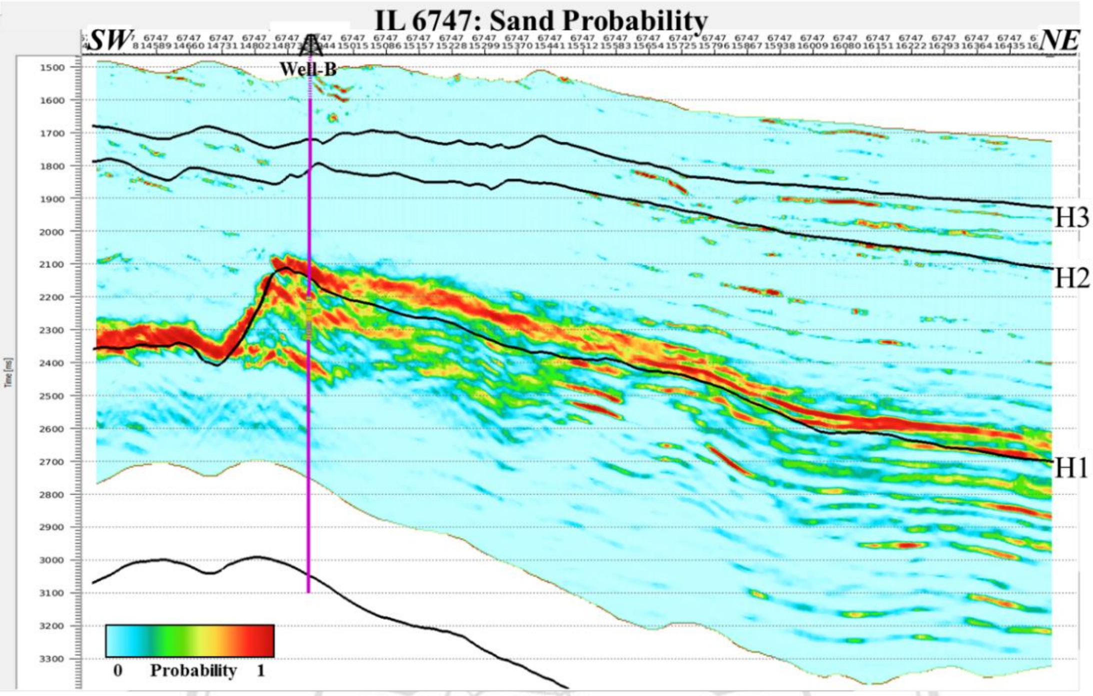

Figure D-8 Inline 6747 section showing the distribution of sand probability.

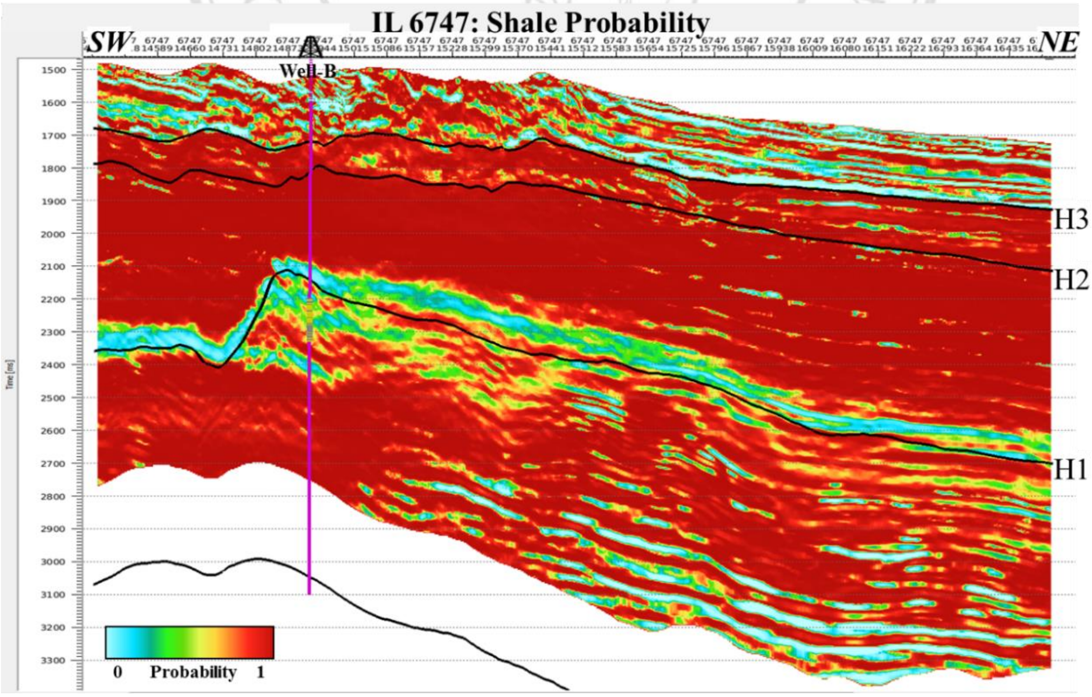

Figure D-9 Inline 6747 section showing the distribution of shale probability.

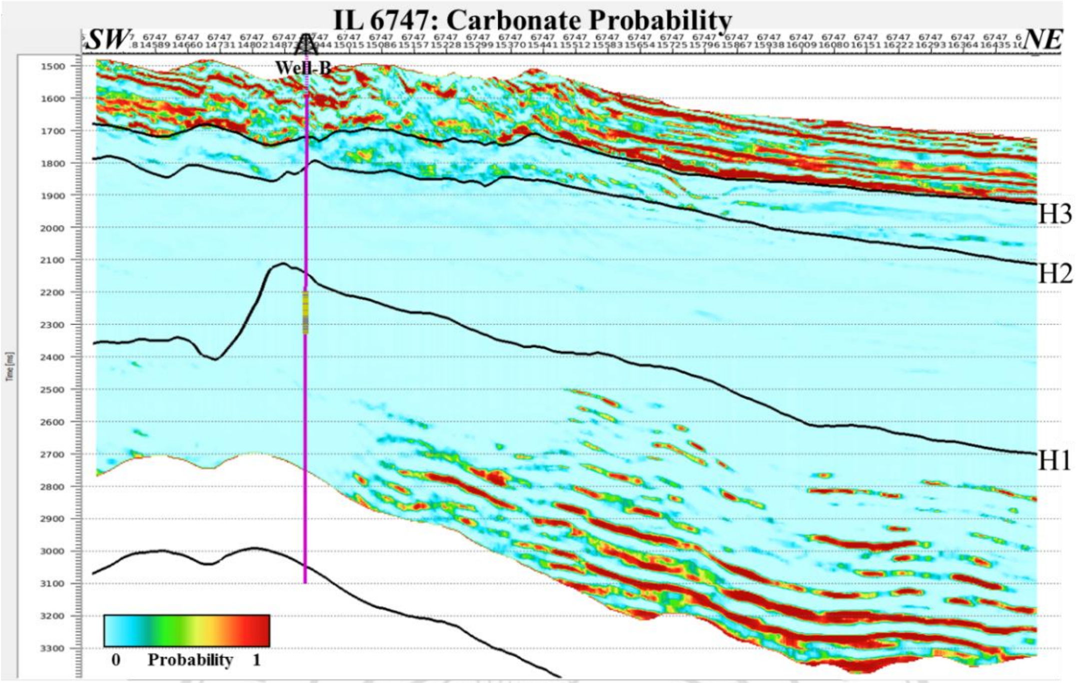

Figure D-10 Inline 6747 section showing the distribution of carbonate probability.

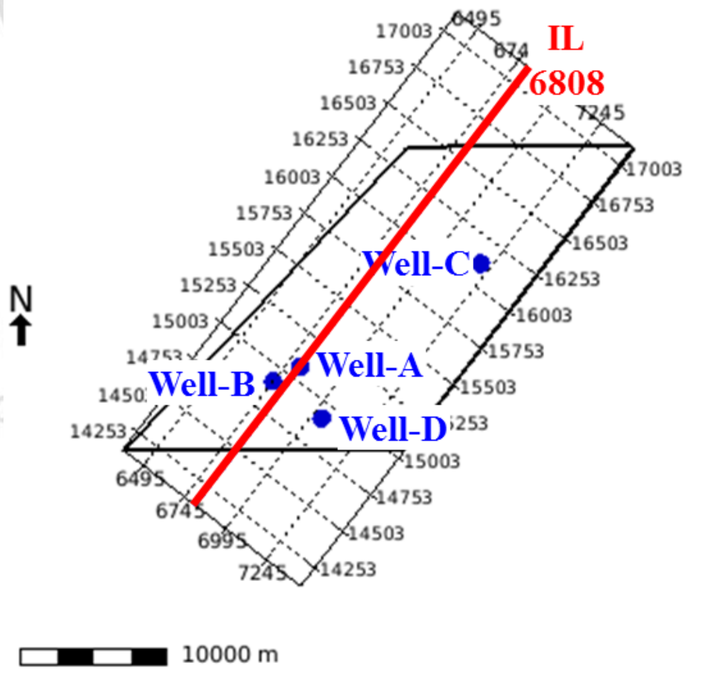

Figure D-11 Map location of inline 6808 that passed through Well-A location.

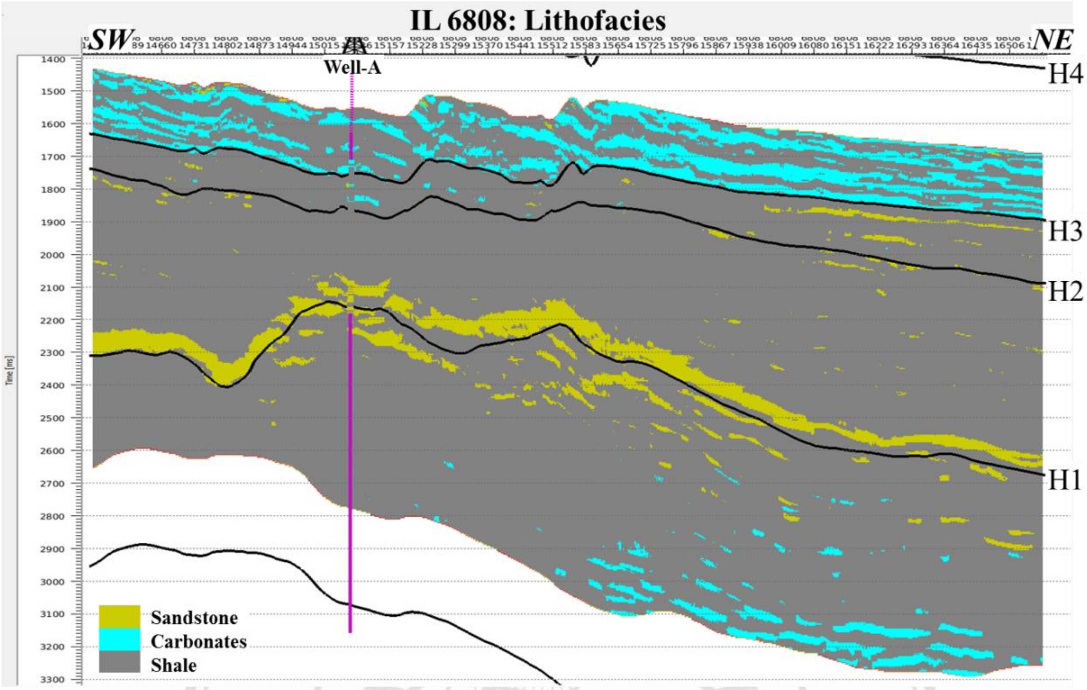

Figure D-12 Inline 6808 section showing lithology log of Well-A was properly captured by the lithofacies cube (most probable).

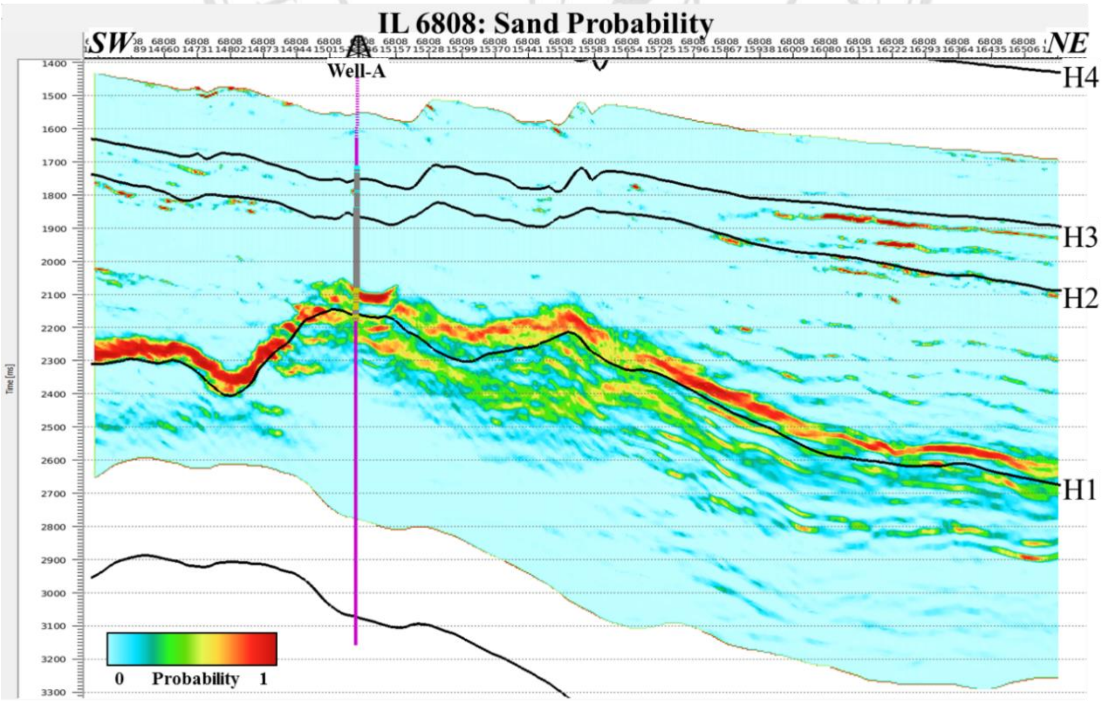

Figure D-13 Inline 6808 section showing the distribution of sand probability.

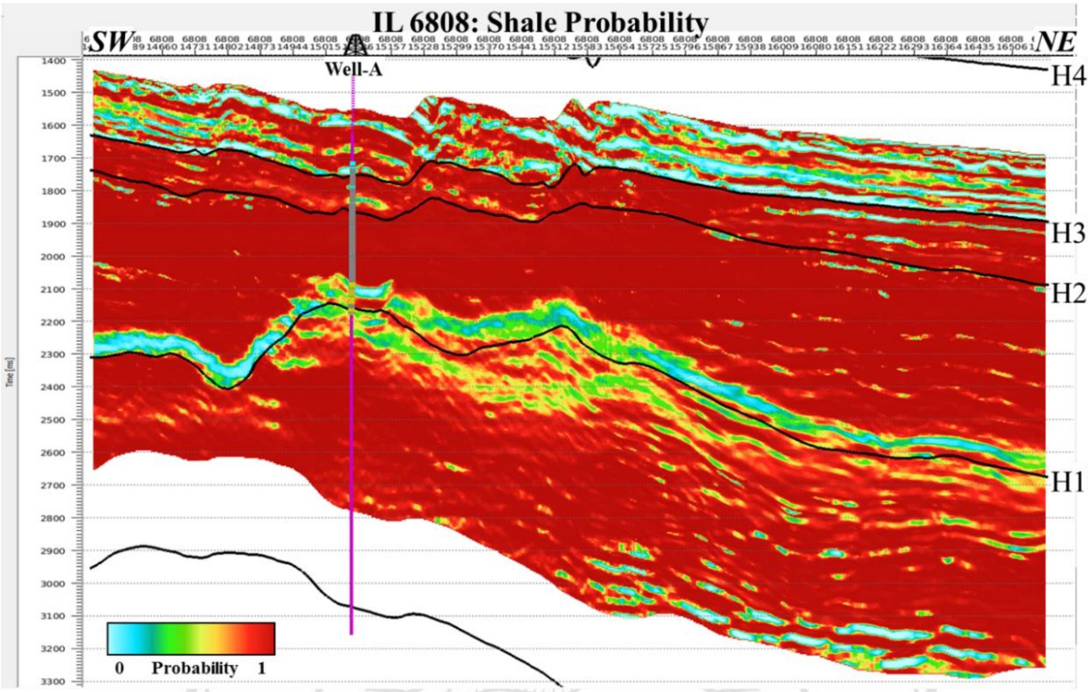

Figure D-14 Inline 6808 section showing the distribution of shale probability.

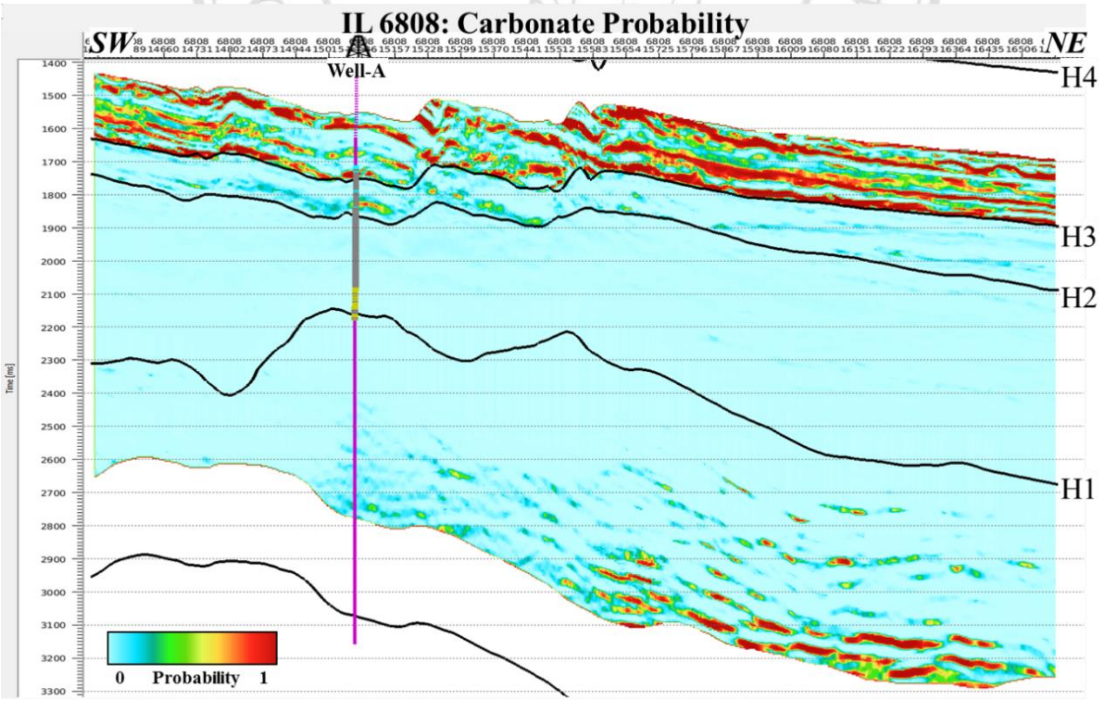

Figure D-15 Inline 6808 section showing the distribution of carbonate probability.

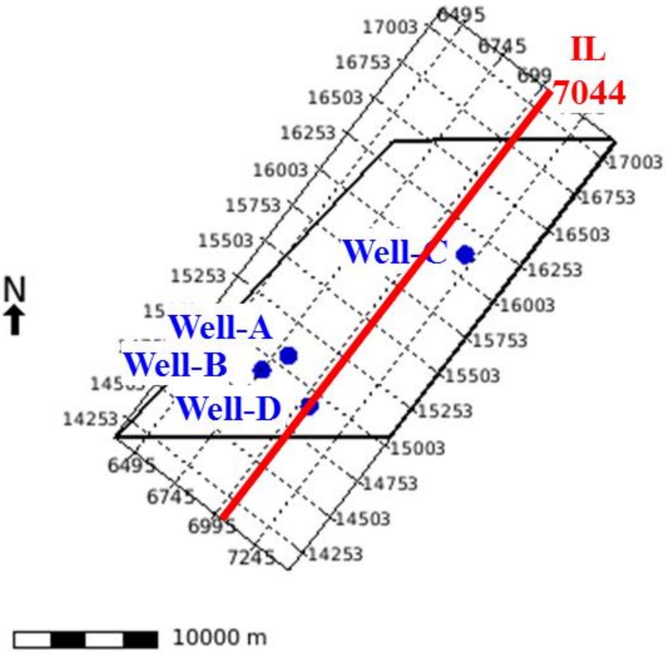

Figure D-16 Map location of inline 7044 that passed through Well-D location.

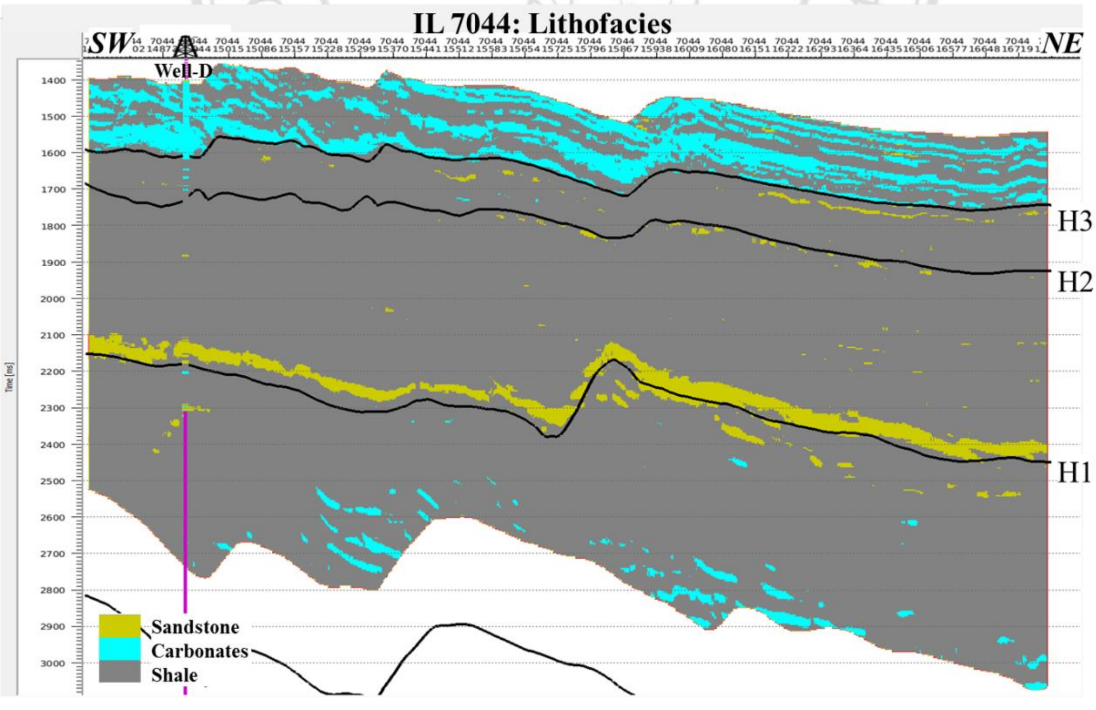

Figure D-17 Inline 7044 section showing lithology log of Well-D was properly captured by the lithofacies cube (most probable).

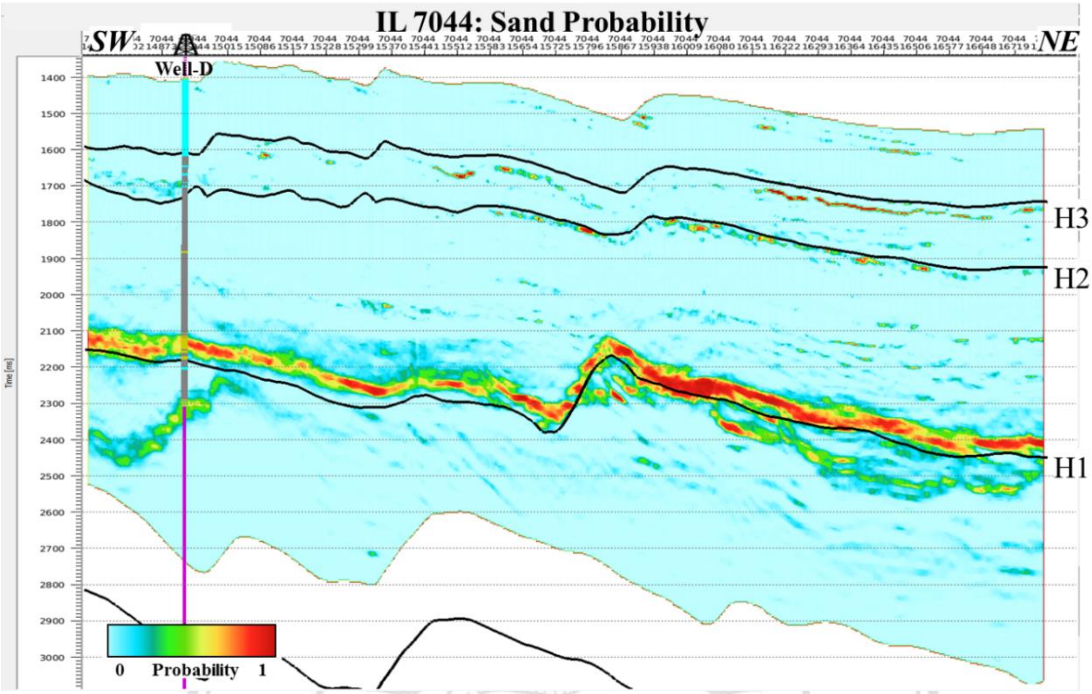

Figure D-18 Inline 7044 section showing the distribution of sand probability.

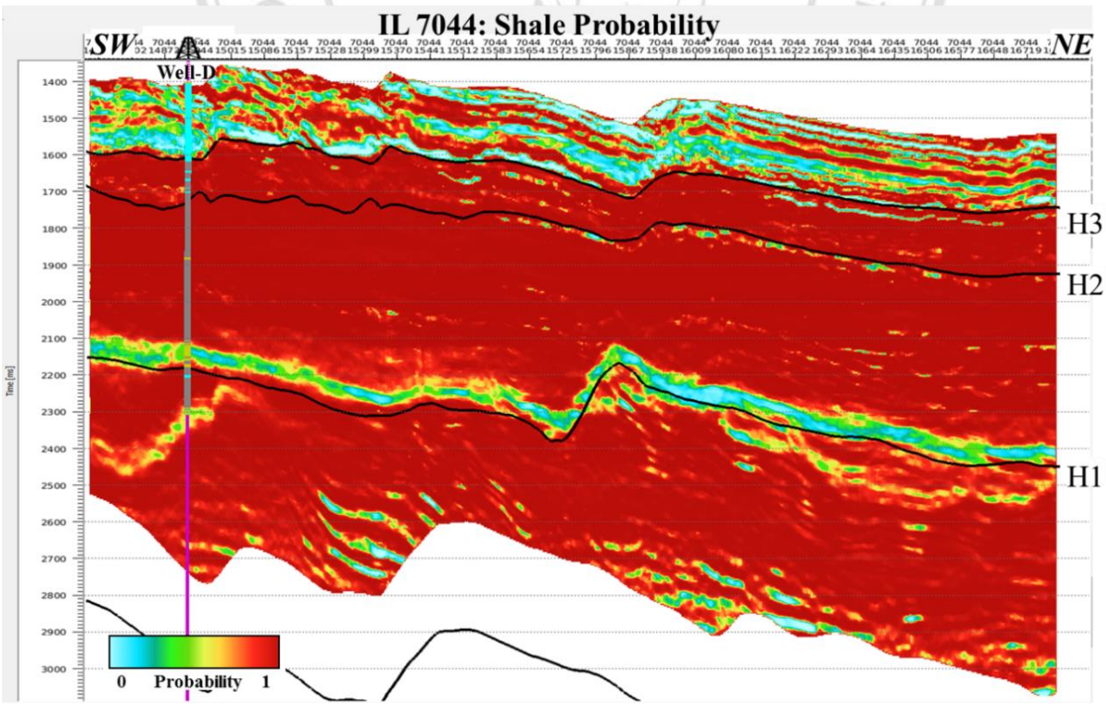

Figure D-19 Inline 7044 section showing the distribution of shale probability.

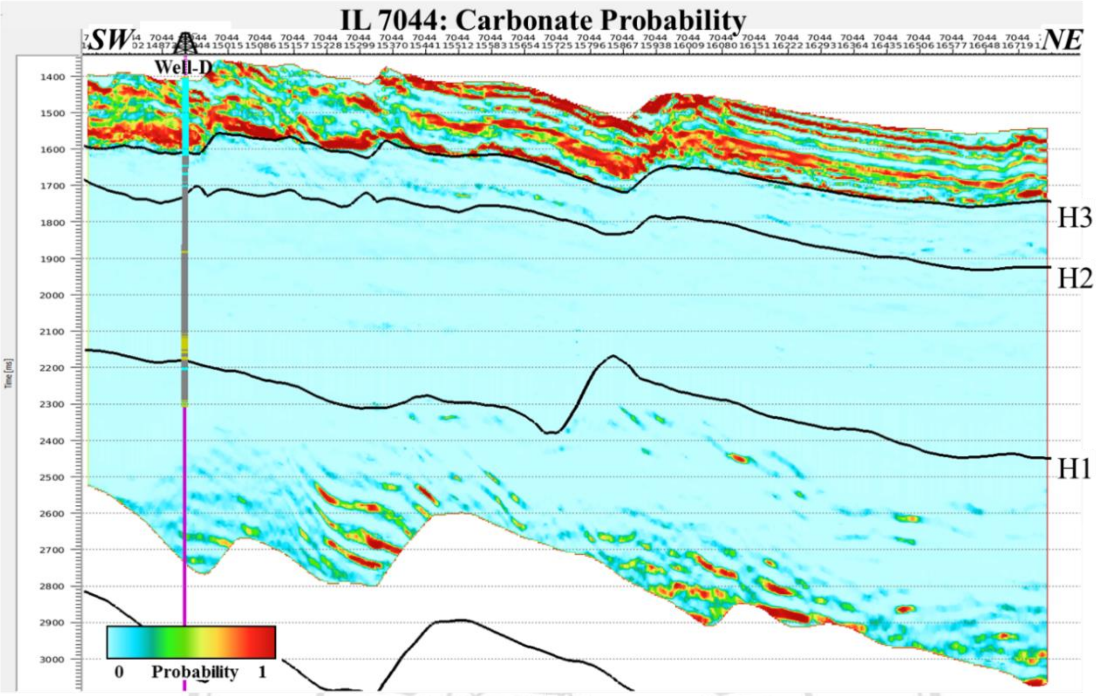

Figure D-20 Inline 7044 section showing the distribution of carbonate probability.

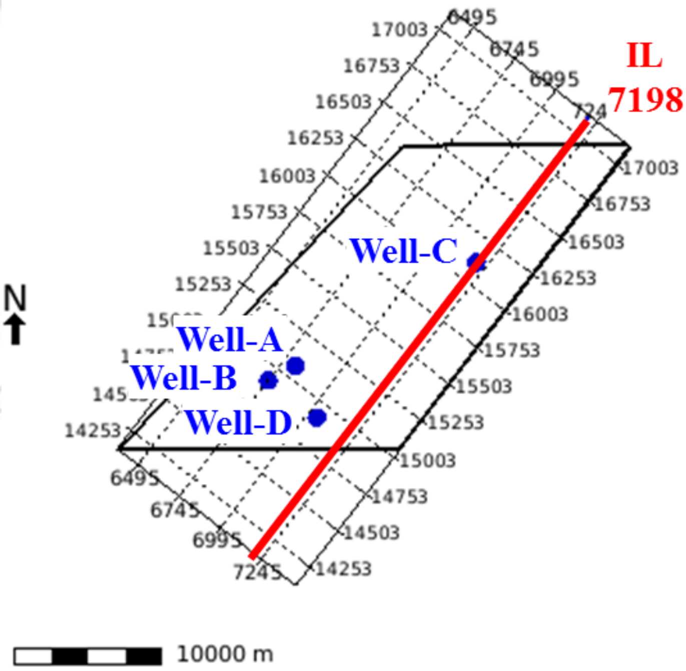

Figure D-21 Map location of inline 7198 that passed through Well-C location.

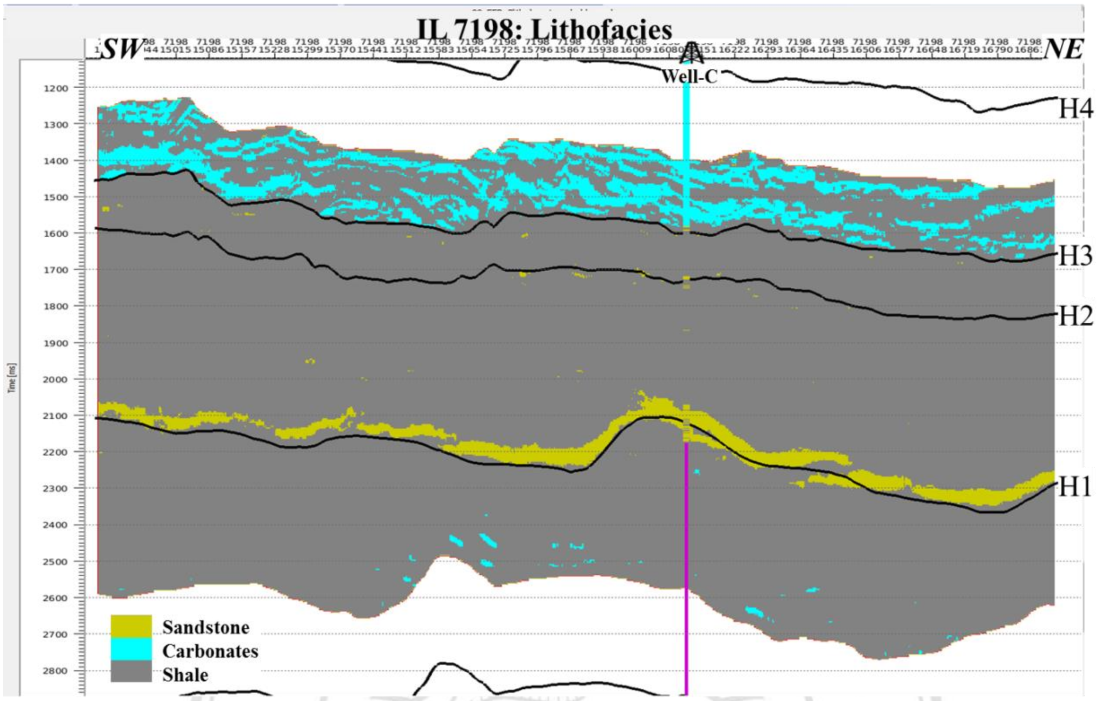

Figure D-22 Inline 7198 section showing lithology log of Well-C was properly captured by the lithofacies cube (most probable).

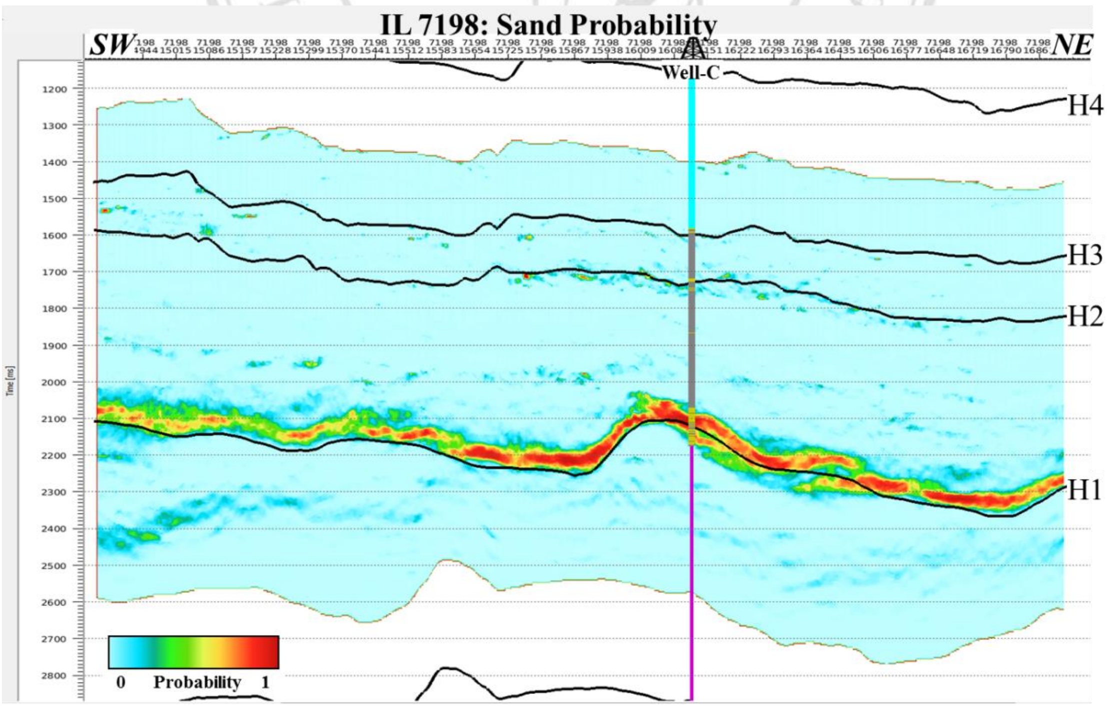

Figure D-23 Inline 7198 section showing the distribution of sand probability.

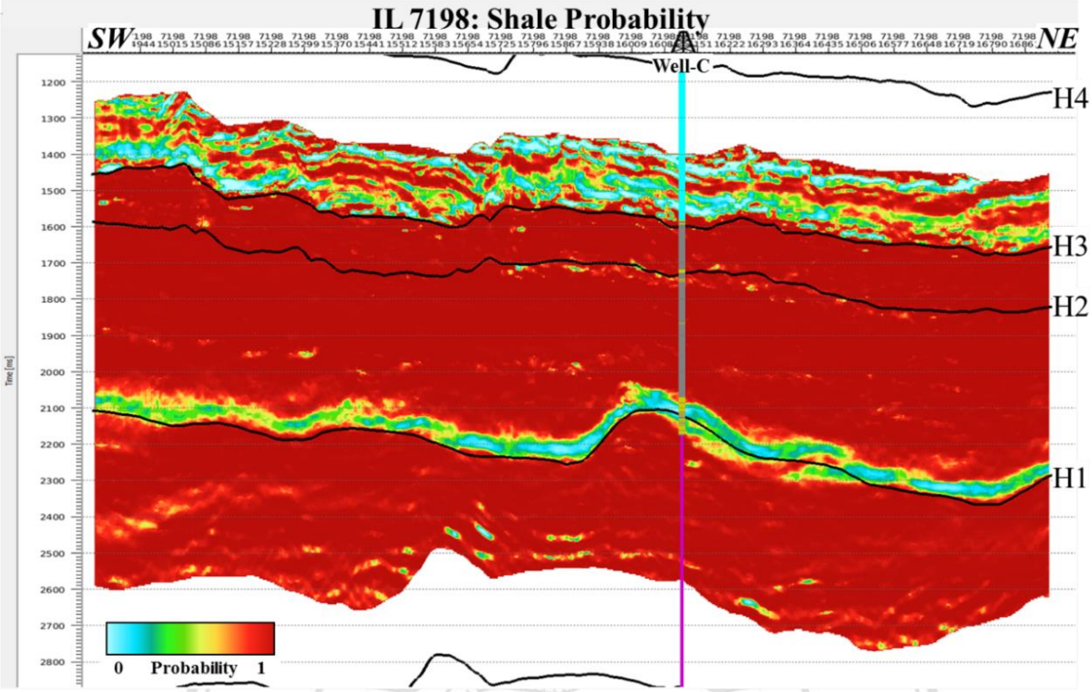

Figure D-24 Inline 7198 section showing the distribution of shale probability.

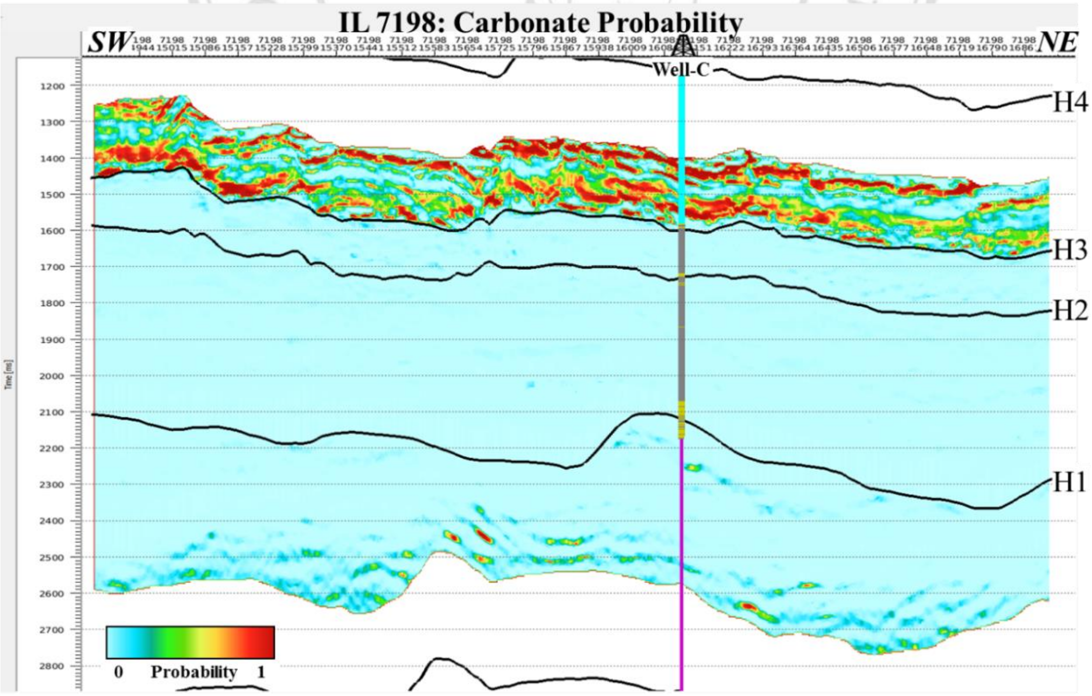

Figure D-25 Inline 7198 section showing the distribution of carbonate probability.

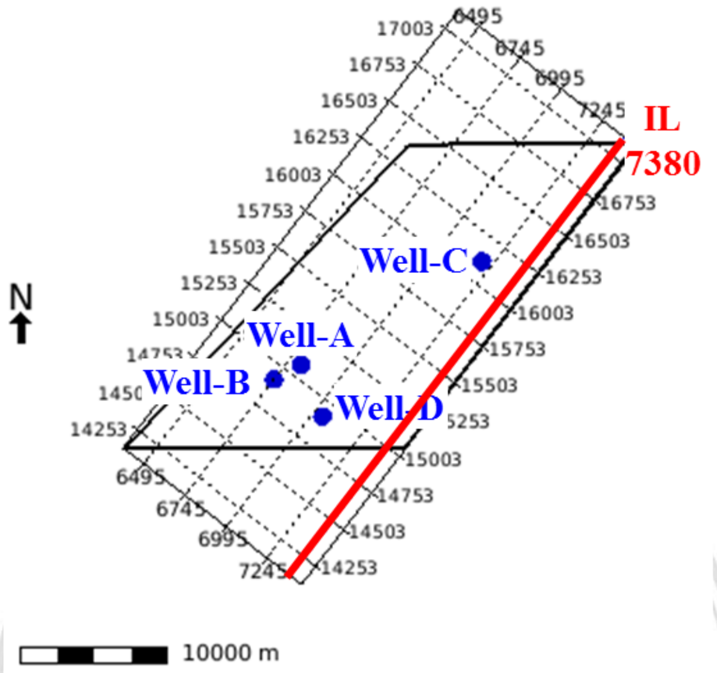

Figure D-26 Map location of inline 7380.

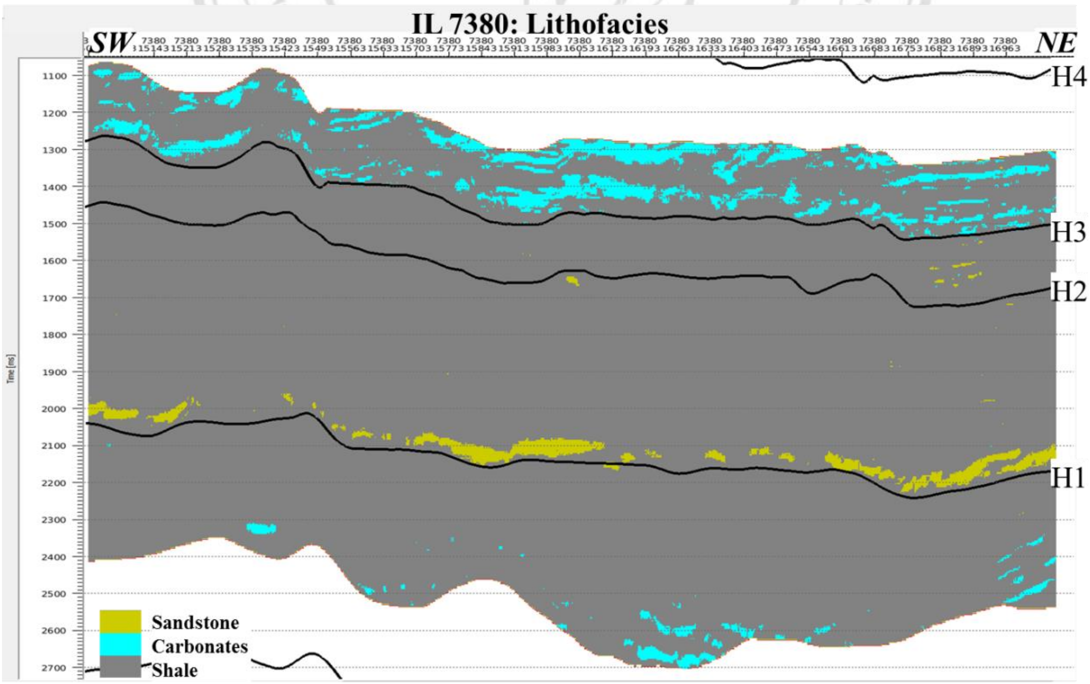

Figure D-27 Inline 7380 section showing lithofacies (most probable).

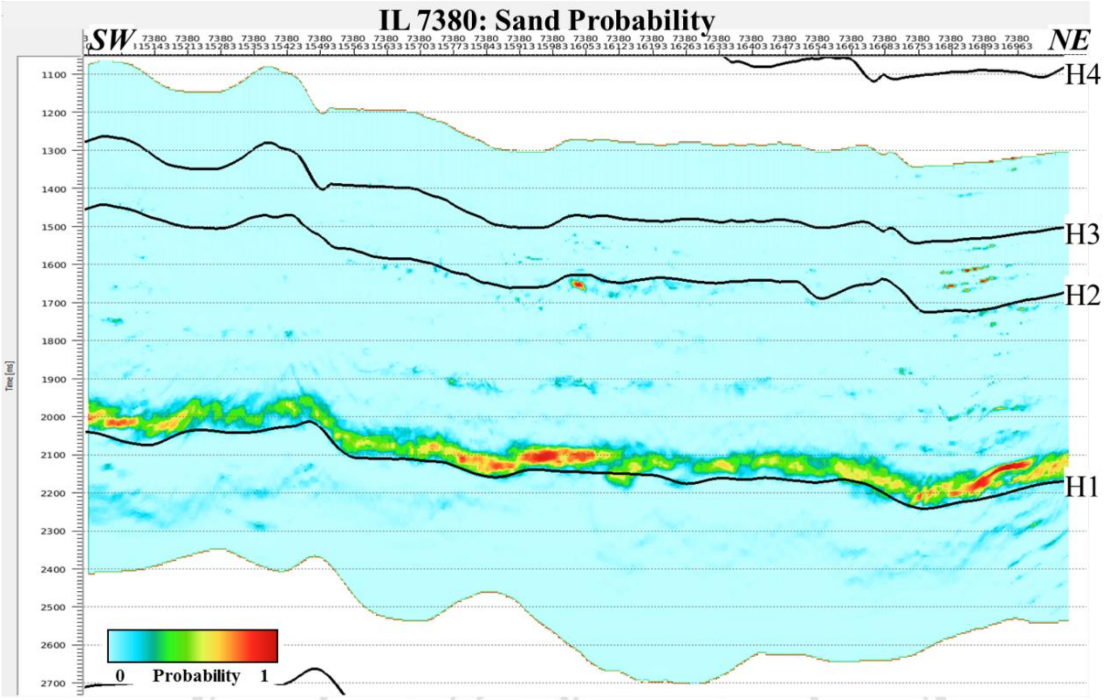

Figure D-28 Inline 7380 section showing the distribution of sand probability.

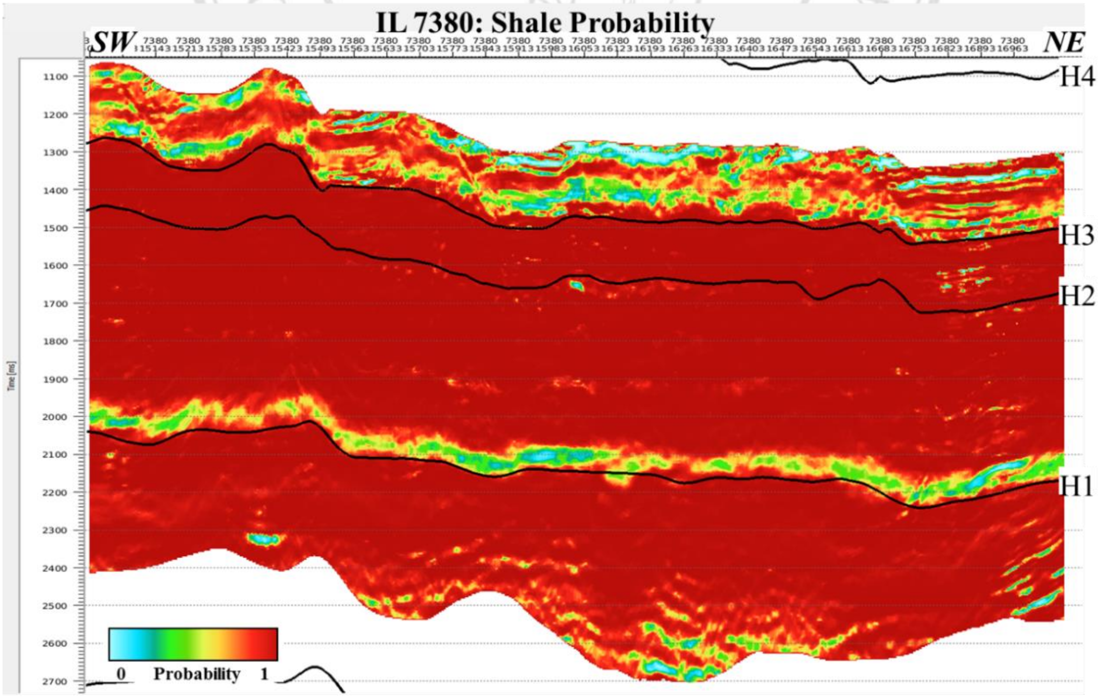

Figure D-29 Inline 7380 section showing the distribution of shale probability.

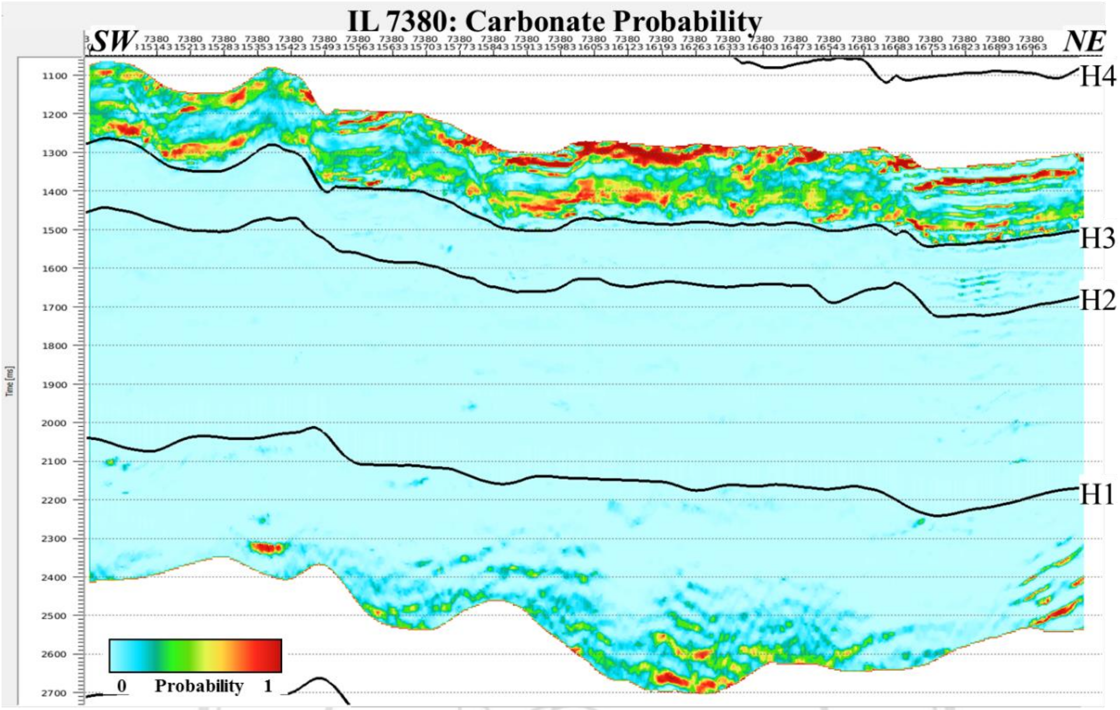

Figure D-30 Inline 7380 section showing the distribution of carbonate probability.

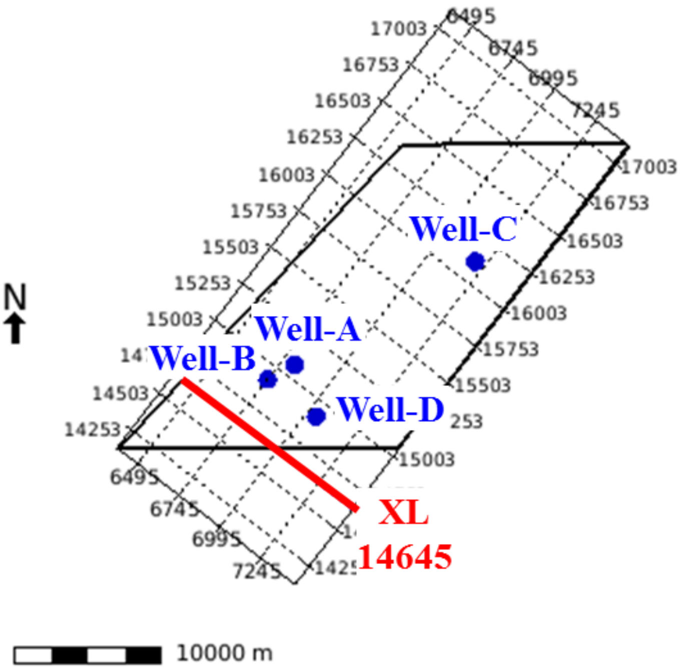

Figure D-31 Map location of crossline 14645.

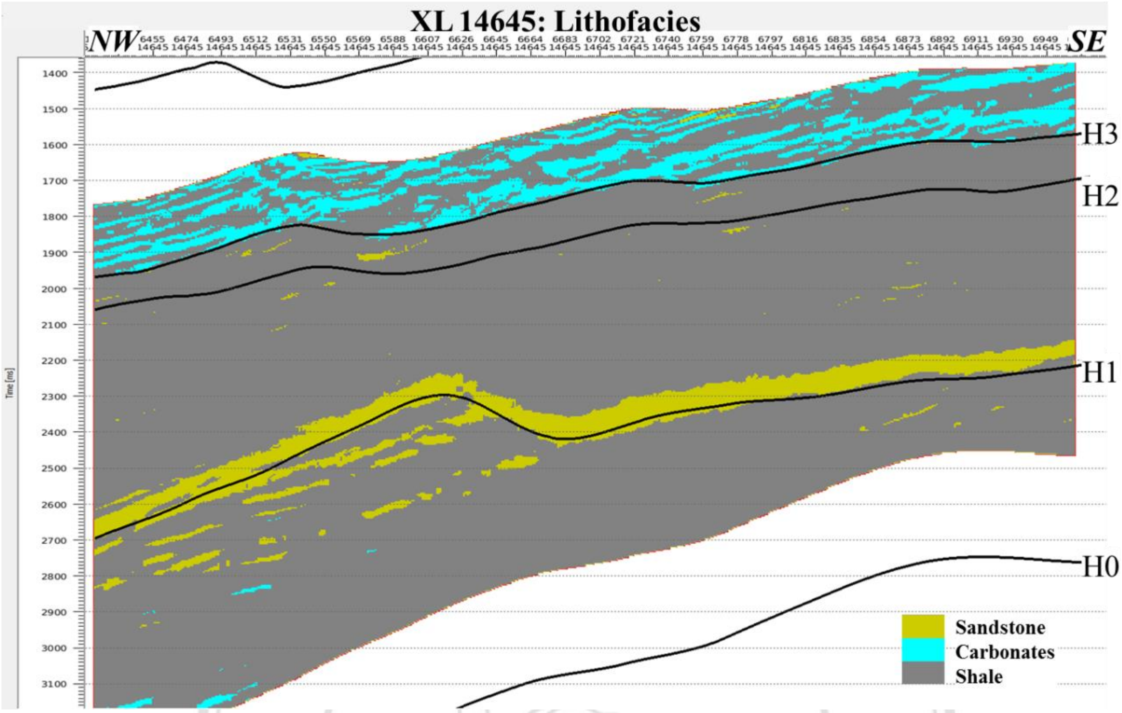

Figure D-32 Crossline 14645 section showing lithofacies (most probable).

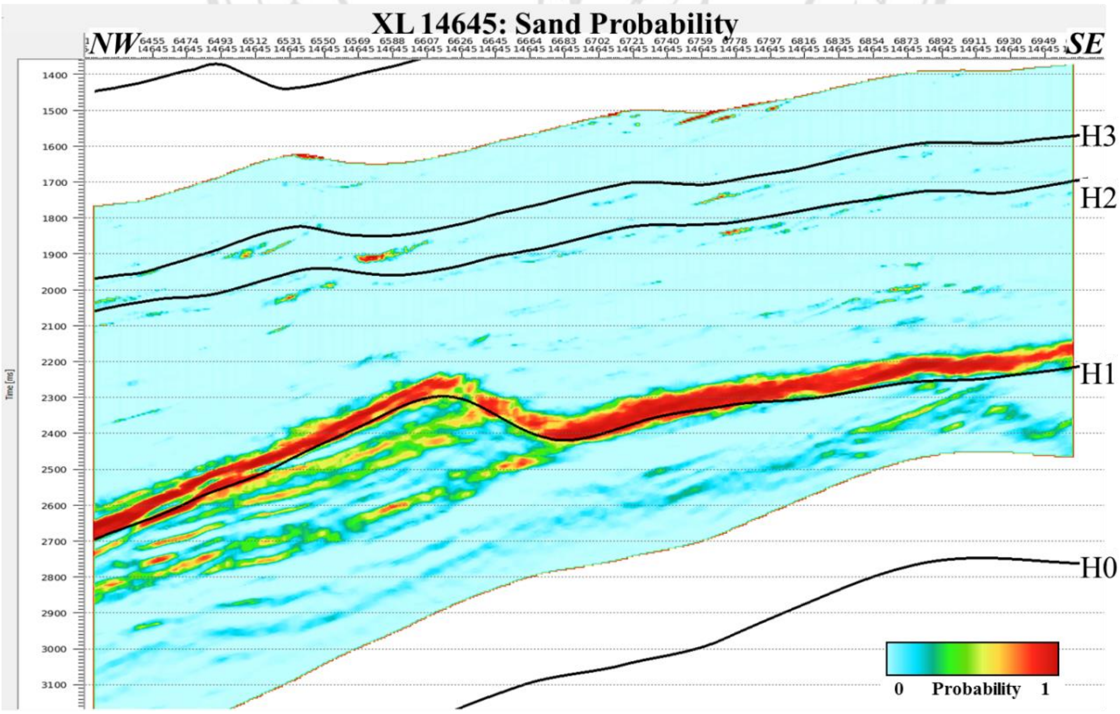

Figure D-33 Crossline 14645 section showing the distribution of sand probability.

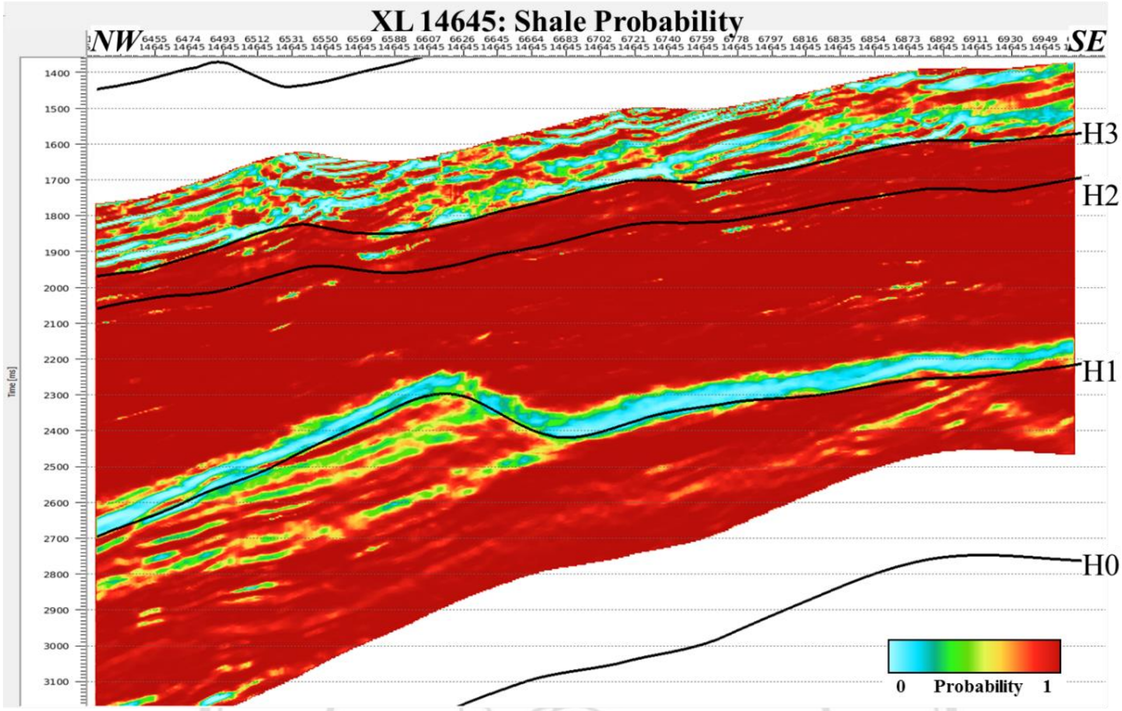

Figure D-34 Crossline 14645 section showing the distribution of shale probability.

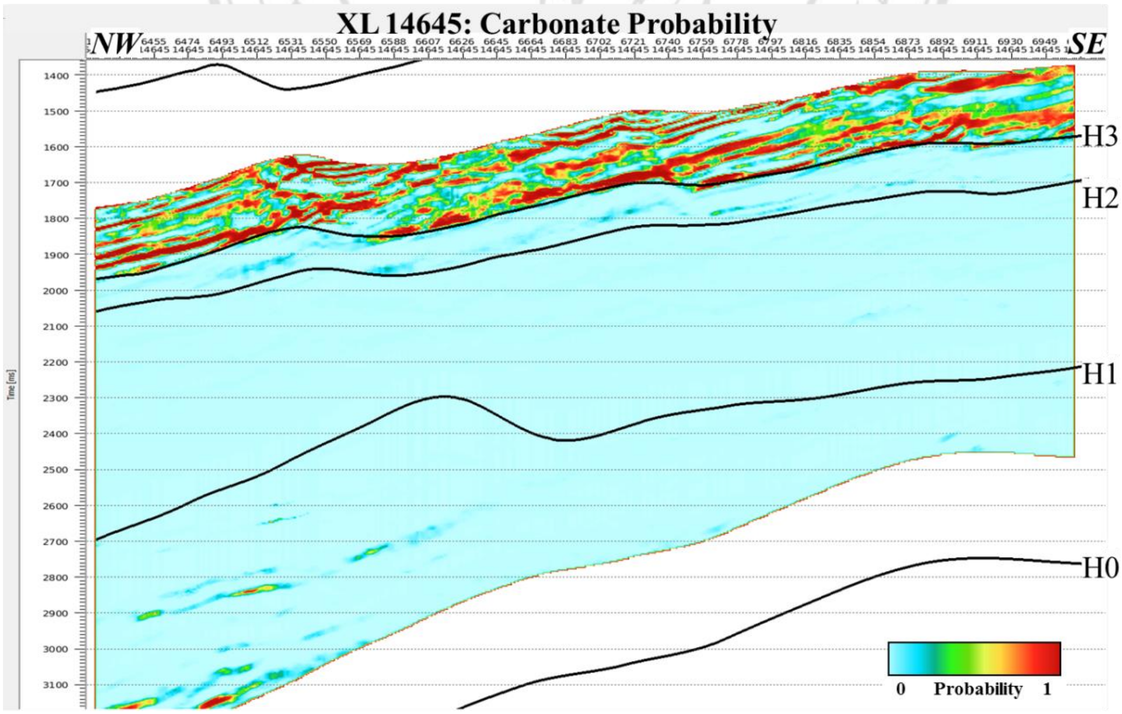

Figure D-35 Crossline 14645 section showing the distribution of carbonate probability.

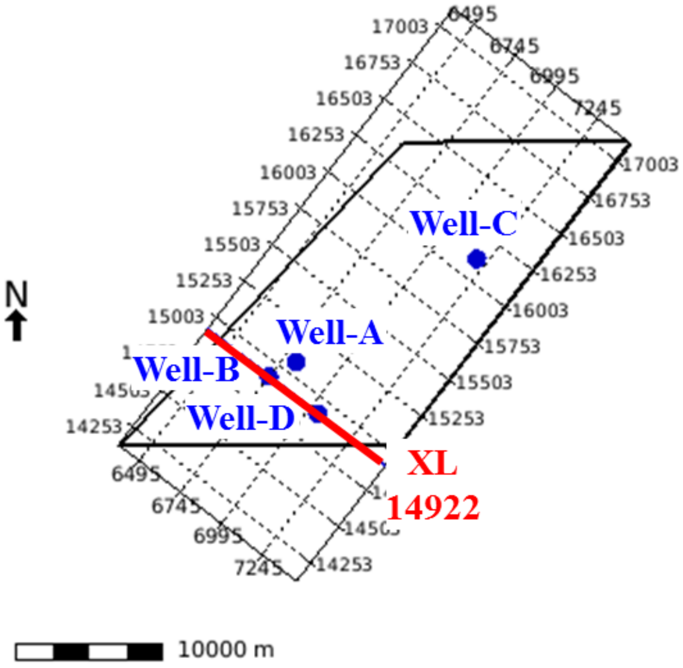

Figure D-36 Map location of crossline 14922 that passed through Wells-B and -D location.

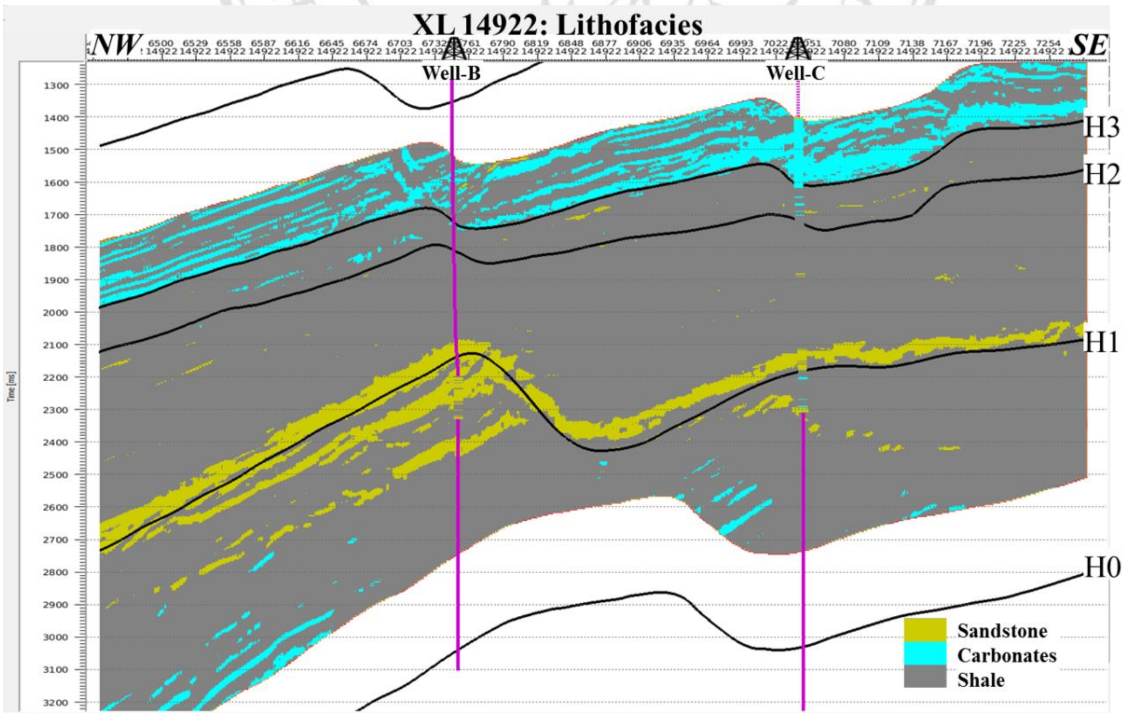

Figure D-37 Crossline 14922 section showing lithology logs of Wells-B and -D were properly captured by the lithofacies cube (most probable).

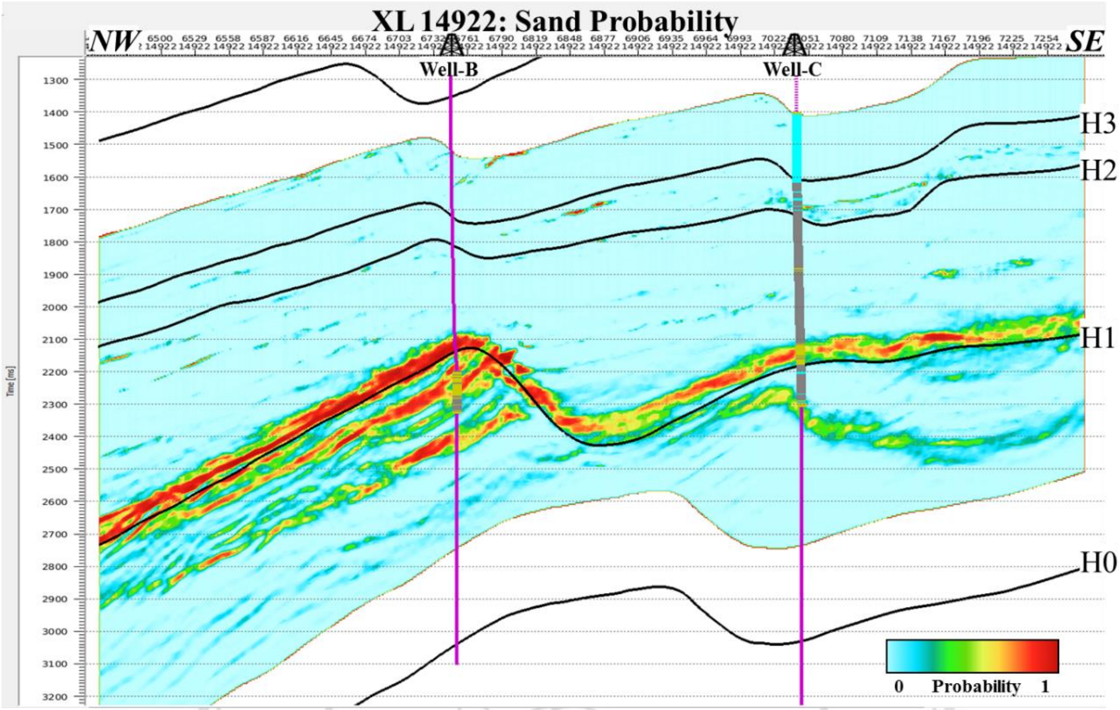

Figure D-38 Crossline 14922 section showing the distribution of sand probability.

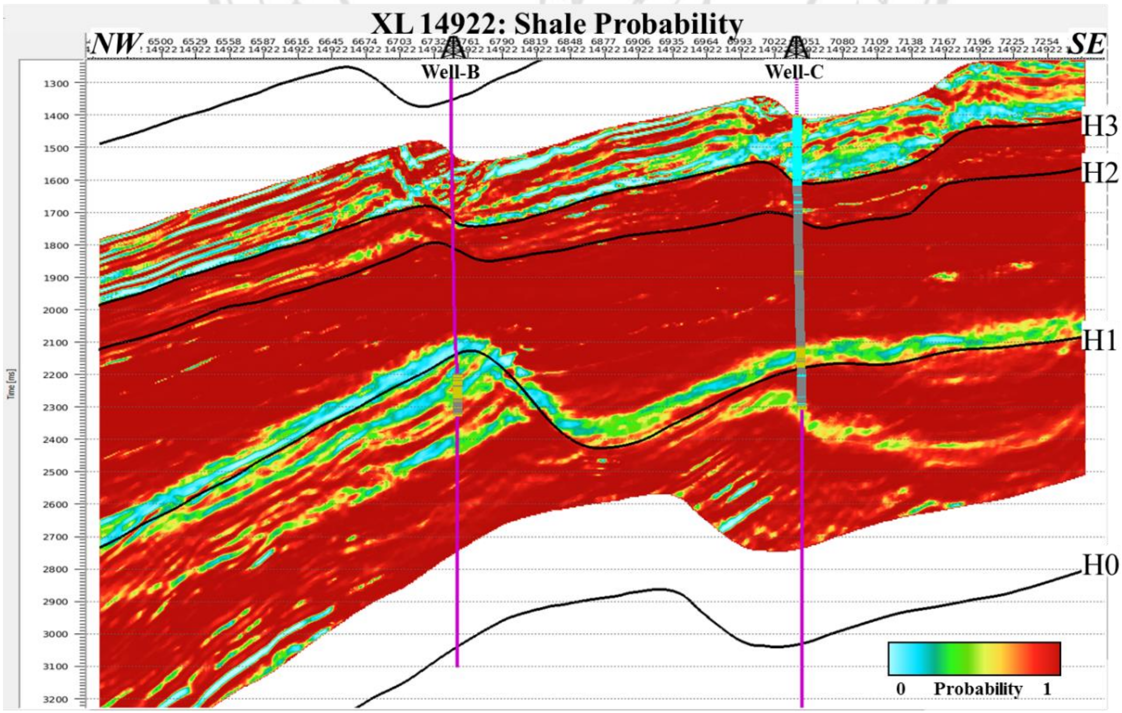

Figure D-39 Crossline 14922 section showing the distribution of shale probability.

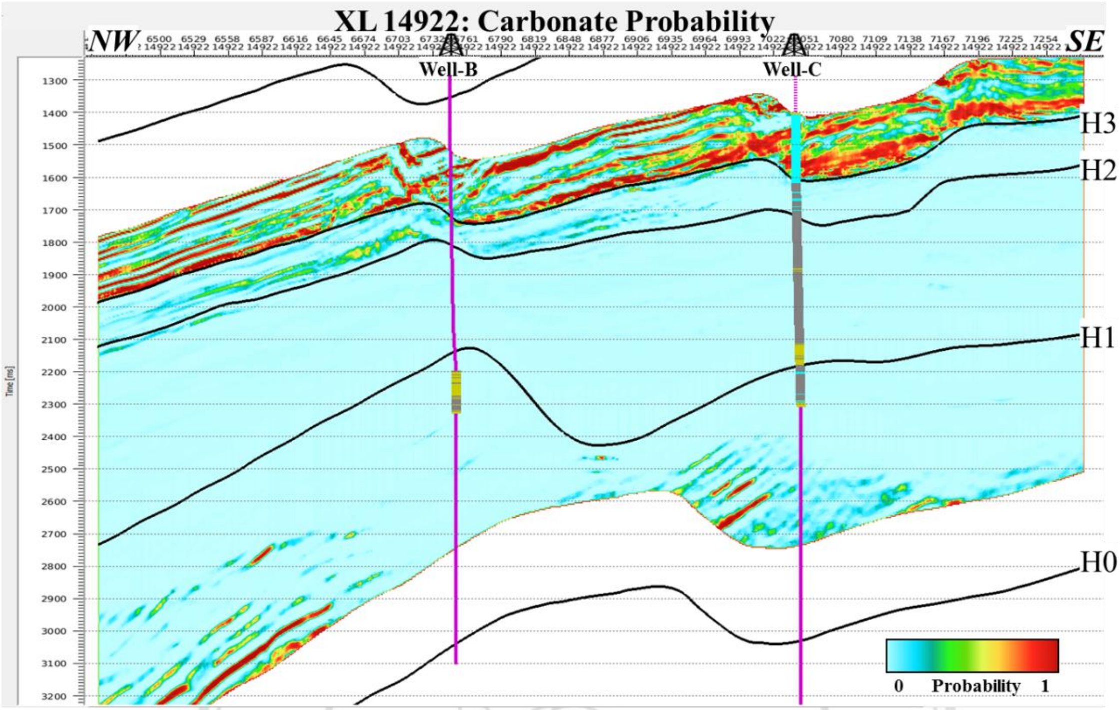

Figure D-40 Crossline 14922 section showing the distribution of carbonate probability.

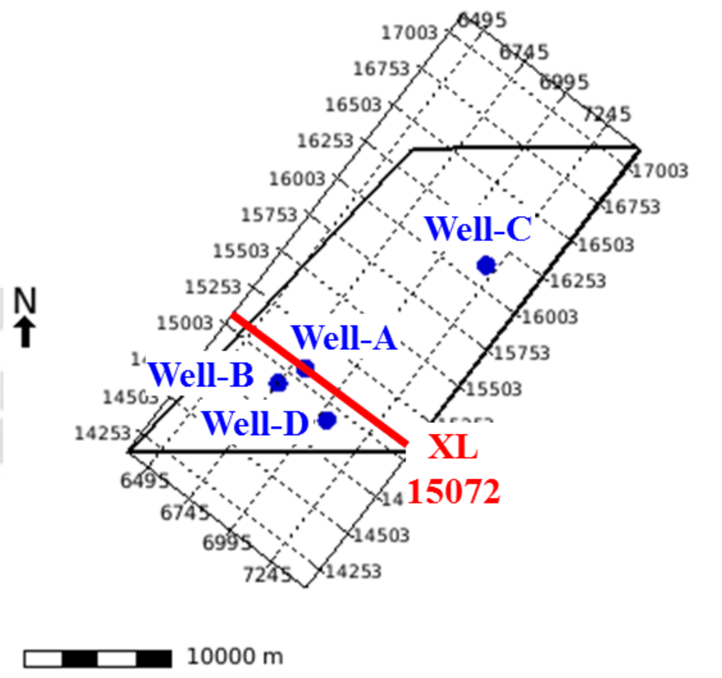

Figure D-41 Map location of crossline 15072 that passed through Well-A location.

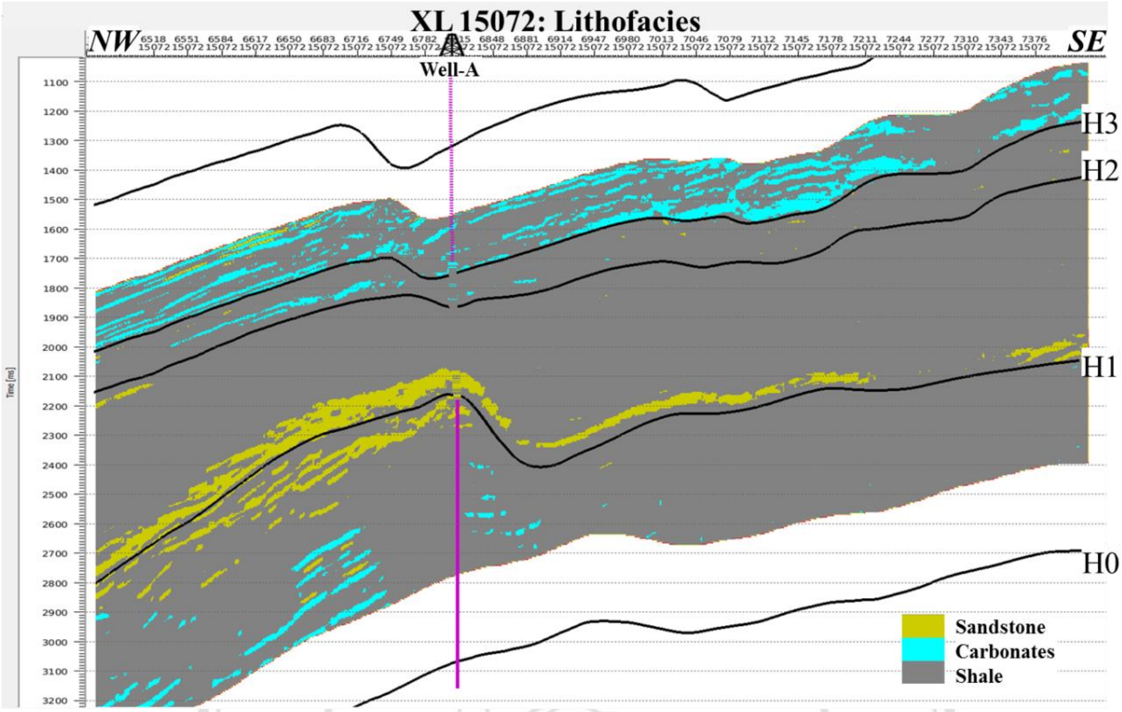

Figure D-42 Crossline 15072 section showing lithology logs of Well-A was properly captured by the lithofacies cube (most probable).

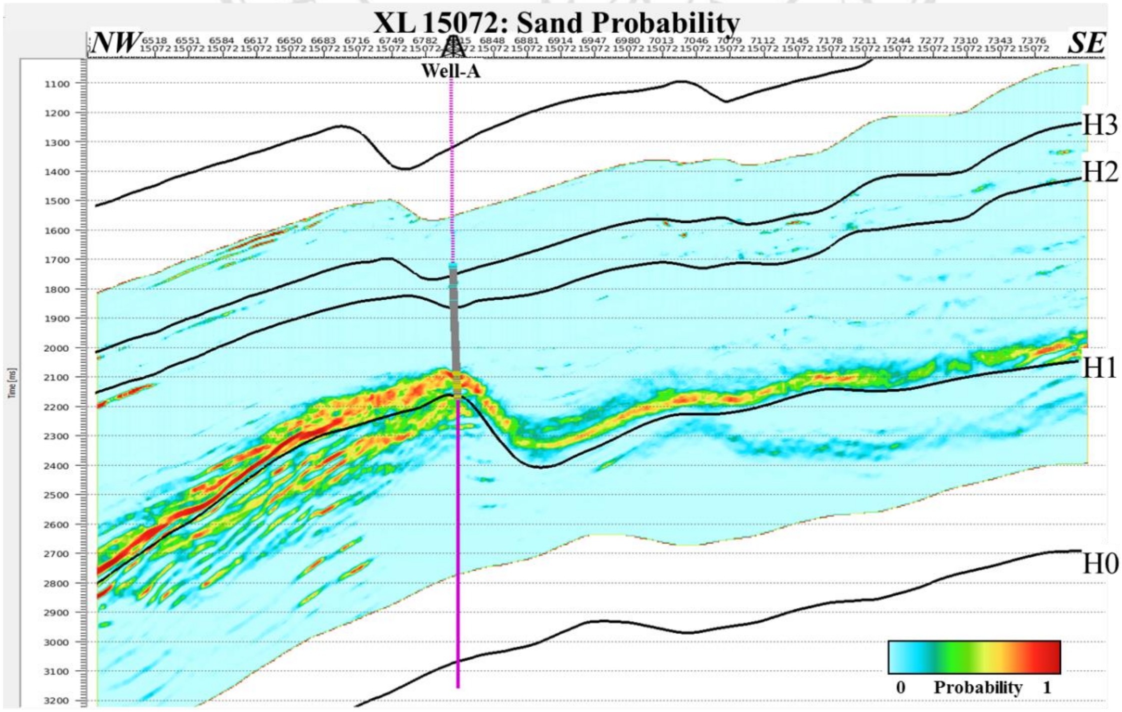

Figure D-43 Crossline 15072 section showing the distribution of sand probability.

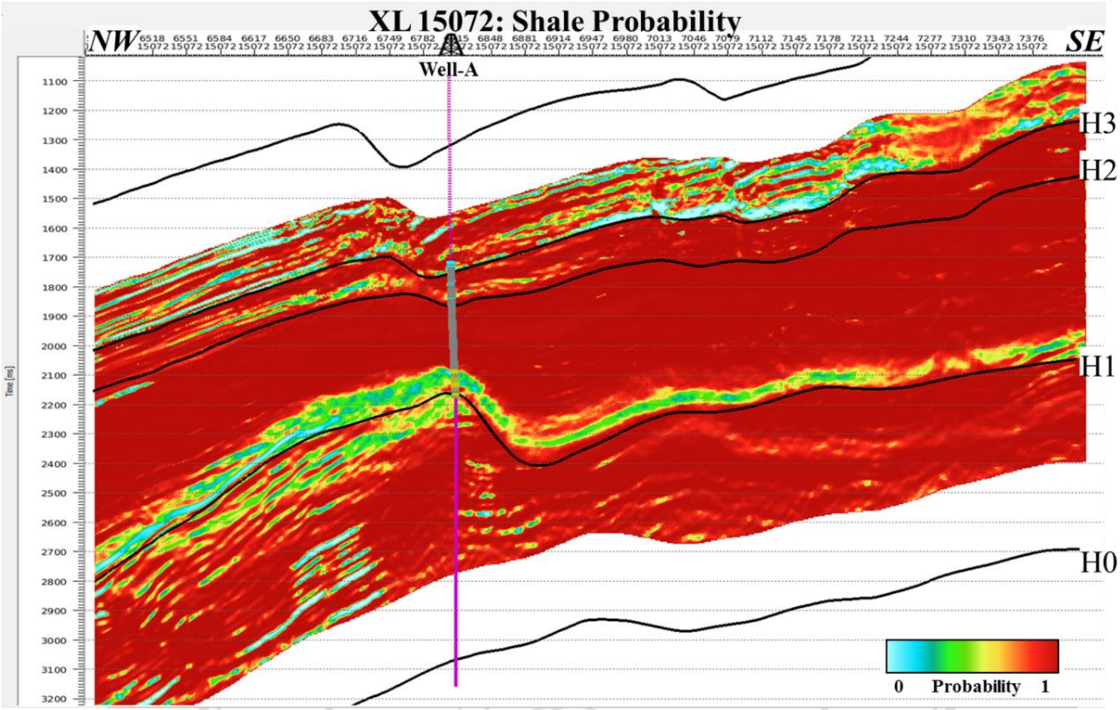

Figure D-44 Crossline 15072 section showing the distribution of shale probability.

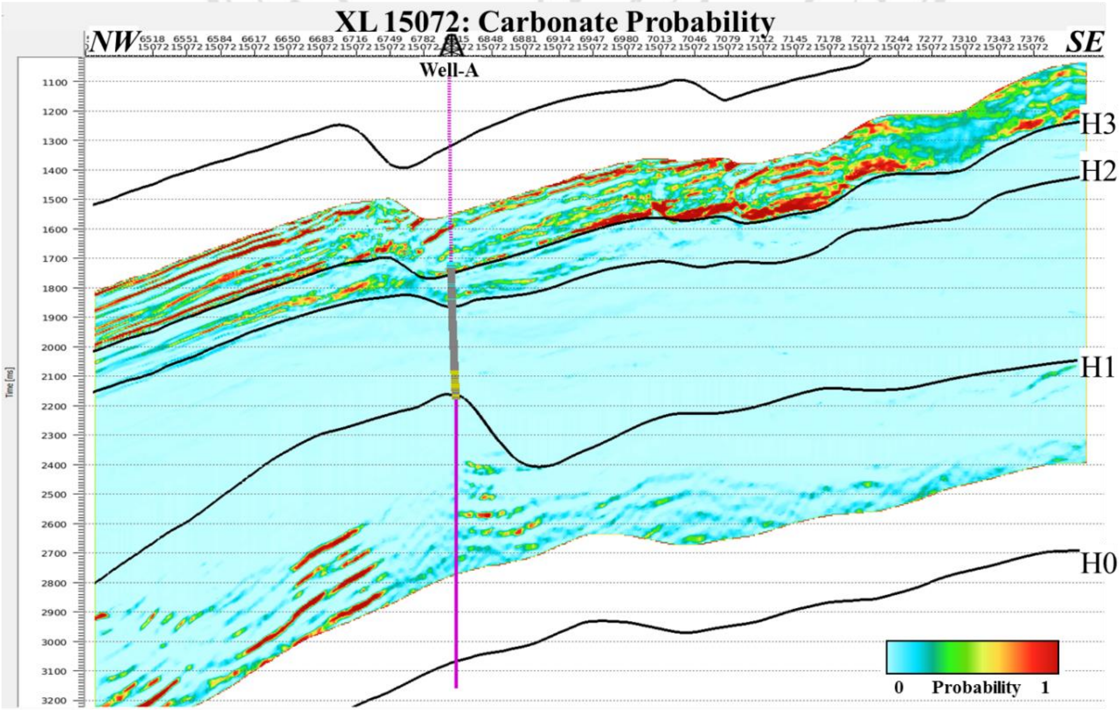

Figure D-45 Crossline 15072 section showing the distribution of carbonate probability

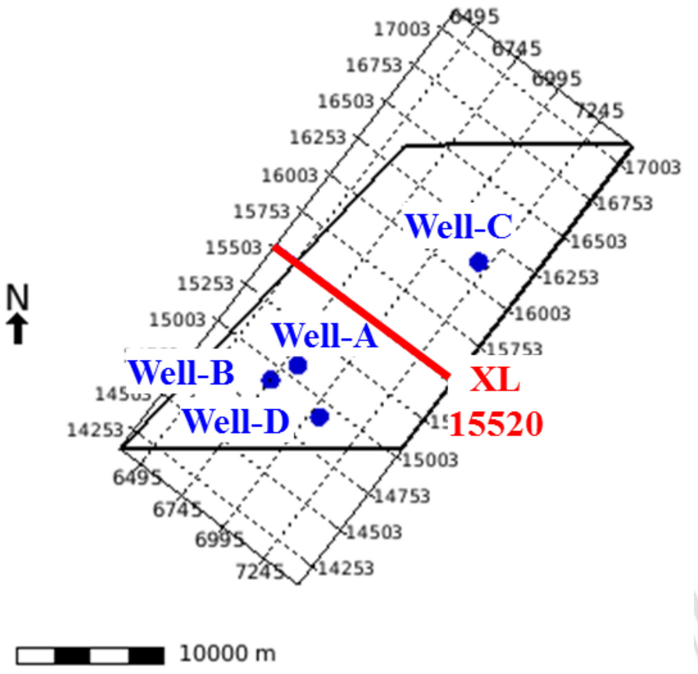

Figure D-46 Map location of crossline 15520.

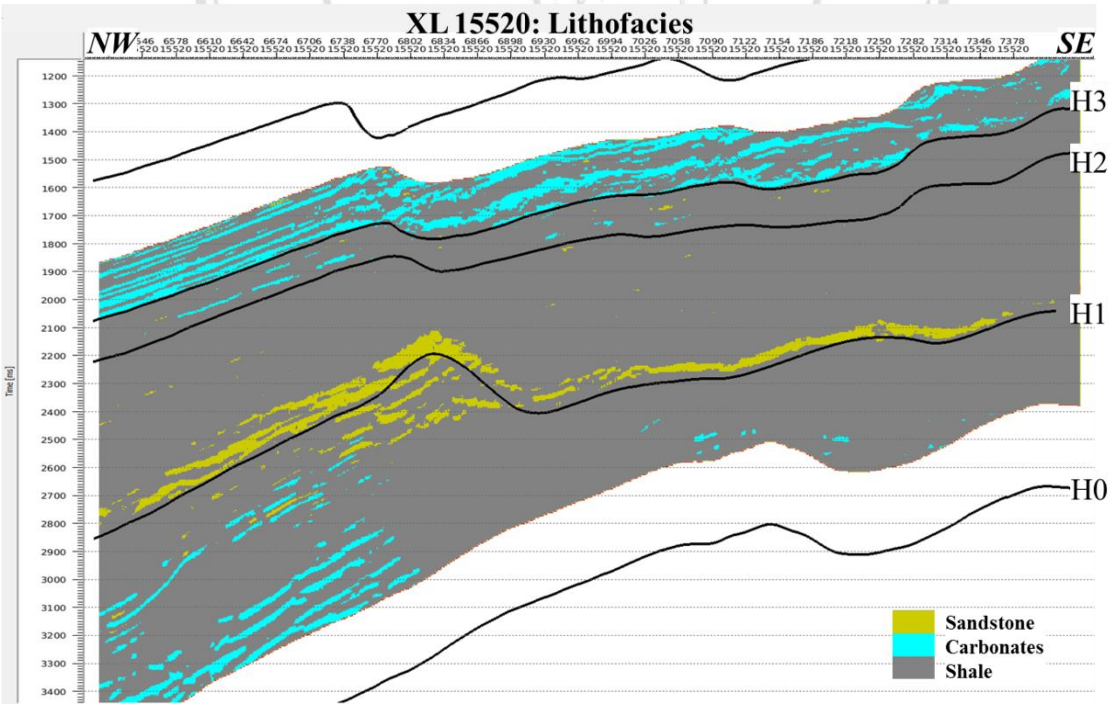

Figure D-47 Crossline 15520 section showing lithofacies cube (most probable).

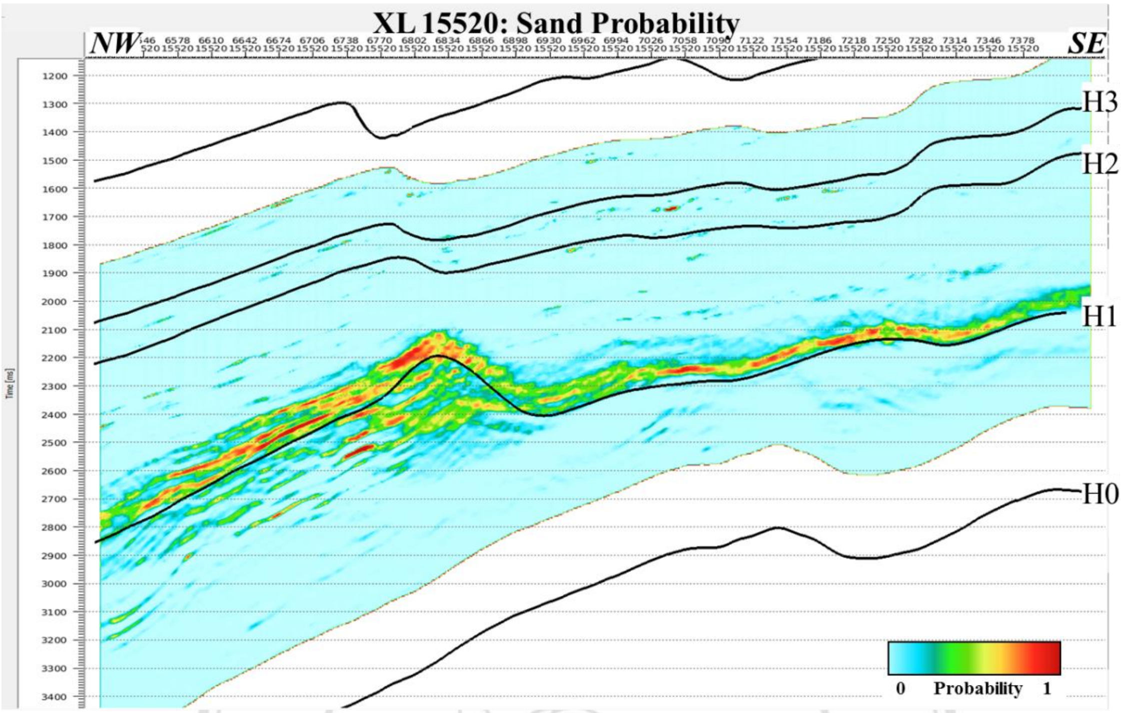

Figure D-48 Crossline 15520 section showing the distribution of sand probability.

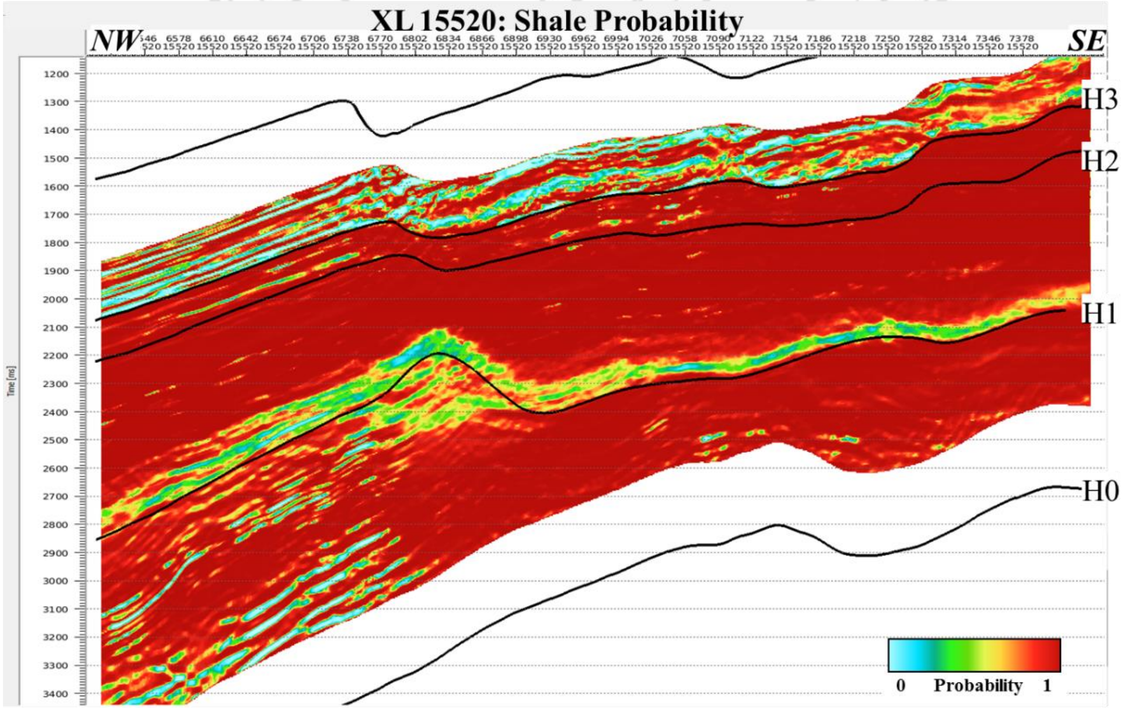

Figure D-49 Crossline 15520 section showing the distribution of shale probability.

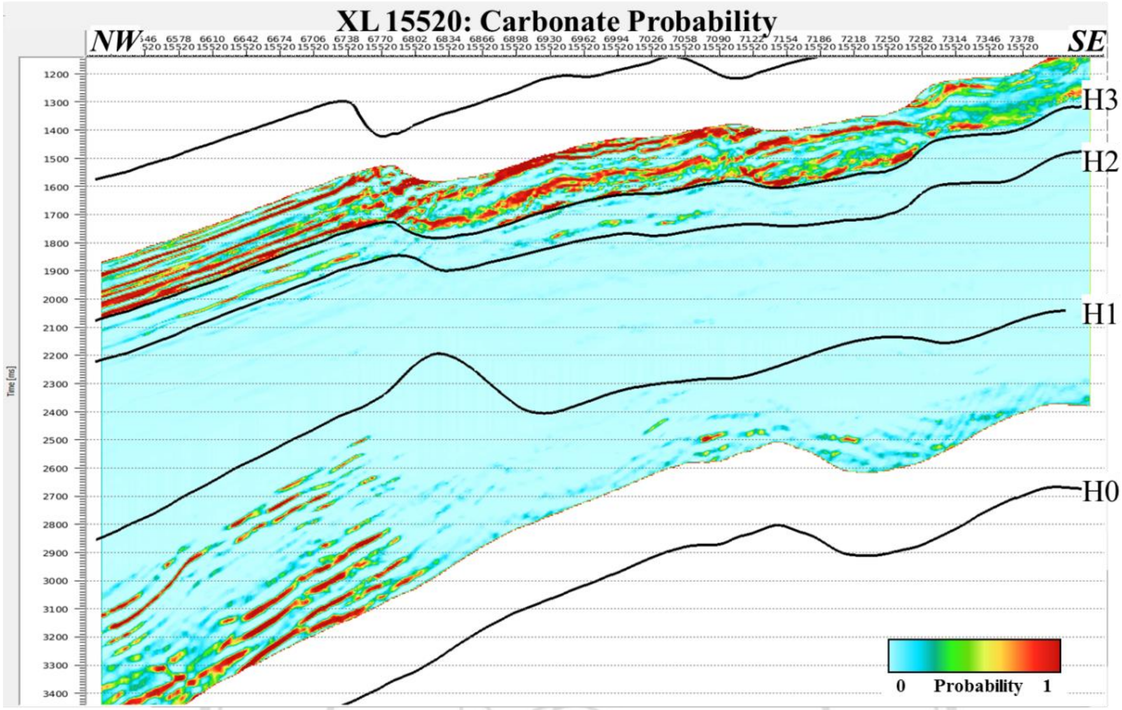

Figure D-50 Crossline 15520 section showing the distribution of carbonate probability.

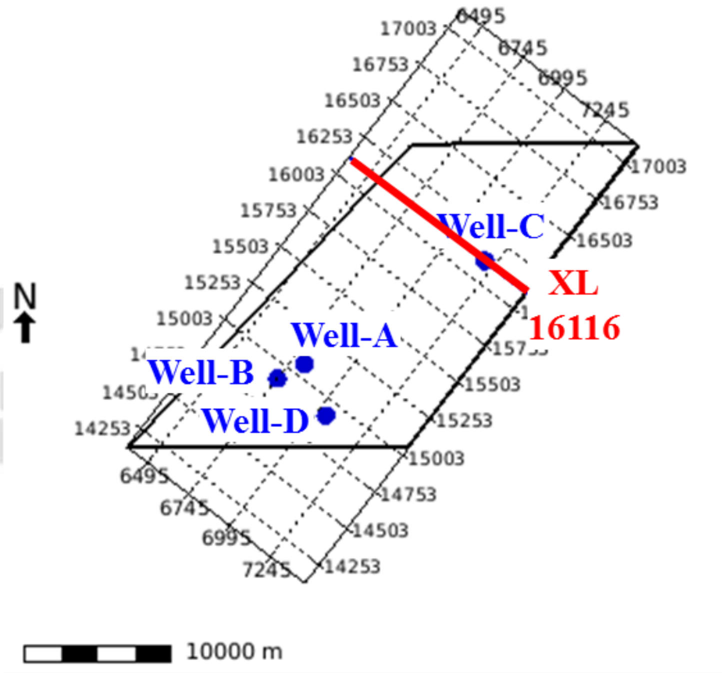

Figure D-51 Map location of crossline 16116 that passed through Well-C location.

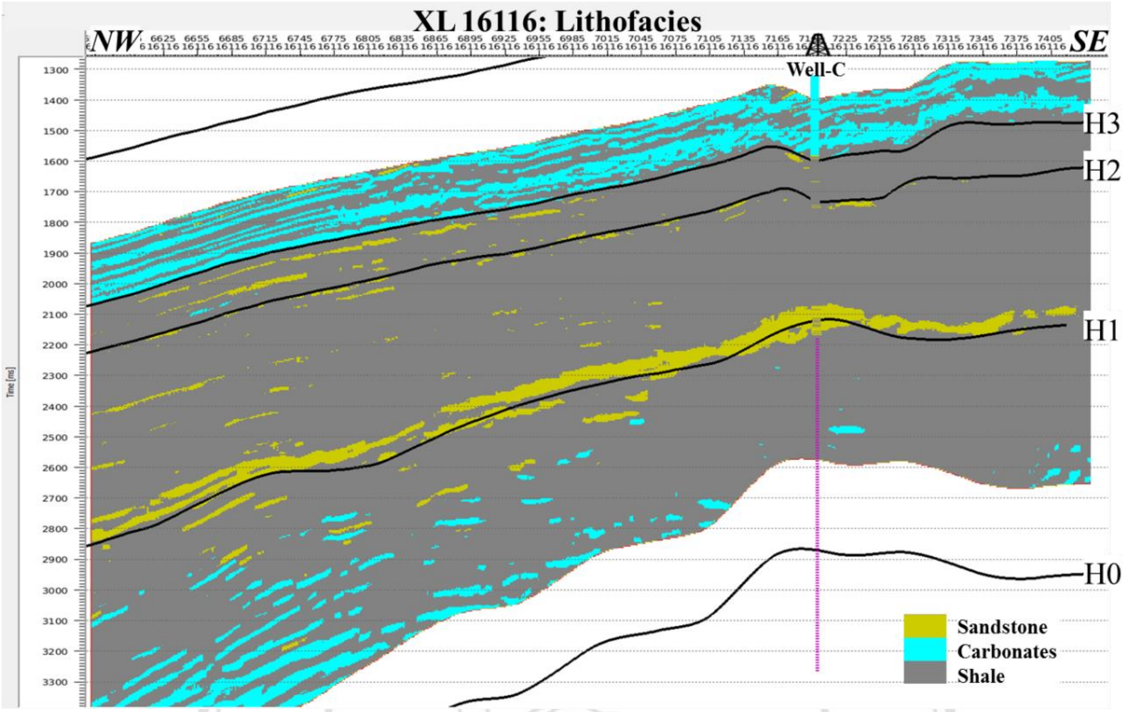

Figure D-52 Crossline 16116 section showing lithology logs of Well-C was properly captured by the lithofacies cube (most probable).

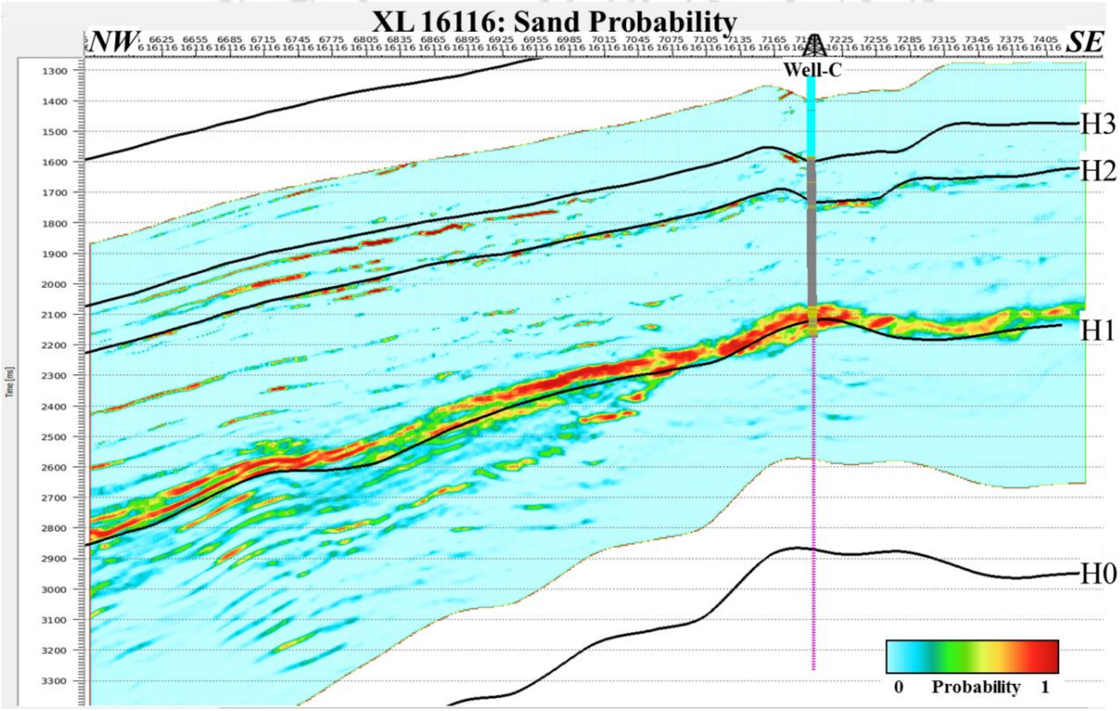

Figure D-53 Crossline 16116 section showing the distribution of sand probability.

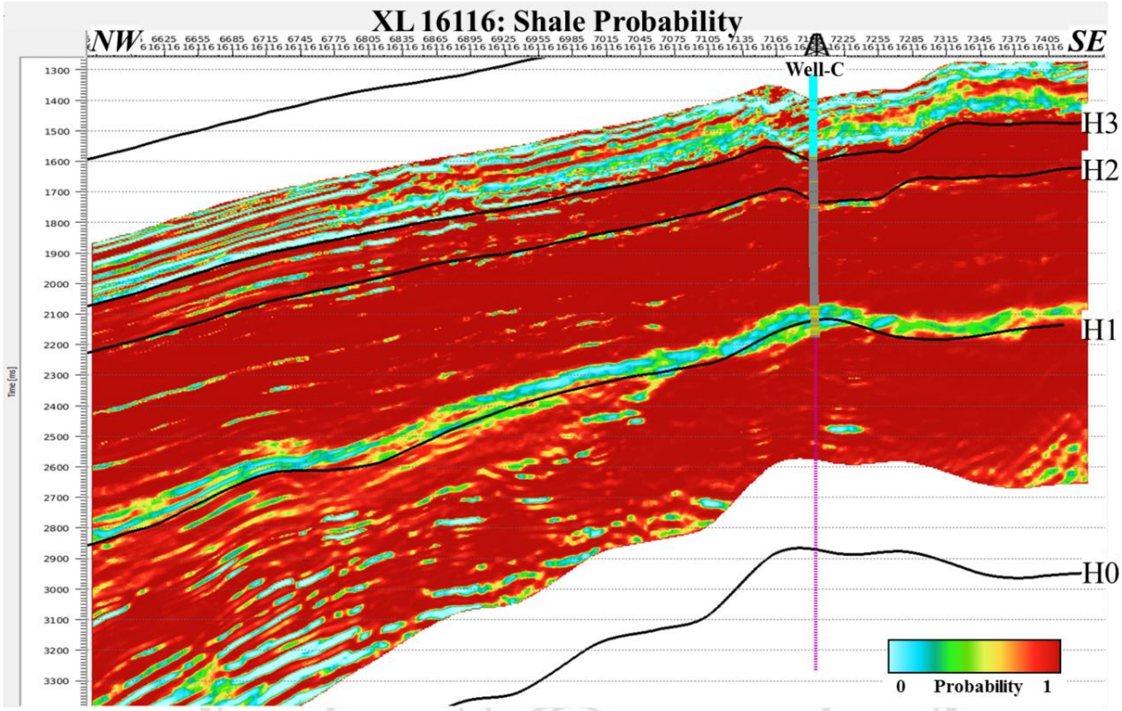

Figure D-54 Crossline 16116 section showing the distribution of shale probability.

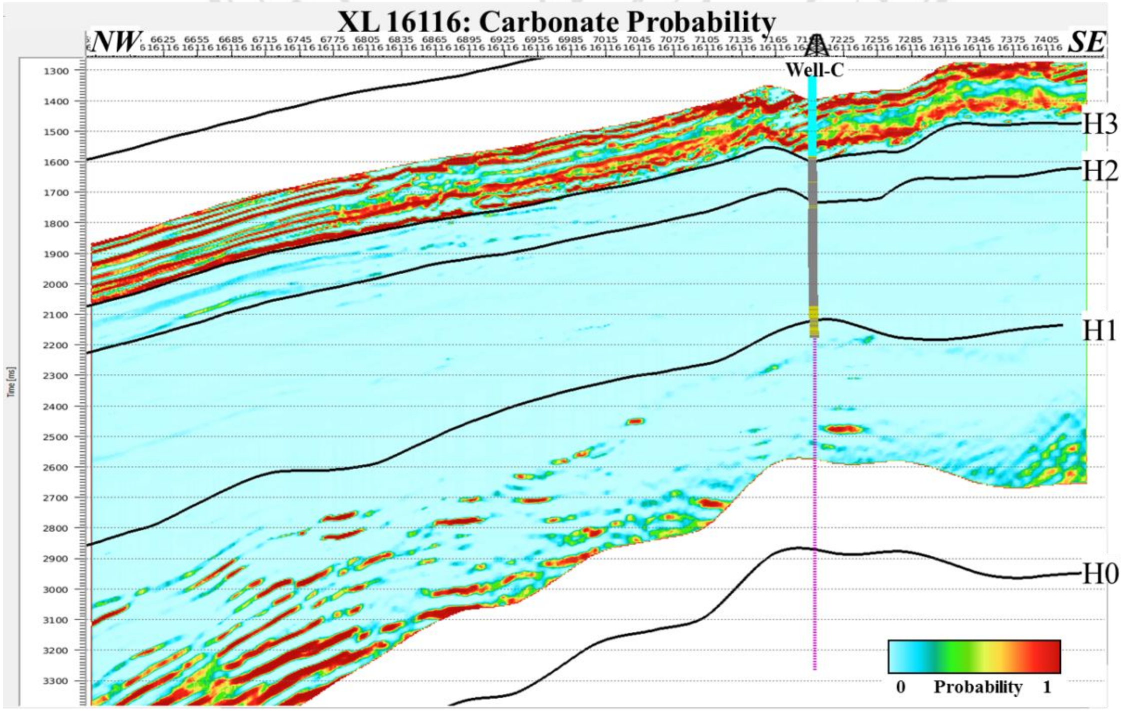

Figure D-55 Crossline 16116 section showing the distribution of carbonate probability.

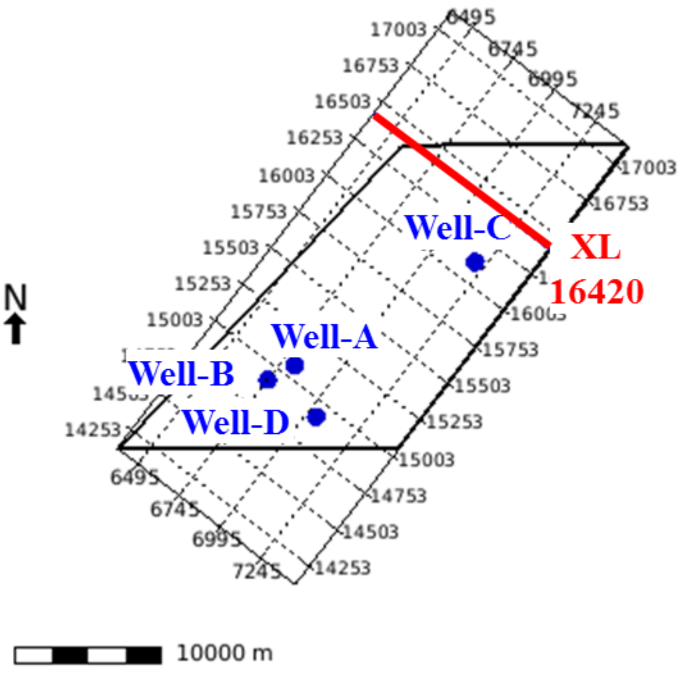

Figure D-56 Map location of crossline 16420.

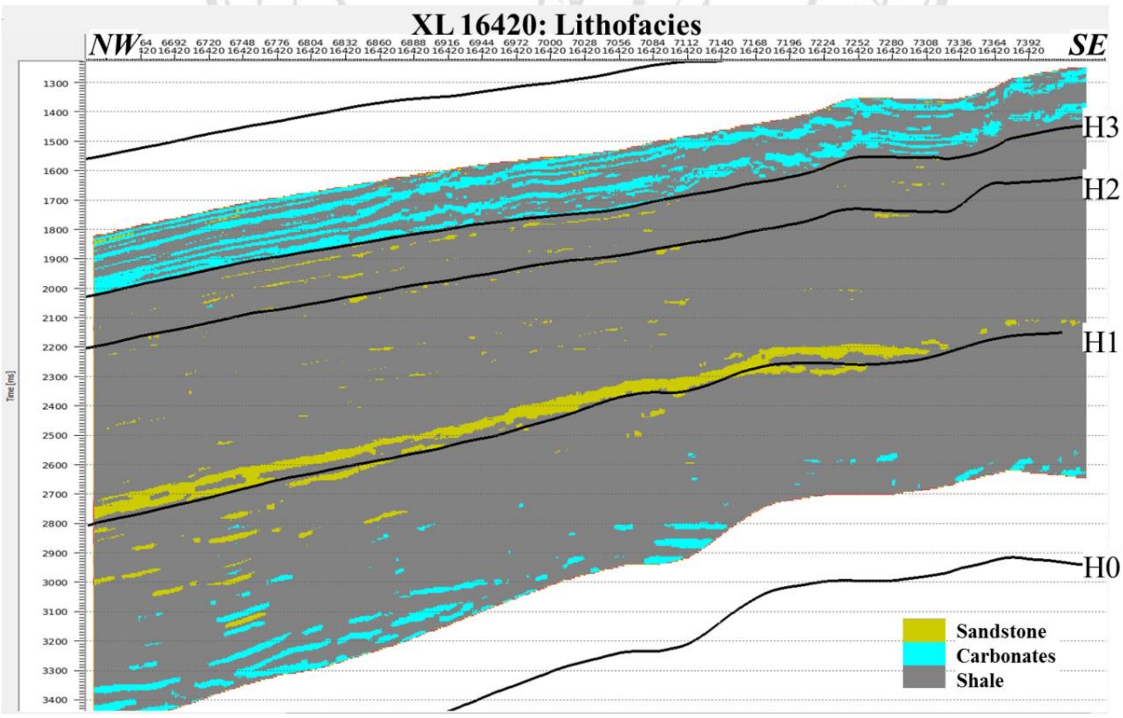

Figure D-57 Crossline 16420 section showing lithofacies (most probable).

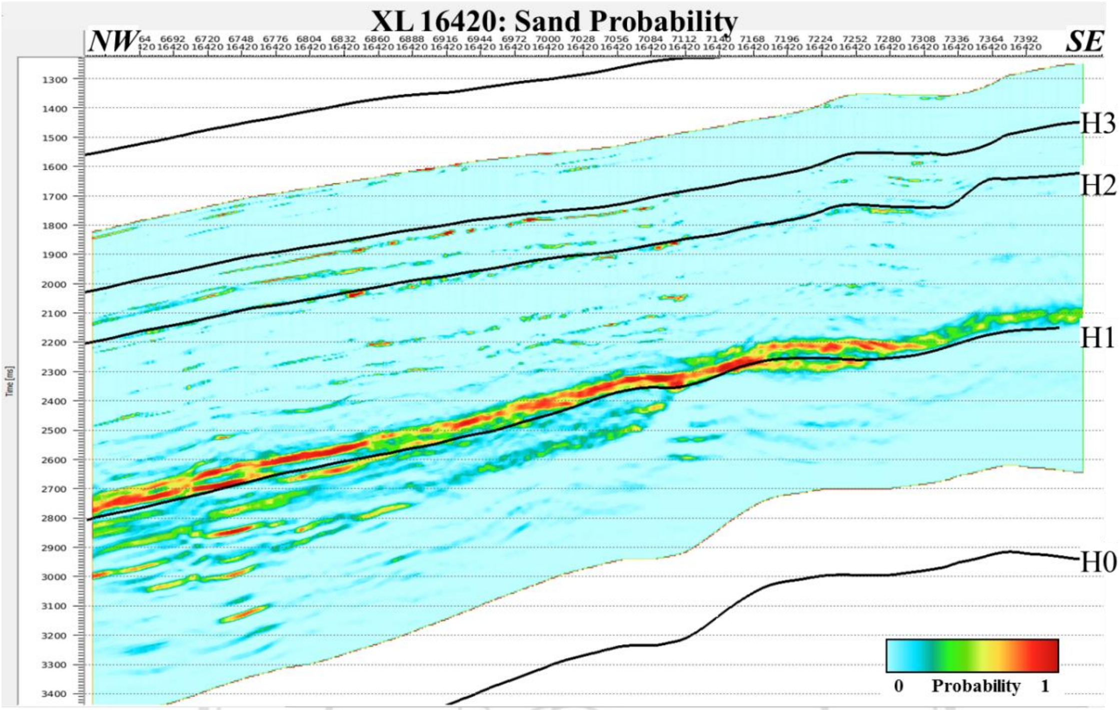

Figure D-58 Crossline 16420 section showing the distribution of sand probability.

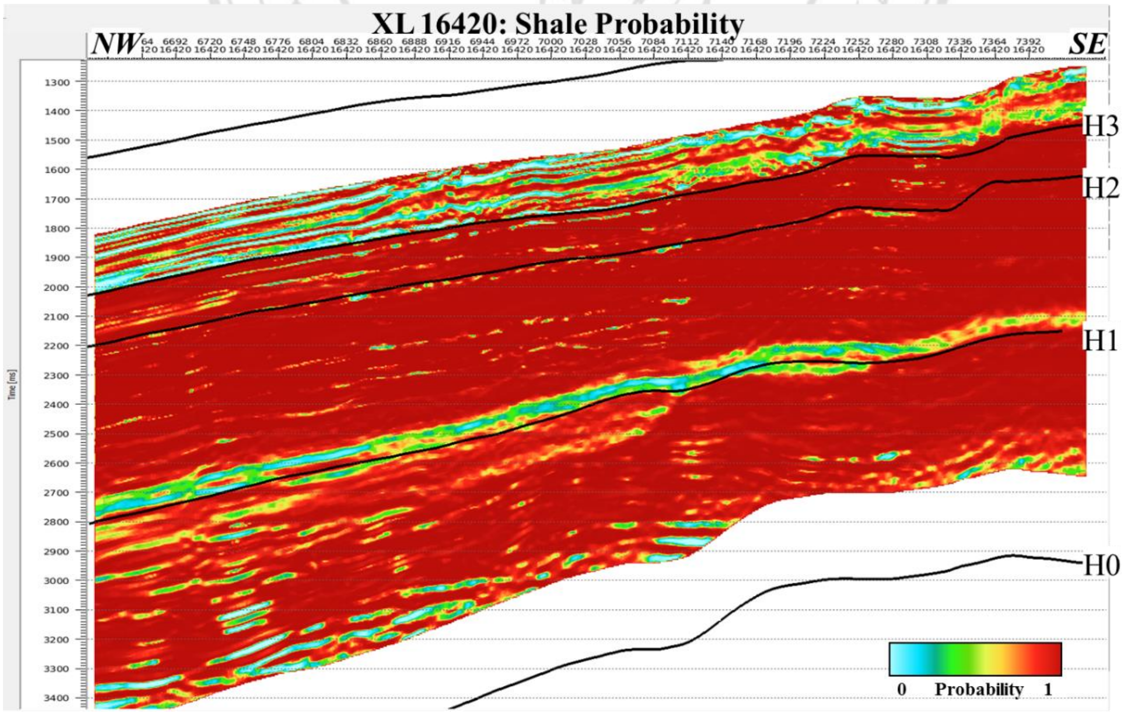

Figure D-59 Crossline 16420 section showing the distribution of shale probability.

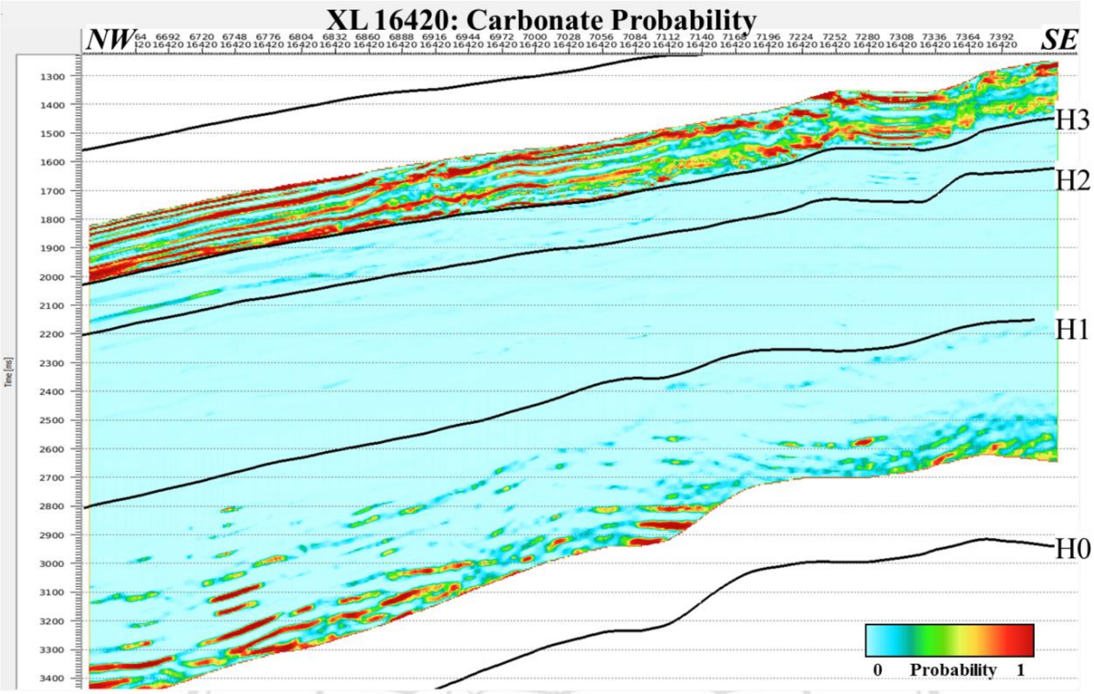

Figure D-60 Crossline 16420 section showing the distribution of carbonate probability.

CURRICULUM VITAE

Author's Name Ms. Namfon Pooksook

Date of Birth 18 April 1988

Education 2010 Bachelors of Science, Physics, Chiang Mai University

Scholarship 2007 - 2010 Faculty of Science, Chiang Mai University

2014 - 2016 PTT Exploration and Production Co., Ltd

Publication Pooksook, N., Wongpornchai, P., Sognnes, H.I. and Kongjuk, K., "Reservoir Characterization Using Pre-stack Simultaneous Inversion of 3D Seismic Data from Timor Sea, Australia." PROCEEDINGS: International Graduate Research Conference 2015, December 11.

Experiences 2010 - 2011 Associated geoscientist, PTT Exploration and Production Company Limited.

2011- Recent Geophysicist, PTT Exploration and Production Company Limited.